Dissertation

submitted to the

Combined Faculty of Natural Sciences and Mathematics

of Heidelberg University, Germany

for the degree of Doctor of Natural Sciences

Put forward by

Jiyoung Kim

born in: Busan, South Korea

Oral examination: 02.02.2022

Jet-hadron correlations to search for Mach cone signals in Pb–Pb collisions with ALICE at the LHC

referees:

Prof. Dr. Johanna Stachel

Dr. Alice Elisabeth Ohlson

Prof. Dr. Norbert Herrmann

Deutsche Zusammenfassung:

Bei relativistischen Schwerionenkollisionen wird erwartet, dass sich das Quark-Gluon-Plasma (QGP) bei extrem hohen Temperaturen und/oder hohen Baryonendichten bildet. Die mit hohem Impulsübertrag gestreuten Partonen (Quarks und Gluonen) erzeugen Teilchenschauer, die so genannton jets, welche sich in ähnliche Richtungen bewegen. Da diese Partonen beim Durchqueren des Mediums stark mit diesem wechselwirken, sind sie sehr gut geeignet um die Eigenschaften des QGP zu untersuchen. Der Energieverlust von Jets durch die Wechselwirkung mit dem QGP wurde bereits experimentell beobachtet. Als eine der möglichen Wechselwirkungen zwischen Jets und dem QGP wurden durch Jets induzierte Mach-Stoßwellen vorhergesagt. In dieser Arbeit wurden Winkelkorrelationen ($\Delta\varphi$, $\Delta\eta$) zwischen den Jet Achsen und Teilchen (alle Hadronen und identifizierte Protonen) analysiert um nach Signalen der Machstoßwellen zu suchen. Es wurden Pb–Pb-Kollisionen mit einer Schwerpunktsenergie pro Nukleon-Nukleon Paar von $\sqrt{s_{\mathrm{NN}}} = 5.02$ TeV analysiert, wobei der p_{T}-Bereich von $2 < p_{\mathrm{T}} < 4$ GeV/c für assoziierte Teilchen verwendet wurde. Mit der Analyse der Jet-Hadron- und Jet-Proton-Korrelationen konnten keine Mach-Stoßwellen im QGP beabachtet werden.

Zusätzlich wurden Hadron-Hadron-Korrelationen entlang der Pseudorapidität ($\Delta\eta$) mit ausgewählten Spuren basierend auf den geometrischen Informationen der Jet-Hadron-Korrelationen in Monte-Carlo-Simulationen und in gemessenen Daten untersucht. Die von den Mach-Stoßwellen erzeugten erwarteten Signale wurden über die Hadron-Hadron-Korrelationsmethode in der Simulation, jedoch nicht in den gemessenen Daten beobachtet. Aufgrund der großen statistischen Schwankungen konnte keine Schlussfolgerung gezogen werden. Dieses Ergebnis kann darauf zurückzuführen sein, dass das echte Signal kleiner ist als in der Simulation bzw, dass das Signal während der QGP Entwichlung abgeschwächt wurde. Deshalb wird es interessant sein, für diese Analyse Daten mit höherer Statistik zu benutzen, welche im Jahr 2022 mit ALICE aufgenommen werden. Außerdem kann in Zukunft die Abhängigkeit von der Ereignisebene berücksichtigt und das Ergebnis in Abhängigkeit vom Transversalimpuls analysiert werden.

Abstract:

In relativistic heavy-ion collisions, it is expected that the quark-gluon plasma (QGP) forms at an extremely high temperature and/or high baryon density. Hard-scattered partons (quarks and gluons), resulting in sprays of particles called jets, are crucial probes to investigate the characteristics of the QGP as they strongly interact with the QGP while traversing through the medium. The energy loss of jets due to the interactions with the QGP has been experimentally observed, and the theoretical prediction of Mach shock waves induced by jets as one of the possible interactions between jets and the QGP was suggested. In this work, an analysis of the angular correlations of particles (inclusive primary hadrons and identified protons) with respect to the axes of reconstructed jets is performed, to search for possible signs of a Mach shock wave induced by jet-medium interactions. This analysis was performed with the data measured in central Pb–Pb collisions at $\sqrt{s_{\mathrm{NN}}} = 5.02$ TeV in ALICE, using the p_{T} range for associated particles, $2 < p_{\mathrm{T}} < 4$ GeV/c and for background-subtracted jets above 25 GeV/c. The analysis of the jet-hadron and jet-proton correlations did not show signs of the Mach shock waves in the QGP. Additionally, hadron-hadron correlations in pseudorapidity ($\Delta\eta$) with the tracks belong to $\pi - \pi/4 < \Delta\phi < \pi + \pi/4$ in the jet-hadron correlations were studied in a toy Monte-Carlo simulation and in the data. The expected signals created by the Mach shock waves were observed well via the hadron-hadron correlation method in the simulation, however, the signals were not observed in the experimental data and we cannot draw a conclusion from the result due to large statistical fluctuations. This observation can imply that the actual signal might be smaller than the signal in the simulation or washed out during the QGP medium evolution. Therefore, more statistics are require for more precise measurements. Though the current statistics in the results are too limited to make a conclusive statement, it will be interesting to examine these correlation functions considering the event-plane dependence and p_{T}-differential results with the increased statistics, planned in future ALICE measurements in 2022.

Contents

0.1 List of Figures

0.2 List of Tables

1 Introduction

Physics is a science to understand and describe the rules of a system. Physicists pursue ultimate answers about the system, by finding the rules governing the system and discovering matter that has not been discovered yet. From ancient to modern physics, one of the fundamental questions is what are the elementary building blocks of matter.

After the discovery of atom, once people believed that atoms are one of the most fundamental particles that comprises the matter in the world. Such belief has been broken by one of the breakthrough achievements, the discovery of the atomic nucleus by Ernest Rutherford [1]. The work discovered that the majority of atomic mass is concentrated in the center of an atom as an atomic nucleus and figured out that atomic nuclei contain protons as constituents [2]. Later, James Chadwick discovered the neutron, another constituent of the nucleus in 1932 [3].

Most nuclei consist of densely packed protons and neutrons. Although neutrons do not interact with each other via electromagnetism, protons have the repulsive electromagnetic force between them. Based on the traditional theories such as only electromagnetism, the force that makes the nuclei stable in spite of the high density of protons in nuclei could not be explained.

Hideki Yukawa was the one who first suggested that protons and neutrons are bound together by a new field analogous to the electromagnetic field [4]. The suggestion included a prediction of a responsible particle in the interaction between protons and neutrons, 200 times heavier than the electron, which was observed in cosmic ray experiment by Powell and named the π-meson [5].

Not only the π-meson, many different particles, baryons and mesons, have been also observed by many experiments, and related theories have been quickly developed to explain such observations. One of them is the eight-fold way, an organizational scheme to explain baryons and mesons based on their intrinsic properties, suggested by Murray Gell-Mann [6]. Furthermore, the quark model, explaining that baryons and mesons consist of different configurations of fundamental particles (called quarks), triplets and douplets, respectively, was proposed by Gell-Mann and Zweig [7, 8].

The experimental evidence observed by a series of deep inelastic electron-proton scattering experiments at the Standford Linear Accelerator Center (SLAC) from 1968 confirmed the existence of such point-like particles, or 'partons' as constituents of the protons and the neutrons [9, 10, 11]. Later the 'partons' were renamed to ’quarks’, and it has been known that there are different types of quarks.

Among them, the light quarks, including up, down, and strange quarks were validated relatively early via the scattering measurements at SLAC, and more massive quarks (charm, bottom, and top) were observed later. The existence of the charm quark was confirmed experimentally in 1974 by two research groups independently at the same time; one was the team led by Richter at SLAC [12], and the other one led by Ting at Brookhaven National Laboratory (BNL) [13]. The bottom quark was observed by the group led by Lederman at Fermi National Accelerator Laboratory (Fermilab) in 1977 [14]. The top quark was finally observed by the CDF (Collider Detector at Fermilab) collaboration [15] and the DZero collaboration at Fermilab in 1995 [16].

Figure 1.1 shows that all these quarks are listed as elementary particles in the Standard Model, a theory describing three fundamental forces (electromagnetic, weak, and strong) and classifying elementary particles. Quarks and leptons, as the basic building blocks of matter, are called fermions based on their spin. Fermions have half-integer spin, like 1/2, 3/2, and so on. They have ’antiparticles’, that have the same mass, spin, and mean lifetime but have an opposite sign of electric charge and other charges. They and their antiparticles obey the Pauli exclusion principle and Fermi-Dirac statistics [18]. The difference between quarks and leptons is the interaction they are involved in. Quarks interact via the strong interaction, whereas leptons via the electroweak interaction. In addition to fermions, there is another type of particle, called bosons. Gauge bosons, as force carriers, mediate the interactions: gluons for the strong interaction, photons for electromagnetic interaction, and W and Z bosons for the weak interaction. The bosons have integer spin and follow Bose-Einstein statistics [18]. The term *gauge* refers to a type of field theory where the Lagrangian is invariant under local transformations. As the Standard Model is a gauge-invariant quantum field theory, the gauge bosons represent the quantized gauge fields [19, 20, 21, 22]. Vector and scalar bosons have different spins, 1 and 0, respectively. The Higgs boson plays a unique role, involving the mass generation of elementary particles via electroweak symmetry breaking [23, 24, 25].

Although the Standard Model has been regarded as a successful theory by providing precise experimental predictions, there are still several unexplained phenomena. For instance, gravity, one of the four known fundamental forces, is not included. Also the baryon asymmetry in our universe is not explained in the Standard Model [26]. Physicists are working hard to get more complete answers with various attempts, like Beyond Standard Model, Grand Unified Theory, and so on [27, 28].

In the following sections, we focus on the strong interaction between quarks and gluons to obtain a better understanding of the elementary building blocks.

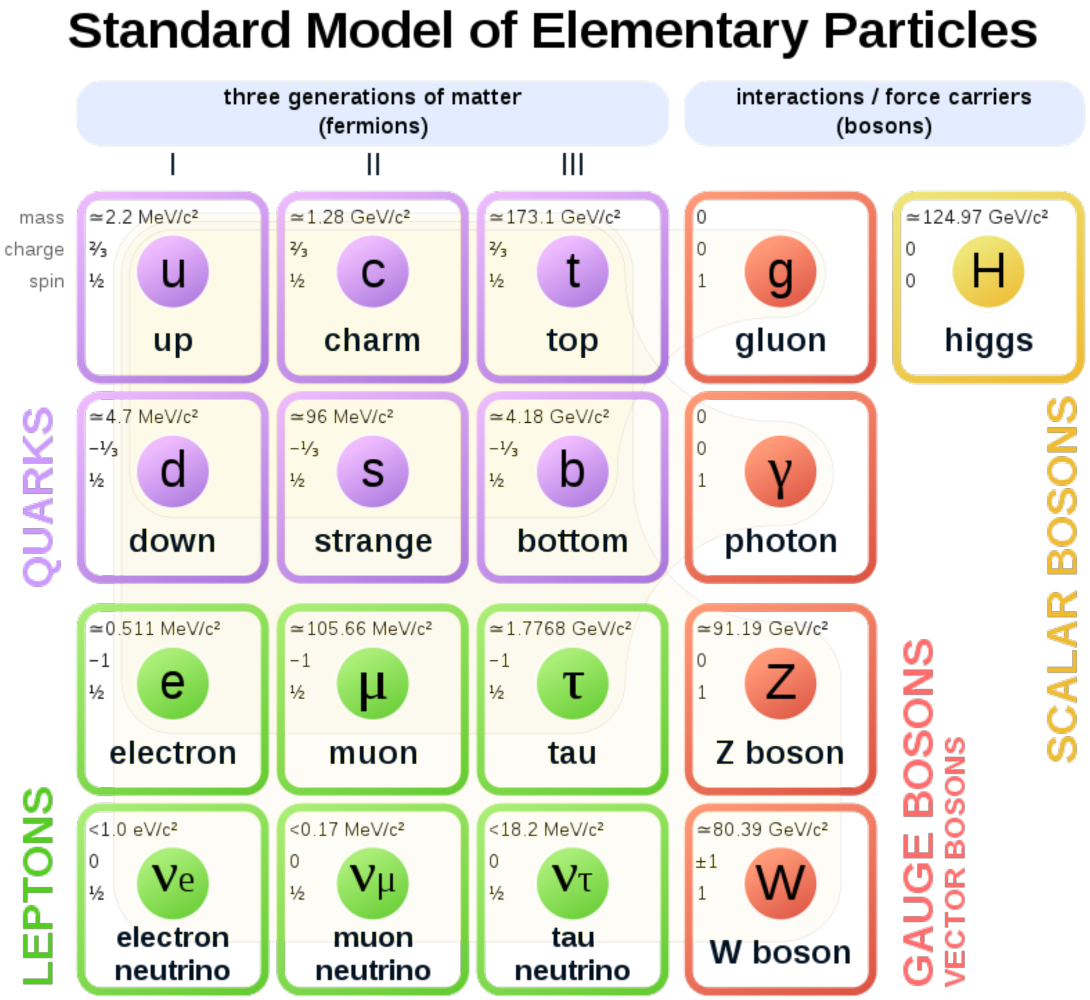

Figure 1.1: Standard Model of elementary particles
(figure taken from [17]).

1.1 Quantum Chromodynamics

When the eightfold way [6] and the quark model [7, 8] were introduced, they did not initially consider one of the degrees of freedom of the strong interaction, which is called 'color charge'. The concept of color charge was suggested to explain the existence of exotic particles, $\Delta^{++}(uuu)$, $\Delta^{-}(ddd)$, and $\Omega^{-}(sss)$.

Those particles were observed experimentally [29, 30, 31, 32], but they do not obey Pauli's exclusion principle. Later, Fritzsch and Gell-Mann introduced three color charges as a new degree of freedom in the strong interaction in 1971 [33, 34]. It was a starting point for Quantum ChromoDynamics (QCD), the theory of the strong interaction.

In QCD, quarks have three color charges: red, blue, and green. Those colors are not optical properties but quantum numbers to explain the natural symmetry of the system. There are also anticolors: anti-red, anti-blue, and anti-green. Gluons mediate the strong interaction between quarks, exchanging their colors, like red to anti-blue. In the case of Quantum ElectroDynamics (QED), photons play a role as a force carrier in electromagnetism, and they do not have any charges. Surprisingly, gluons, the force carrier in the strong interaction, have color charges themselves. This enables self-interactions by gluons, adding a high level of complexity in QCD [35].

Quarks are never observed independently in nature. Instead, they have to be confined into hadrons as a color-neutral state. Baryons are the combination of red-blue-green, and mesons are pairs of colors and anticolors, like red and anti-red. Inside of hadrons, quarks are bound with gluons, which change the color of the quarks. While changing the color charges, the total color charge should be conserved as neutral. Color confinement is one of the unique features of QCD, which makes hadrons exist in the form of baryons or mesons, or exotic hadrons including tetraquarks, pentaquarks, etc.

The binding energy between quarks by gluons can be scaled with a coupling constant, α_{s}, which is analogous to the electromagnetic coupling constant. Another feature of QCD is having a running coupling constant, depending on the interaction energy between quarks/gluons. The strong coupling constant is given by:

$$\alpha_{\mathrm{s}}(Q^2) = \frac{\alpha_{\mathrm{s}}(\mu^2)}{1 + (\alpha_{\mathrm{s}}(\mu^2)/12\pi)(33 - 2n_f)\ln(Q^2/\mu^2)} \tag{1.1}$$

with the momentum transfer Q, the energy scale μ, and N_f, the number of quark flavors [35]. Figure 1.2 shows the running coupling constant (α_{s}) as a function of the momentum transfer (Q). The QCD prediction, shown as the solid black lines, is in a good agreement with the extracted values from the experiments. The strong coupling constant decreases significantly with increasing Q^2. A small coupling constant at large momentum transfer, equivalent to a short distance, refers to quarks/gluons behaving as free particles in the regime, called asymptotic freedom. In contrast, a large coupling constant at small momentum transfer, equivalent to a long distance, refers that quarks and gluons cannot exist individually, which is color confinement. Furthermore, it is possible to do perturbative calculations thanks to the small coupling constants at large Q^2 [36, 37].

$\lambda_{\mathrm{Q}CD}$ refers to the location of the QCD Landau pole, used as an indicator between perturbative and non-perturbative regimes in QCD [35]. It is defined as:

$$\lambda_{\mathrm{Q}CD} \equiv \mu^2 \exp\left[-\frac{12\pi}{(33-12n_f)\alpha_{\mathrm{s}}(\mu^2)}\right] \tag{1.2}$$

With the $\lambda_{\mathrm{Q}CD}$ scale, the coupling constant is described by:

$$\alpha_{\mathrm{s}}(Q^2) = \frac{12\pi}{(33-2n_f)\ln(Q^2/\lambda^2_{\mathrm{Q}CD})} \tag{1.3}$$

When $Q \gg \lambda_{\mathrm{Q}CD}$, perturbative calculations are possible, and when $Q \approx \lambda_{\mathrm{Q}CD}$, non-perturbative treatments are needed in QCD.

As described above, QCD has unique and interesting features distinctly different from QED: color confinement and asymptotic freedom. QCD has an evident constraint since quarks and gluons are bound into hadrons under normal conditions. However, the running coupling constant enables to access quarks and gluons in the asymptotic freedom at the larger momentum transfer (Q). This feature is related to hard scattering process discussed in Ch. 2 and allows to think of a new state of matter, where quarks and gluons are asymptotically free. A state of matter called Quark-Gluon Plasma (QGP) is needed to directly explore the realm of deconfined quarks and gluons.

1.2 Quark-Gluon Plasma (QGP)

It has been discussed that QCD matter could undergo a phase transtion, and its possibility has gained a general agreement in the physics community. For example, Collins and Perry argued that the quark model implies the existence of superdense matter consisting of quarks, and suggested that it could be found in neutron-star cores and the early universe after the Big Bang [39]. Cabibbo and Parisi also proposed that exponentially growing hadronic state densities can be interpreted as the presence of a phase transition [40]. Both papers suggested that a phase transition to a phase consisting of deconfined quarks and gluons occurs at a high temperature or high baryonic density.

Figure 1.3 shows a phase diagram of QCD matter as a function of the system's temperature and baryon chemical potential, equivalent to the baryon density. In

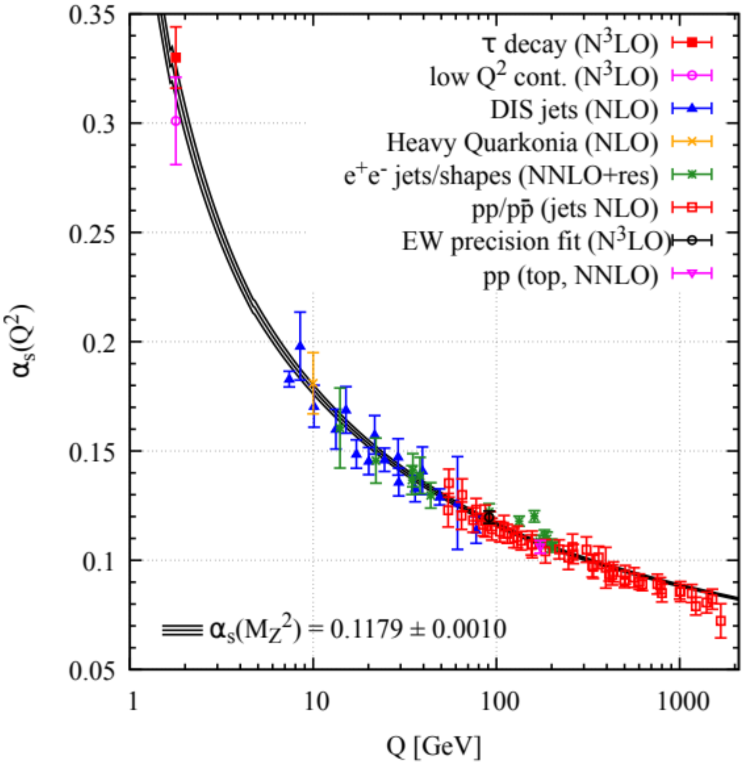

Figure 1.2: Strong coupling constant (α_s) as the function of the momentum transfer (Q) in deep inelastic scattering processes. The solid black line represents the theoretical QCD prediction. Colored points are extracted values from different experiments at different energy scale, Q. The information inside parentheses indicates used approximation orders of pQCD calculation. The world average of α_s at the mass of the Z boson is given as a reference. (figure taken from [38]).

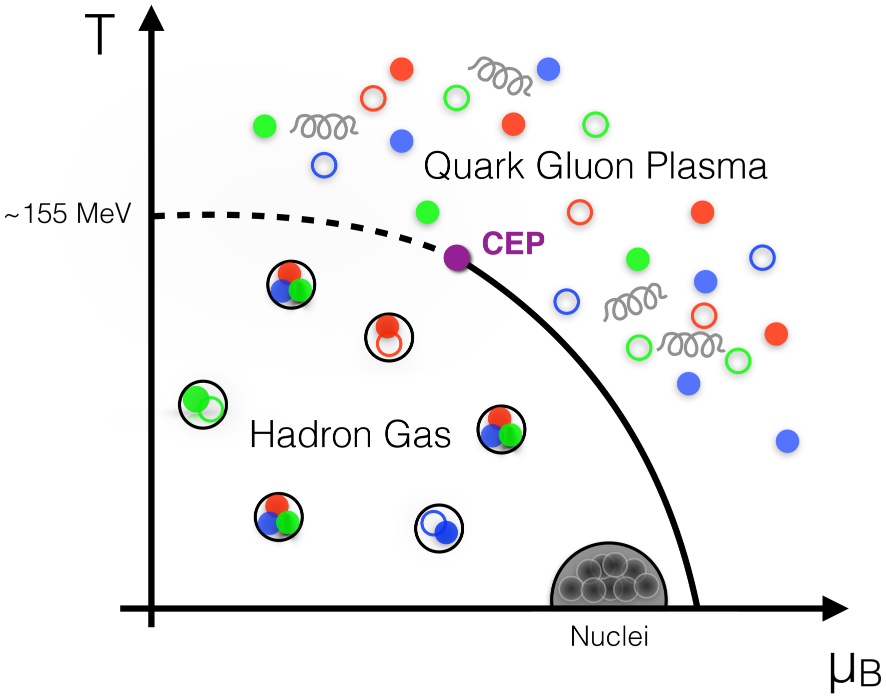

Figure 1.3: Sketch of the QCD phase diagram as a function of T (the temperature of the system) and μ_B (baryon chemical potential of the system), correlated to the baryon density. The gray region on the right bottom indicates that hadrons (protons, neutrons) are bound into nuclei. When the temperature goes up, hadrons are not bound and move freely in the hadron gas state. Two types of transitions are shown: a first-order phase transition (solid line) and a cross-over transition (dashed line). The first-order transition means a more discrete transition from hadron gas to the QGP. The purple point is a critical endpoint (CEP). (figure taken from [41]).

an ordinary regime, hadronic matter exists as nuclei. However, when the system becomes heated, it turns to a hadron gas state. When it is above the critical temperature (described in Fig. 1.3, around 155 MeV), the system reaches the QGP state in which the components of the hadron (quarks and gluons) are deconfined [42, 43].

pQCD calculations do not work in this phase transition regime due to the large coupling constant. Instead, lattice QCD (LQCD), discretized QCD calculations, have been used to calculate the critical temperature in the phase diagram [41, 44]. LQCD is a computational method to solve the QCD Lagrangian on a space-time lattice while approaching the lattice spacing a to zero (the continuum limit) [45, 46].

The critical temperature was estimated [42, 43] as

$$T_{\mathrm{c}} = 154 \pm 9 \text{ MeV} \tag{1.4}$$

Investigation of the QGP allows us to understand the strong interaction and enable access to deconfined quarks and gluons. In addition, our universe underwent the QCD phase transition a few microseconds after the Big Bang [39]. Therefore, research on the QGP state and its phase transition contribute to establishing an understanding of fundamental particles, quarks and gluons, and the evolution of our universe.

1.3 Relativistic heavy-ion collisions

As mentioned in the earlier section, high temperatures and/or densities are required to make a phase transition to the QGP. Relativistic (or ultrarelativistic) heavy-ion collisions enable us to achieve such conditions experimentally.

When heavy ions (commonly gold or lead) are accelerated to relativistic speeds, close to the speed of light (c), and collide with each other, a significant fraction of their kinetic energy is deposited in the collision. Thus, the system of colliding nuclei achieves an exceptionally high energy density (equivalent to extremely high temperatures) environment, enabling it to reach the QGP state.

Figure 1.4 displays a simulation of a heavy-ion collision in order of time. Two Lorentz-contracted nuclei are incoming from opposite directions, then colliding with each other. After that, a particular medium, assumed as the QGP, is produced. The medium expands in all directions (4π) over time. As the temperature of the medium cools down, propagating particles (quarks and gluons) are confined into hadrons, which are illustrated as white particles in the simulation.

In Fig. 1.5, a schematic of the space-time evolution of a heavy-ion collision is illustrated according to the beam direction (z) and time (t). After the collision,

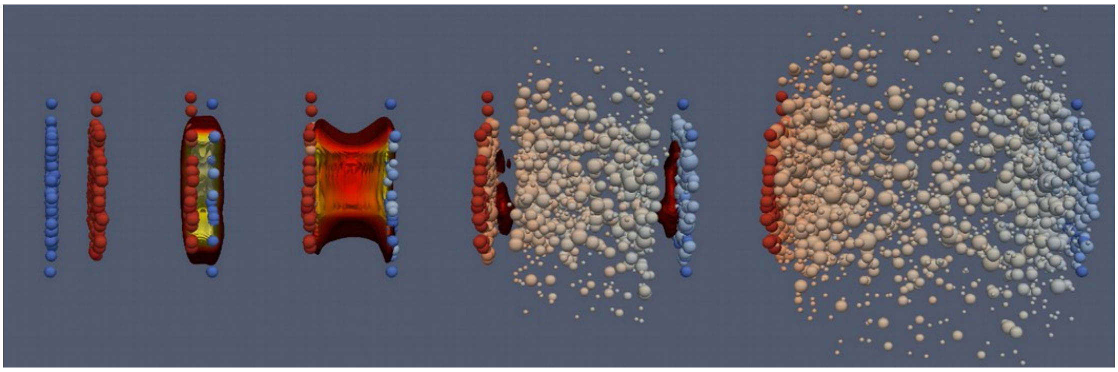

Figure 1.4: Visualized medium evolution during a heavy-ion collision. Lorentz contracted nuclei collide with each other. The second and third stages show the QGP formation and its expansion. As the temperature cools down, propagating particles from the QGP are bound into color-neutral hadrons shown as white particles. (figure taken from [47]).

the diagram indicates a short time interval before the QGP is created. At this stage, the system is heated by the collision energy and finally reaches the critical temperature (T_c) to produce the QGP state [48, 49]. In the meantime, initial interactions between quarks/gluons with high momentum transfer (called hard scatterings) can happen, for more detailed explanations see Sec. 2.1.

The QGP formation starts from τ_0 presumed lower than 1 fm/c, and it lasts for about 10 fm/c. Afterwards, it reaches the cross-over phase transition from the QGP state to the hadron gas at $T = T_\mathrm{c}$, the critical temperature. Then, the chemical freeze-out (T_ch) and kinetic freeze-out T_fo follow in order.

The chemical freeze-out indicates the lower temperature limit that enables the creation/change of quark compositions via inelastic scatterings in the QGP medium. After that, the proportional yields of produced particles are entirely determined. Such quark-level interaction is more unrestrained in the QGP state, so T_c and T_ch are very close [51, 52].

The kinetic freeze-out comes later than the chemical freeze-out. Although the composition of quarks in each particle is determined, they still interact with each other, affecting their kinetic properties like momentum via elastic scattering. After the kinetic freeze-out, the kinematics (momentum distribution) of particles are fixed. Subsequently, hadronic particles propagate toward the detectors in the experiments.

The first official announcement about the existence of QGP in relativistic heavy-ion collisions was made on 10 February 2000 at CERN [53]. Spokespersons from the heavy-ion program experiments at CERN presented compelling evidence of the existence of a new state of matter where quarks move freely instead of be-

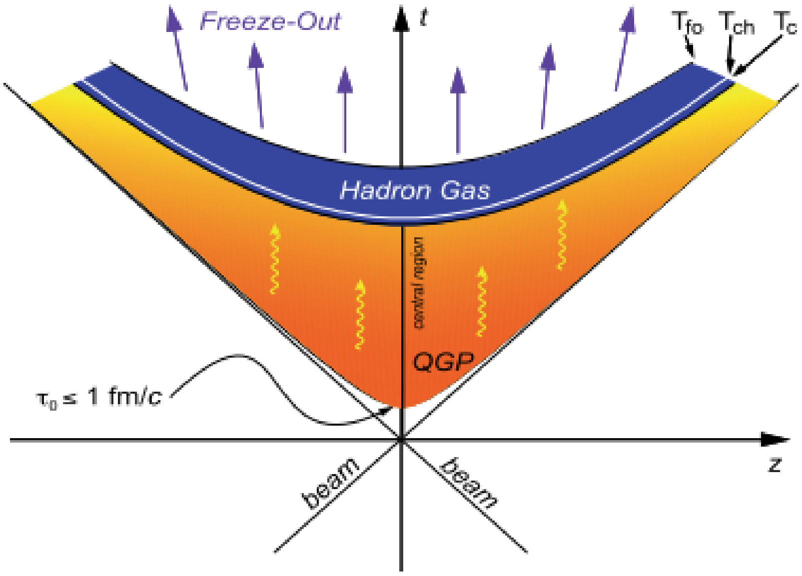

Figure 1.5: Schematics of the space-time evolution of a relativistic heavy-ion collision, indicating the beam direction, z, and time, t. τ_0 indicates the start of the QGP formation. T_{c}, T_{ch}, and T_{fo} are temperatures for the phase transition, chemical freeze-out, and kinetic freeze-out. (figure taken from [50]).

ing confined into more complex particles (baryons, mesons) such as protons and neutrons.

This statement came from the combined data from the seven heavy-ion experiments at the Proton Synchrotron (PS) and Super Proton Synchrotron (SPS) accelerators in CERN. (The experiments named NA44, NA45, NA49, NA50, NA52, WA97 / NA57, and WA98) They measured different aspects of lead-lead and lead-gold collisions. Although the combined results from all the experiments are consistent with the predicted signatures of QGP, the data from a single experiment was not enough to provide the complete picture.

Afterwards, a more apparent observation that confirms the existence of QGP was reported from the experiments (BRAHMS, PHENIX, PHOBOS, STAR) at the Relativistic Heavy Ion Collider (RHIC) at the Brookhaven National Laboratory (BNL) in the United States in April 2005 [54, 55, 56, 57]. Such discoveries influenced CERN's Large Hadron Collider (LHC) experimental program to include a dedicated heavy-ion experiment, ALICE, which has enabled measurements of heavy-ion collisions with higher collision energy by the LHC than the RHIC. Thanks to the higher collision energy, the produced medium in ALICE reaches higher temperatures and has a longer lifetime of the QGP in the collisions. Since the cross-section of produced particles in the QGP increases according to the collision energy, therefore, rare particles containing heavy quarks like charm and beauty are produced much more in the ALICE. ALICE has confirmed the observations made at RHIC, such as parton energy loss and collective expansion. In the following subsections, such QGP signatures are explained in more detail.

1.3.1 Parton energy loss

The energy loss of highly energetic partons (gluons and quarks) trasversing the QGP medium was first suggested as evidence of the QGP existence [58]. During the propagation of the energetic partons in the QGP medium, the constituents of the QGP medium (quarks and gluons) may collide with the propagating parton. Therefore, such collisions result in the energy loss of the trasversing parton in the QGP medium. However, the partons lose their energy not only via such collisional energy loss but also another process called radiative energy loss, discussed in Sec. 2.2 in more detail. Later, calculations revealed that radiative energy loss is more dominant than collisional energy loss [59].

Such energy loss was observed via the nuclear modification factor (R_{AA}) measurements at RHIC, for instance; R_{AA} as a function of p_{T} is given as:

$$R_{\mathrm{AA}}(p_{\mathrm{T}}) = \frac{1}{\langle N_{\mathrm{coll}} \rangle} \frac{\mathrm{d}N_{\mathrm{AA}}/\mathrm{d}p_{\mathrm{T}}}{\mathrm{d}N_{\mathrm{pp}}/\mathrm{d}p_{\mathrm{T}}} \tag{1.5}$$

where $\mathrm{d}N_{\mathrm{AA}}/\mathrm{d}p_{\mathrm{T}}$ is the p_{T}-differential yield of particles in nucleus-nucleus (A–A) collisions, $\mathrm{d}N_{\mathrm{pp}}/\mathrm{d}p_{\mathrm{T}}$ is the p_{T}-differential yield of the same particles in pp collision, and $\langle N_{\mathrm{coll}}\rangle$ is the average of the number of nucleon collisions. $\mathrm{d}N_{\mathrm{AA}}/\mathrm{d}p_{\mathrm{T}}$ normalized with $\langle N_{\mathrm{coll}}\rangle$ corresponds to the p_{T}-differential yield in pp collision. Considering that the QGP is not created in pp and A–A collisions and the A–A collisions are just a superposition of multiple nucleon collisions, this R_{AA} should be 1. However, under the assumption that the QGP is formed in A–A collisions, but not in pp collisions, it cannot be explained by only the superpostion of mutiple nucleon collisions, and a the deviation of the modification factor from 1 can be interpreted as the effect of QGP medium in Pb–Pb collisions on the particle production.

Figure 1.6 shows R_{AA} comparisons as a function of p_{T}, measured from the PHENIX (Pioneering High Energy Nuclear Interaction eXperiment) experiment at RHIC. Since direct photons are not colored objects, they do not undergo a strong interaction with the QGP. Thus their R_{AA} is close to 1. However, π^0 and η mesons have clear evidence of an interaction with the QGP, showing a significant suppression (lower than 1) at high p_{T}. Moreover, the suppression scale is in agreement with the pQCD model prediction of parton energy loss. The model prediction was calculated based on radiative energy loss of partons. π^0 and η at the high p_{T} region are produced via jets, the fragmentation of hard scattered partons. When partons traverse through the QGP, the partons lose their energy due to the interaction with the QGP medium. As a result, the significant suppression is observed at high p_{T} region. This parton energy loss is regarded as one of the QGP signatures, and it is connected to the phenomena called jet quenching. This aspect is discussed in Ch. 2.

1.3.2 Collective flow

Collective flow refers to a grouped motion of particles as a bulk, which is a phenomenon usually observed in heavy-ion collisions. It can be described in terms of relativistic hydrodynamics. A review of the relativistic hydrodynamics for heavy-ion collisions can be found in [61, 62]. In the hydrodynamical picture, a thermalized QGP medium has a high energy density in a small volume (the "fireball") compared to the vacuum. Such deviation of the density produces a pressure between the fireball and the vacuum, making the medium expand. This is called collective behavior or flow [63].

At the beginning of the heavy-ion research, the radial expansion was observed experimentally. It was described well by a blast-wave model in the experiments [64]. The blast-wave model assumes the condition that particles are created thermally from boosted sources with a radial velocity profile,

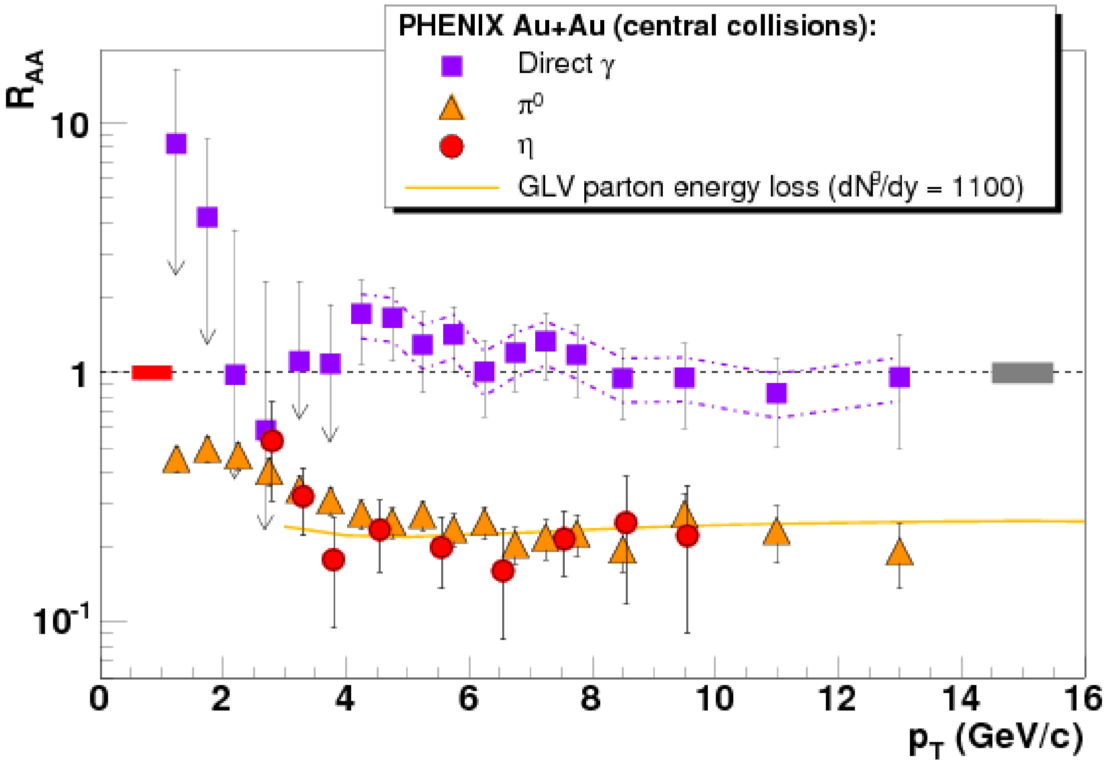

Figure 1.6: Nuclear modification factor (R_{AA}) measurement of π^0 (orange triangle), η (red circle) and direct γ (purple square) as a function of p_{T} in central Au–Au collisions at $\sqrt{s_{\mathrm{NN}}}$ = 200 GeV from the PHENIX experiment. Dash-dotted lines indicate uncertainties from NLO-pQCD calculation for the pp reference of direct γ. The solid yellow line is a parton energy loss prediction for pions in a medium with initial gluon density $d\mathrm{N}^{\mathrm{g}}/dy = 1000$. In the energy loss calculation, gluon radiation process is mainly considered. (figure taken from [60]).

$$\beta_r(r) = \beta_\mathrm{s}\left(\frac{r}{R}\right)^n \tag{1.6}$$

where β_s is the surface velocity and R is the radius of the fireball. The particle spectrum is given as the superposition of individual thermal sources.

$$\frac{\mathrm{d}n}{m_\mathrm{T}\mathrm{d}m_\mathrm{T}} \propto \int_0^R r\mathrm{d}r m_\mathrm{T} I_0\left(\frac{p_\mathrm{T}\sinh\rho}{T_\mathrm{kin}}\right) K_1\left(\frac{m_\mathrm{T}\cosh\rho}{T_\mathrm{kin}}\right) \tag{1.7}$$

with $\rho = \tanh^{-1}\beta_r$, the transverse mass $m_\mathrm{T} = \sqrt{m^2 + p_\mathrm{T}^2}$, the modified Bessel functions I_0 and K_1, and the kinetic freeze-out temperature, T_kin.

Figure 1.7 shows a combined blast-wave fit and measured spectra of light flavor hadrons. The fit shows good agreement with the data. In the higher p_T range, the fit has a substantial deviation from the data in general. It is because high p_T particles are not thermally produced in the fireball. Instead, they have a different origin, like hard scattering and fragmentation. The low p_T pions over the fit was previously explained due to the pion production from resonance decays, called the feed-down effect. Recently, there is a different aspect to explain those results, using a different freeze-out prescription [66].

So far, the radially symmetric flow has been discussed. However, azimuthally anisotropic flow, elliptic flow becomes important in semi-central/peripheral collisions. Elliptic flow is generated by the spatial anisotropy of a non-central collision, shown as in Fig. 1.8. Inside the almond-shaped fireball, different pressure gradients work anisotropically: stronger along the shorter axis due to the higher density and relatively weaker along the longer axis. These pressure gradients push particles stronger along the shorter axis, which leads to a momentum increase in that direction (x axis in Fig. 1.8). This impacts the momentum anisotropy of the outgoing particles, for example, the average momentum of particles is higher towards the shorter axis than towards the longer axis. In addition, the increased momentum of particles along the shorter axis makes the particles propagate farther in that direction, as a result, the particles are anisotropically distributed on the azimuthal plane due to the elliptic flow. Elliptic flow is expressed as the second coefficient v_2 in the Fourier expansion of the azimuthal distribution of particles [67],

$$E\frac{\mathrm{d}^3N}{\mathrm{d}^3p} = \frac{1}{2\pi}\frac{\mathrm{d}^2N}{p_\mathrm{T}\mathrm{d}p_\mathrm{T}\mathrm{d}y}\left(1 + 2\sum_{n=1}^{\infty} v_n \cos n(\varphi - \Psi_{\mathrm{PP},\ n})\right) \tag{1.8}$$

where φ is the azimuthal angle of the particles, v_n is the n-th order Fourier coefficient, and $\Psi_{\mathrm{PP},\ n}$ is the n-th order participant plane. The participant plane is defined by the collection of participants (nucleons involving in the collision, see Sec. 3.5.1), which can fluctuate in each event due to the fluctuation of the nucleon density. From this Eq. 1.8, the second coefficient v_2 can be obtained. The higher

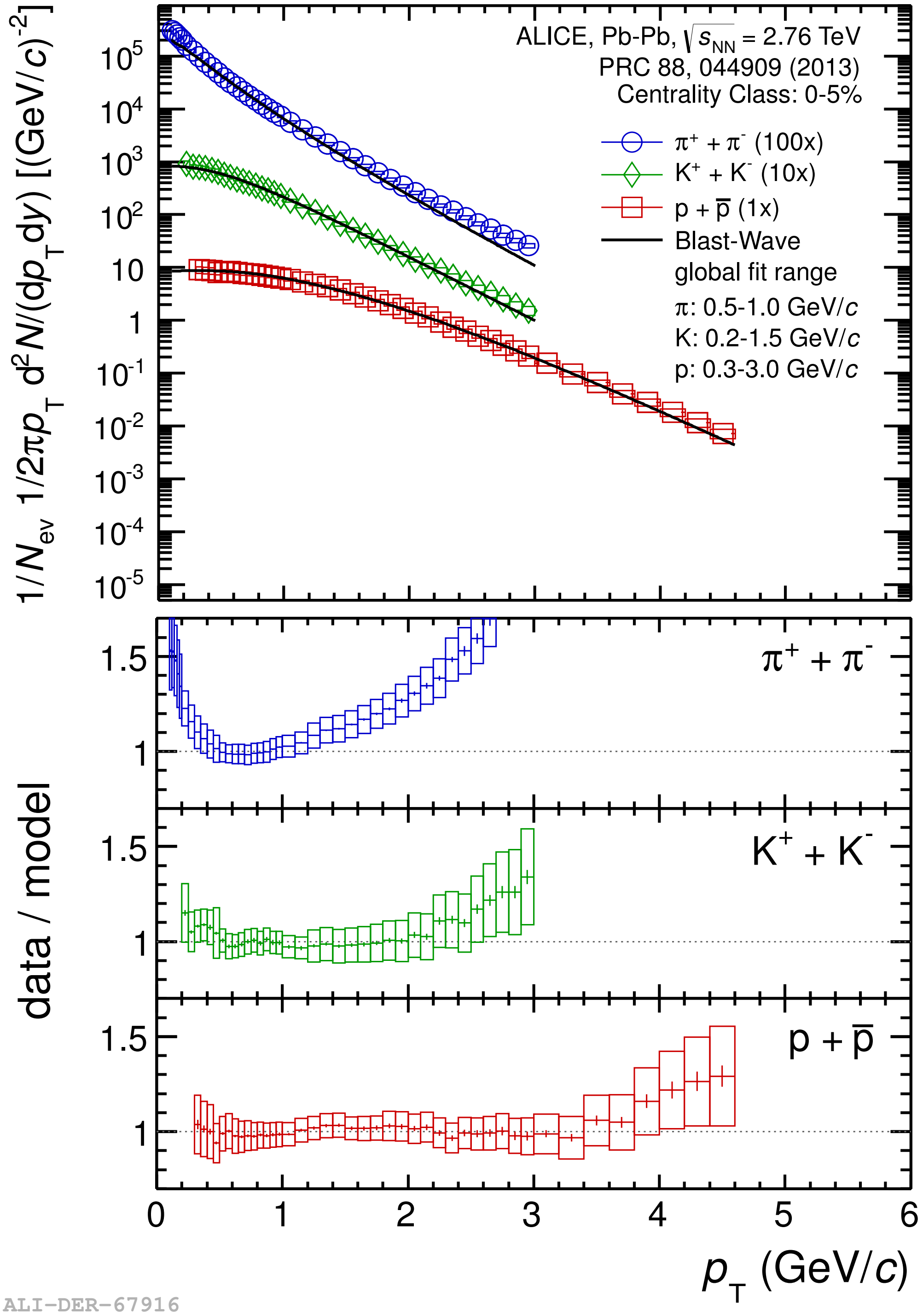

Figure 1.7: Blast wave fits to the measured spectra of particles. All particles are summed charge (±) states. Spectra are measured in most central events (0-5%) by ALICE. The fit range for the blast-wave is shown in the legend. (figure taken from [65]).

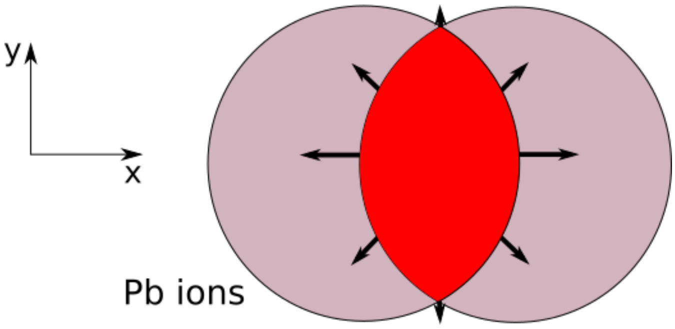

Figure 1.8: Schematic of the almond-shaped initial geometry in a heavy ion collision. The red area shows the overlap region between colliding lead ions. The black arrows indicate different sizes of force caused by the pressure gradients along the axes.

order of harmonics, v_3, v_4 and so on, which are having different shape of the participant planes (circular, quadratural and so on) induced by the density fluctuation, can also be obtained. Details on the experimental methods can be found in [68].

As explained, parton energy loss and collective flow are prominent phenomena in heavy-ion collisions. The collision is a complex system made of diverse physical phenomena and processes. They are not independently happening and affect each other, and display convoluted outputs in the end. Studies are done to disentangle the processes and to understand the whole picture. In the following chapter, the specific process of interest in this analysis is discussed.

1.4 Outline

This thesis discusses experimental analyses of possible interactions between the QGP and jets, like a Mach shock wave, through jet-hadron correlation and jet-proton correlation methods. Relevant characteristics of the QGP, experimental observables, and the explicit strategy of analyses are described in Ch. 2. Chapter 3 gives an overview of ALICE, its sub-detectors, and the analysis framework. General analysis criteria for events, tracks, and jet selections are introduced in Ch. 4. The jet-hadron correlation analysis and the jet-proton correlation analysis are presented in Ch. 5. A new method with hadron-hadron correlation with away side tracks is explained in Ch. 6. Finally, a summary, conclusion, and outlook are given in Ch. 7.

2 Jets and the correlation function

2.1 Jets in high energy collisions

As explained in Ch. 1, quarks and gluons (called partons) are confined in hadrons and not independently measurable. But under certain circumstances, they can be freed from hadrons due to the running coupling constant. Figure 1.2 shows the running coupling constant (α_{s}) of the strong force according to the momentum transfer (Q). The coupling constant decreases dramatically when the momentum transfer between partons becomes larger. Which means, when there is a large momentum transfer between partons, then the involved partons have an opportunity to escape to the outside of hadrons. This event is called *hard scattering* and happens in particle collision experiments [69].

While these almost freed partons travel, they actually cannot exist in a free form since they carry their color charge away. They should always be in a colorless state [69]. While they travels, more energy is required when the distance is longer between the two partons. At some point, the amount of energy needed to be stable at the colorless state of the two partons is higher than the energy to create a pair of partons between them. As a result, a pair of partons is produced in the middle of the original two partons to make a color-neutral state. As far as the original two partons moves away, more pairs can be produced, as shown in the Fig. 2.3. Therefore, each parton produces other colored particles around itself to form a color-neutral object to keep this colorless state. This process is called *fragmentation* [70].

The final output of the processes mentioned above is called a 'jet'. Figure 2.1 represents the physical schematic of jet production in a particle collision. Initially, partons inside colliding nuclei have initial momenta, described by parton distribution functions (PDF). Figure 2.2 shows the PDFs obtained from the HERA experiment [72], which illustrates the probability function depending on the fraction of the carried momentum by each parton in a proton. The two partons carrying a certain momentum do hard scattering with a negligible strong coupling constant. As an aftermath of hard scattering, two partons escape from confinement and propagate through the vacuum during the fragmentation. Since it must fulfill the rule of momentum conservation, a back-to-back structure appears in the transverse plane. In the end, one can measure one/two cone-shaped sprays of particles in the experiment, which are the jets.

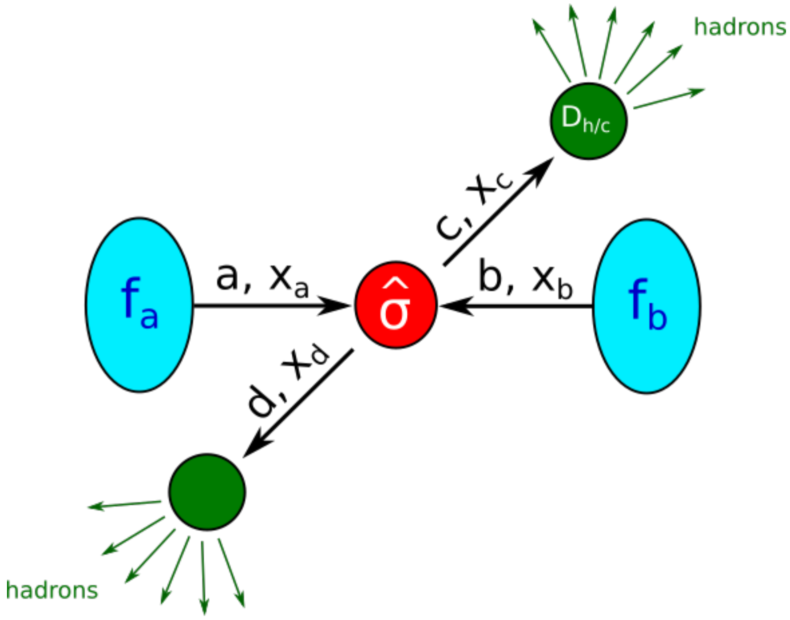

Figure 2.1: Schematic of jet production induced by hard scattering, calculated by the factorization of the involved processes (shown as Eq. 2.1). Initial partons are described by the parton distribution functions and the cross-section of hard scattering is calculated by pQCD. Fragmentation functions account for the hadronization process.

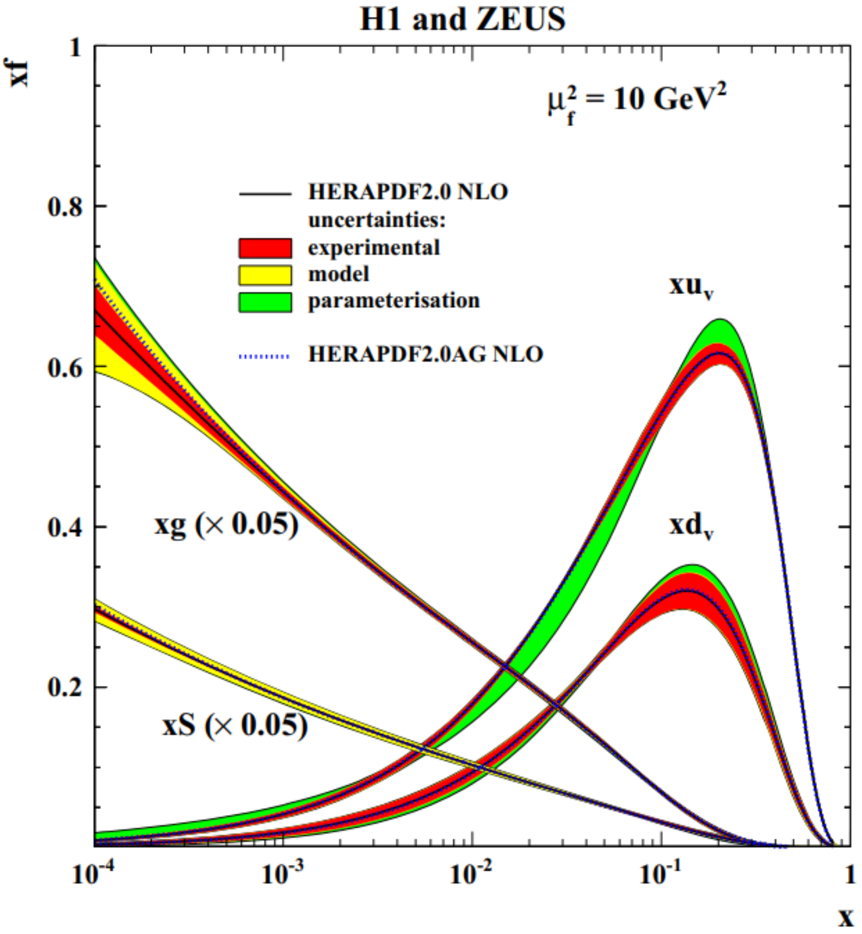

Figure 2.2: Parton distrubtion function (PDF) of a proton in the measurement and the model calculation. Experimental results measured in H1 and ZEUS detectors in HERA (Hadron Electron Ring Collider) accelerator at DESY (German Electron Synchrotron) in Hamburg. Deep Inelastic Scattering (DIS) between electrons/positrons and protons were studied in this facility to explore the proton's innermost structure and behavior. Parton density functions f(x) are extracted from QCD and from that, the probability to find a parton with a fraction, x, of the proton's momentum can be obtained. xf(x) is called the Parton Distribution Function (PDF). It is predicted to depend on the scale (μ_{f}^2), factorization scale, which corresponds to the average Q^2 (momentum transfer) taken in the inclusive DIS. In the figure, u and d are valence quarks composing the proton. And gluon and the virtual quarks (sea quarks, generated from gluon splitting) are dominant in the low momentum regime. Experimental results and the model calculation are in good agreement. This PDFs' results can be employed to study other collision experiments. (figure taken from [71]).

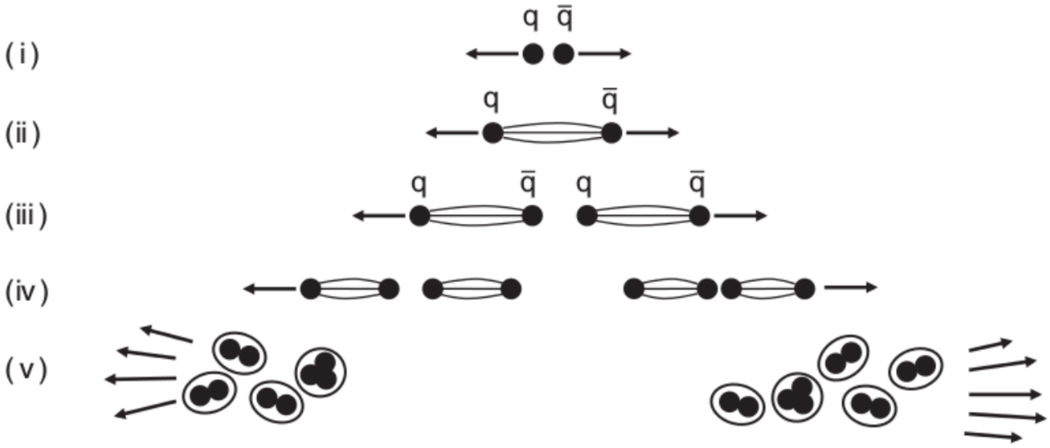

Figure 2.3: Theoretical picture of fragmentation from a high momentum quark-antiquark pair. (figure taken from [35]).

$$E\frac{d^3\sigma}{dp^3} \propto f_{a/A}(x_a, Q^2) \otimes f_{b/B}(x_b, Q^2) \otimes \frac{d\hat{\sigma}^{ab\to cd}}{dt} \otimes D_{h/c}(z_c, Q^2) \otimes D_{h/d}(z_d, Q^2) \tag{2.1}$$

where a and b refer to the initial partons in the nuclei A and B, c and d refer to the scattered partons after hard scattering, and h indicates hadrons created through the fragmenation process.

Jet production can be addressed by factorization of the processes [73, 74], like Eq. 2.1. The $f_{a/A}(x_a, Q^2)$ term indicates the PDF for the initial parton carrying a partial momentum of nuclei. These partons undergo hard scattering and turn into scattered partons ($\frac{d\hat{\sigma}^{ab\to cd}}{dt}$). The $D_{h/c,d}(z_{c,d}, Q^2)$ term shows fragmentation functions (FF) describing produced hadrons via the fragmentation of partons.

For hard scatterings with a small strong coupling constant, perturbative calculations in QCD (pQCD) can be used. On the other hand, PDF and FF are non-perturbative, but they both have universality [75], which means these do not change in some collision systems, for example, e-p collisions and pp collisions. Hence, calculations and results from theories and other nuclear experiments can be used [76, 77, 78].

Figure 2.4 compares a jet cross-section from the model prediction (with Next-to-Leading-Order pQCD) and experimental results from proton-proton collisions at $\sqrt{s_{\mathrm{NN}}} = 200$ GeV at RHIC [76, 79]. The theoretical calculation shows excellent agreement with the experimental data. As a well-established observable, jets have been used in particle and nuclear collision experiments for decades.

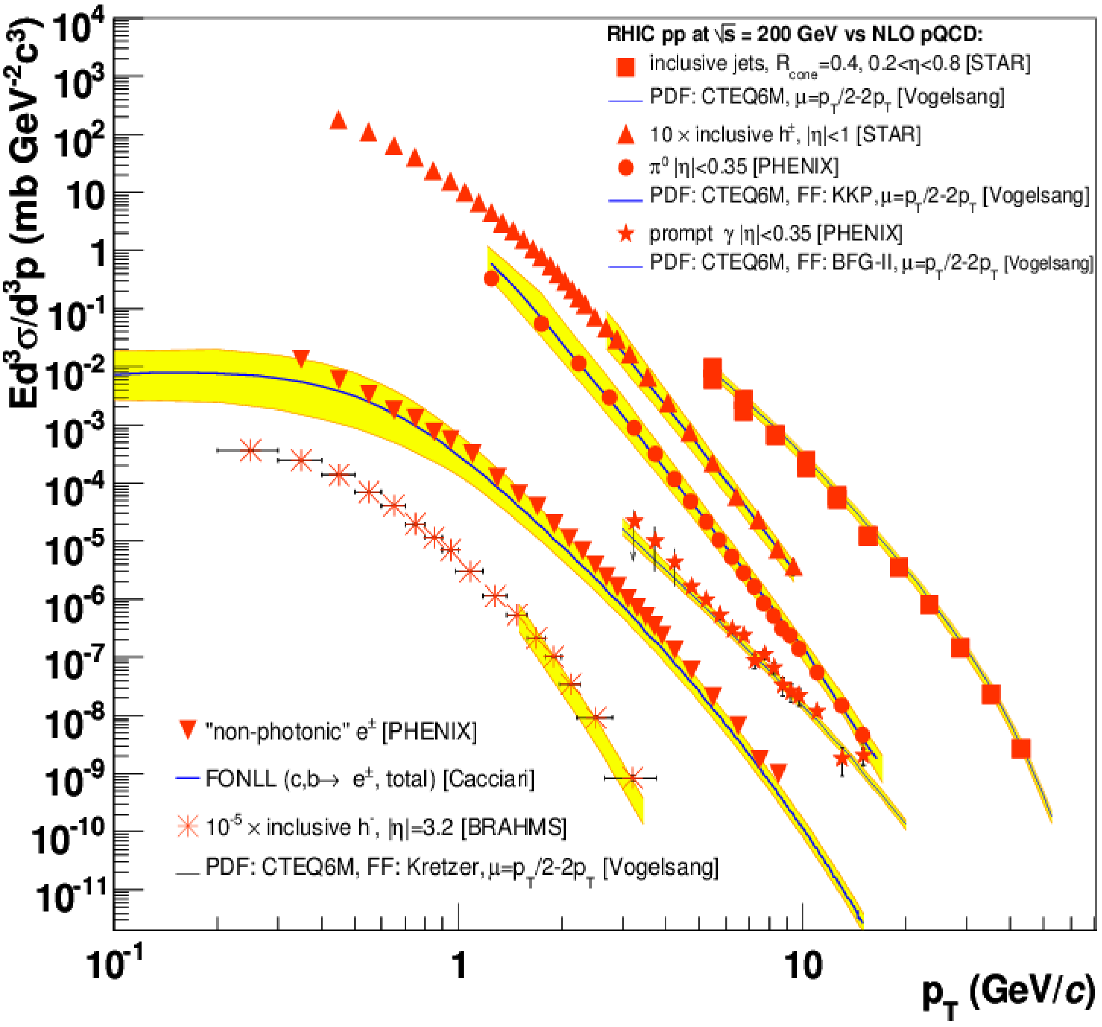

Figure 2.4: Compilation of cross-sections of inclusive jets and high momentum particles (inclusive hadrons, π^0, prompt γ and non-photonic electrons) in pp collisions at $\sqrt{s_{\rm NN}}$ = 200 GeV measured by STAR, PHENIX and BRAHMS, compared to NLO and NLL (Next-to-Leading-Log) pQCD preditions (black solid lines and yellow bands). (figure taken from [79]).

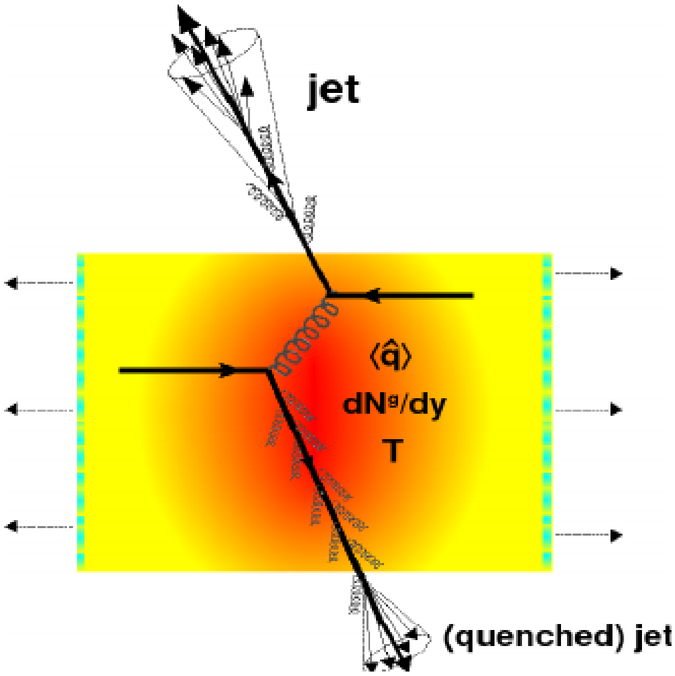

Figure 2.5: Sketch of jet quenching in a relativistic heavy-ion collision. The upper jet has much less energy loss and the bottom jet loses larger energy in the medium due to the long in-medium pathway. The energy loss is dependent on the medium properties, like gluon density ($d\mathrm{N}^{\mathrm{g}}/\mathrm{dy}$), temperature (T) and the average transport coefficient ($\hat{q}$). Only the radiational energy loss via gluon emission is depicted in this schematic. (figure taken from [79]).

2.2 Energy loss in the medium

2.2.1 Theoretical picture of jet energy loss

Jets have been used as a probe in QGP research, thanks to their robust theoretical and experimental understanding. Hard scattering occurs at a very early stage of the collision, assumed from 0.001 to 0.01 fm/c (considering $\tau_{hard} \sim \sqrt{Q^2}$ [80].) Since the QGP forms from 0.1 to 1 fm/c, which is later than the hard scattering process, hard scattered partons (jets) experience the entire evolution of the QGP medium [52]. While the parton travels in the QGP, it interacts and loses its energy entirely or partially in the medium, called jet quenching.

Figure 2.5 shows the schematics of jet quenching in the QGP medium. There are two back-to-back jets; the upper one located close to the surface of the QGP and the lower one which travels longer in the QGP. While propagating through

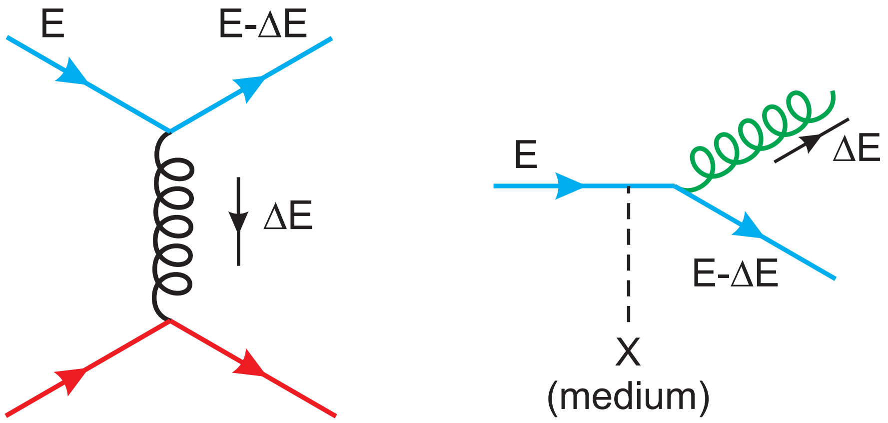

(a) Collisional energy loss

(b) Radiative energy loss

Figure 2.6: Diagrams for parton energy loss mechanisms in the QGP. (figure taken from [79]).

the QGP medium, the jet has significant interactions. In the end, it leaves with a much smaller jet energy compared to the original one. Figure 2.5 only describes the radiative energy loss. But, there are two mechanisms of jet energy loss; one is collisional energy loss, and the other is radiative energy loss. The former refers to the process of losing the energy via collisions with existing partons in the QGP, while the latter refers to the energy loss through gluon emission (gluon bremsstrahlung) during its travel in the QGP [81, 59]. In the low p_{T} regime, the collisional interactions are increasing, but the radiative interations are more dominant in the high p_{T} regime.

The radiative energy loss is related to the medium properties [82, 83], as shown in:

$$\Delta E \propto \alpha_{\mathrm{s}} C_{\mathrm{F}} \hat{q} L^2 \tag{2.2}$$

$$\hat{q} = \frac{\mu^2}{\lambda} \tag{2.3}$$

C_{F} refers to the color factor to determine the coupling strength of a gluon to a quark $C_{\mathrm{F}} = 3,\ 4/3\ $ for quark jets, gluon jets, μ^2 indicates the typical momentum transfer from the medium to the parton, λ refers to the mean free path in the QGP medium, and L refers to the travel length. $\hat{q}$ refers to the transport coefficient in the QGP. It has been theoretically predicted that gluon jets have a larger energy loss than quark jets via the radiative mechanism.

One more thing to point out in Fig. 2.5 is that even though jets lose their energy in the QGP medium via gluon radiation, the jets still exist as hard scattered

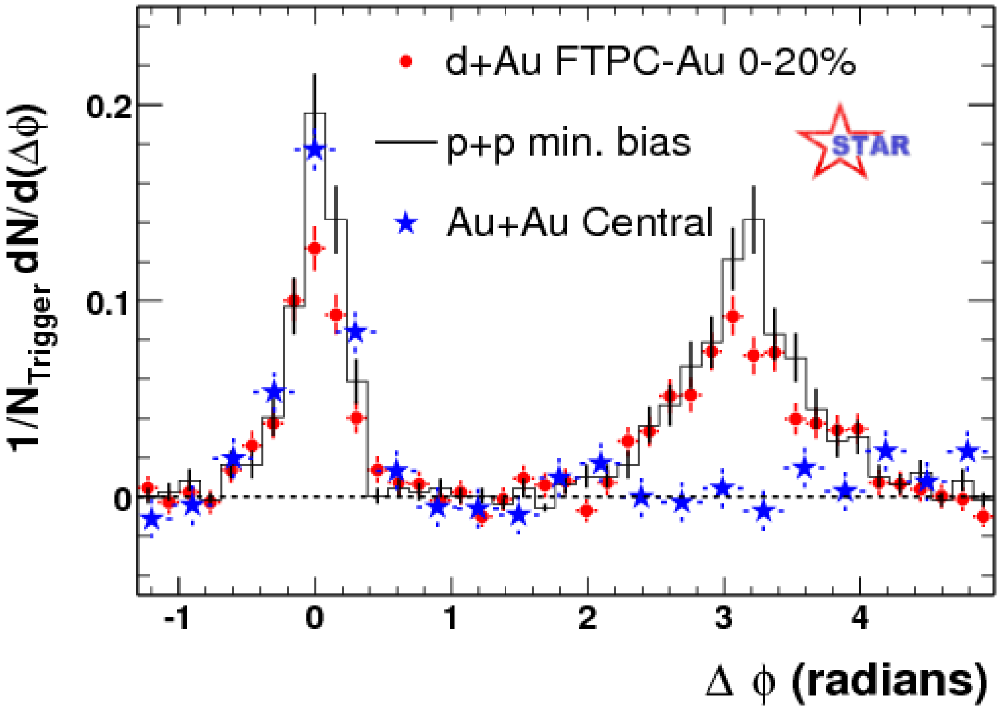

Figure 2.7: Two-particle azimuthal correlation distribution measured by the STAR collaboration for pp, d–Au, and central Au–Au collisions at $\sqrt{s_{\mathrm{NN}}} =$ 200 GeV. $\Delta\varphi$ is the opening angle between the trigger ($4 < p_{\mathrm{T}}^{\mathrm{trig}} <$ 6 GeV/c) and associated particles ($2 < p_{\mathrm{T}}^{\mathrm{assoc}} < p_{\mathrm{T}}^{\mathrm{trig}}$ GeV/c). 'FTPC-Au' indicates multiplicity measurement by using Forward Time Projection Chapter (FPTC) in the Au beam direction. (figure taken from [87]).

partons. According to the figure, the fragmentation of jets occurs after passing through the medium, which seems to agree with some measurements [84, 85, 86]. However, it is still an open question whether a jet can exist in the medium, or it is just a parton that then fragments into a jet when it exits the medium. Still, it was assumed that the interaction between jets and QGP follows the description in Fig. 2.5 in this thesis.

2.2.2 Experimental evidences of jet energy loss

As briefly discussed in Sec. 1.3, jet quenching has been measured with R_{AA} as a suppression of high p_{T} particles. The R_{AA} refers to a quantitative comparison between A–A and pp collisions based on the yield of particles in both collision systems, and the suppression of high p_{T} particles indicates the suppressed/reduced number of particles due to the jet quenching effect. Such jet quenching effect also can be observed in the angular correlation analyses, since jets have unique particle distributions by the fragmentation and the back-to-back structure at the azimuthal angle. The azimuthal correlation is calculated with the angle difference between a trigger particle and the associated particles:

$$\Delta\varphi = \varphi_{\mathrm{trig}} - \varphi_{\mathrm{assoc}} \tag{2.4}$$

Figure 2.7 shows azimuthal correlation distributions between particles measured in pp, d–Au and Au–Au collisions. Here, the measurement in d–Au collisions is used as a reference measurement, like pp without the QGP formation. It can have a nuclear effect (the cold nuclear matter effect) induced by a Au-ion, but is not well observed in this result. These correlation functions are normalized with the number of trigger particles in each collision system, and the results shows angular correlation distribution per the number of trigger particles, corresponding to the number of jets. These normalized correlation functions enable one to look into the averaged particle distribution around the trigger particle, compare different collision systems, and observe a precise modification of particles induced by the jet quenching. As shown in Fig. 2.7, a sharp peak appears around $\Delta\varphi = 0$, which is induced by the jet fragmentation. The opposite jet shows up around $\Delta\varphi = \pi$ by the back-to-back structure. Such two peaks are prominent in d–Au and pp but that is not the case in central Au–Au collisions. The opposite jet around $\Delta\varphi = \pi$ almost disappears in central Au–Au collisions, due to the jet quenching effect. Later, it was discovered that such jet quenching leads to an enhancement in low p_{T} particle production due to the deposit energy by jets to the QGP medium [88].

After the first observation of jet quenching, several novel measurements have been undertaken in many experiments [89, 90, 60, 91]. Among them, one significant discovery is the observation of a unique double bump structure in Au–Au collisions at STAR as shown in Fig. 2.8. This result also shows azimuthal correlation distributions between the particles measured in d–Au and Au–Au collisions. But, the p_{T} range for the associated particles is different from the previous result, as shown in Fig. 2.7. This result (Fig. 2.8) used lower p_{T} range, $1 < p_{\mathrm{T}}^{\mathrm{assoc}} < 2.5$ GeV/c to include the medium-produced particles by jet quenching, and was subtracted the background shape induced by v_2 on the azimuthal correlations. Initially, this was interpreted as a medium response produced by the interaction between jets and the QGP, which is described in the following section.

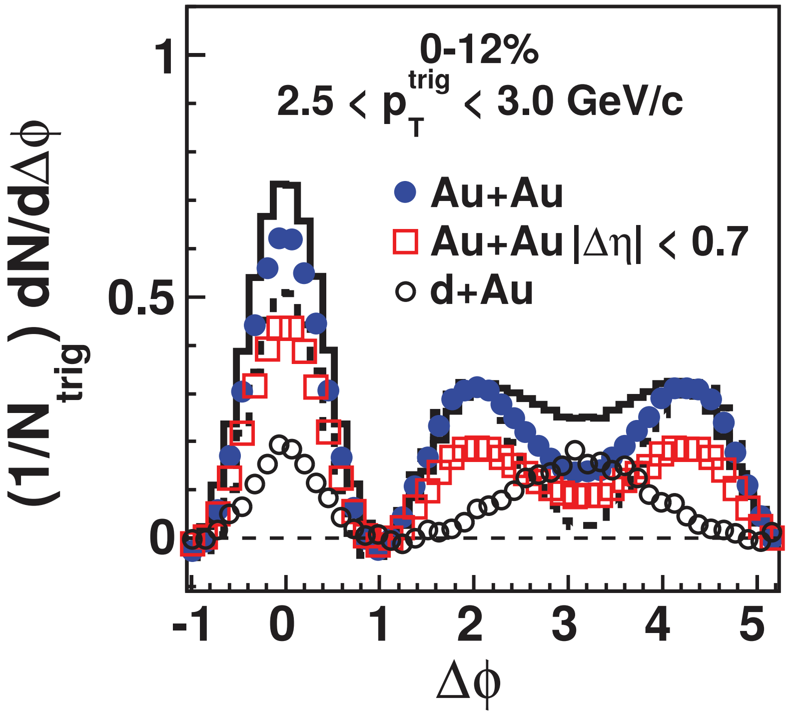

Figure 2.8: Background subtracted two-particle azimuthal correlation with Au–Au and d–Au collisions at $\sqrt{s_{NN}} = 200$ GeV from the STAR collaboration. $\Delta\varphi$ represents the opening angle between the trigger ($2.5 < p_T^{trig} < 3$ GeV/c) and associated particles ($1 < p_T^{assoc} < 2.5$ GeV/c) in central events (0-12% centrality). Solid blue and open black circles show full acceptance results ($|\Delta\eta| < 2.0$). Open red square shows restricted acceptance results ($|\Delta\eta| < 0.7$). The upper and lower limits of systematic uncertainty for the Au–Au results are shown as the solid and dashed histograms. This uncertainty is induced by the v_2 modulation of the subtracted background. (figure taken from [92]).

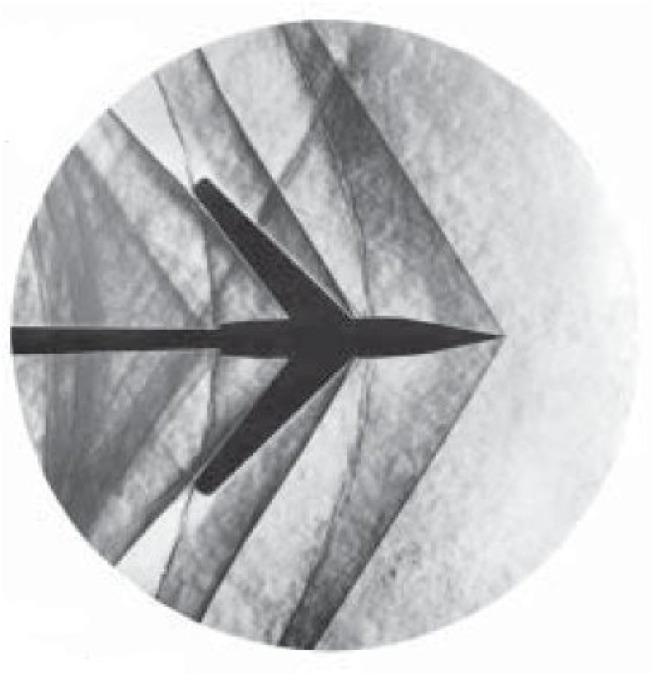

Figure 2.9: Picture of Mach shock wave induced by a sharp-nosed supersonic body. (figure taken from [96]).

2.3 Mach shock wave in the QGP

2.3.1 The Mach shock wave

The Mach shock wave refers to a general physical phenomenon that is created by a fast-moving object in a medium [93, 94, 95]. The term 'sonic boom' is often used to describe an explosive sound, associated with a Mach shock wave triggered by an aircraft traveling with a supersonic speed, over the speed of sound in a medium. Figure 2.9 provides a picture of a Mach shock wave induced by a sharp-nosed supersonic object.

Figure 2.10 explains the reason why the Mach shock wave has such a conical geometrical feature. The aircraft traveling at velocity v produces a spherical pressure wave, or sound wave. The spherical wave propagates at the speed of sound in the medium, in this case, the air. When the aircraft travels slower than the speed of sound ($v < v_{\rm s}$), there is no overlapping between the radial pressure waves, but the density of the waves is disturbed forwards and backwards. Suppose an observer stands nearby the moving object, then one can feel the Doppler effect [97]; the observer hears different sound frequencies when standing in front/rear of the object.

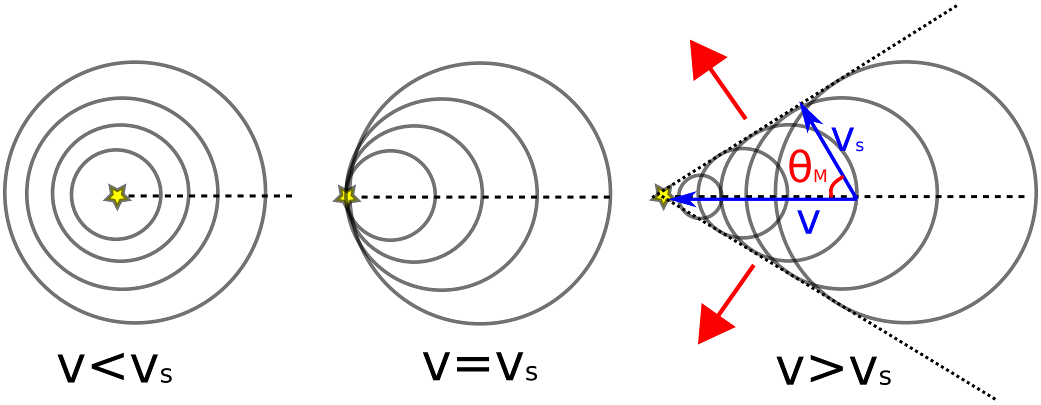

Figure 2.10: Schematics of a Mach shock wave with three different speeds of the moving object.

When the object moves at the sonic speed ($v = v_\mathrm{s}$), the radial waves overlap, starting at the front edge of the object. The large amplitude of the pressure wave is formed by a pile of the waves, called sonic barrier [98].

When the speed of the object exceeds the speed of the sound ($v > v_\mathrm{s}$), it instead produces a flat surface having a conical shape at the center of the movement direction of the object. Like the sonic barrier, a huge amplitude of the pressure wave is produced at the overlapping surface. It transmits the energy induced from the accumulation of the radial pressure waves onto the surface direction, shown as red arrow in Fig. 2.10. This is called the Mach shock wave.

The opening angle (θ_M), called the Mach angle, between the flight direction of the airplane and the direction of the shock wave can be represented as the ratio of the speeds

$$\cos\theta_\mathrm{M} = \frac{v_\mathrm{s}}{v} \tag{2.5}$$

where v is the speed of the object, v_s is the speed of sound.

Similarly the Mach cone can also be created with an object traveling faster than the speed of light in a certain medium, instead of the speed of sound. In this case, instead of the shock wave of sound, what we can observe is the shock wave of light. Such radiation has been commonly observed as blueish light in an underwater nuclear reactor as shown in Fig. 2.11. Simply, the difference between a Mach shock wave and Cherenkov radiation is the form of the transferred wave; sound and light.

As defined earlier, the Mach angle can also be calculated by the ratio of the speed of light in the medium and the speed of the charged particle [100]:

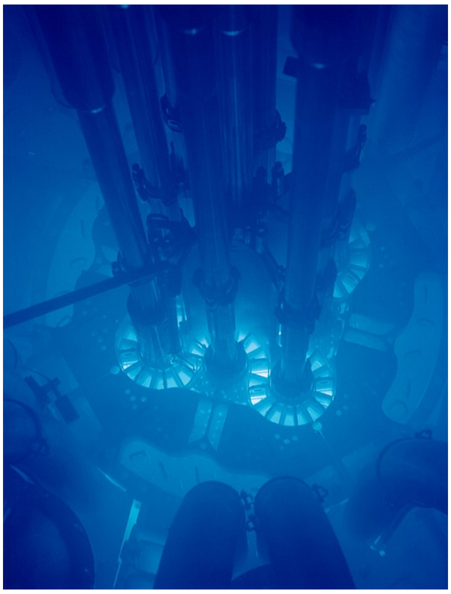

Figure 2.11: Picture of Cherenkov radition glowing in the core of the Advanced Test Reactor (figure taken from [99]).

$$\cos\theta_{\mathrm{c}} = \frac{v_{c,\ medium}}{v} \tag{2.6}$$

The speed of light in a medium is given:

$$v_{c,\ medium} = \frac{c}{n} \tag{2.7}$$

where n is the refractive index of the medium. Finally, the Cherenkov radiation angle is described as:

$$\begin{aligned} \cos\theta_{\mathrm{c}} &= \frac{c/n}{\beta c} \\ &= \frac{1}{n\beta} \end{aligned} \tag{2.8}$$

with n, the refractive index, and β, the velocity of the charged particle. Suppose we know the refractive index of the material and measure the Mach angle induced by an unknown charged particle. We can then calculate the velocity of the particle. If this is combined with the momentum information of the particle, it can be used as a method to identify the particle species. The High Momentum Particle Identification Detector (HMPID) in the ALICE detector uses Cherenkov radiation for particle identification [101].

This sort of shock wave in various mediums is universal. Mach cone studies are

	Ideal gas	sQGP	Hadronic matter
v_s (in units of c)	$\sqrt{1/3}$	$\sqrt{2/3}$	$\sqrt{1/5}$
θ_M (in radian)	54.8° (0.96)	66.4° (1.16)	70.0° (1.22)

Table 2.1: Expected Mach angles for various phases of hadronic matter. The 'sQGP' term indicates a strongly interactive QGP medium. v_s is the speed of sound in a medium. v_s values for ideal gas, sQGP, and hadronic matter are taken from [107, 108, 109].

available in solid state physics with complex plasma crystals [102, 103, 104] and in biology with a living body [105, 106]. Therefore, a Mach shock wave can also be produced in the QGP medium.

2.3.2 QGP Mach cone

Jets propagate through the QGP medium with a high speed close to the speed of light. Hence, there is a fast-moving object (jet) and an interactive medium (QGP). As an analogy, the Mach cone can be generated by a jet in the QGP medium, as described above.

If a Mach shock wave is generated around the jet, it transfers the energy on the shock wave front. The transferred energy undergoes the medium evolution like the QGP itself. Since additional particles are produced along the Mach shock wave front, they have an evident angular correlation to the jet axis, in other words, they all have the same opening angle (Mach angle) to the axis. Therefore they can be observed by the angular correlation analysis.

From Eq. 2.5, the Mach angle, θ_M, is given by:

$$\theta_\mathrm{M} = \arccos\left(\frac{v_\mathrm{s}}{v_\mathrm{jet}}\right) \tag{2.9}$$

where v_s is the speed of sound in a medium and v_jet is the speed of a jet. As jets traverse the QGP medium with the speed close to $c \to 1$, we can obtain expected Mach angles based on theoretical predictions of the speed of sound in the QGP. The possible angles are listed in Table 2.1. The ideal gas is the non-interactive medium and the sQGP means the case where quarks and gluons interact strongly in the medium. The hadronic matter indicates the medium consisting of hadrons, which is a phase when the medium temperature goes down than the critical temperature (T_c).

The double-bump peak in two-particle correlation in Fig. 2.8 has been inter-

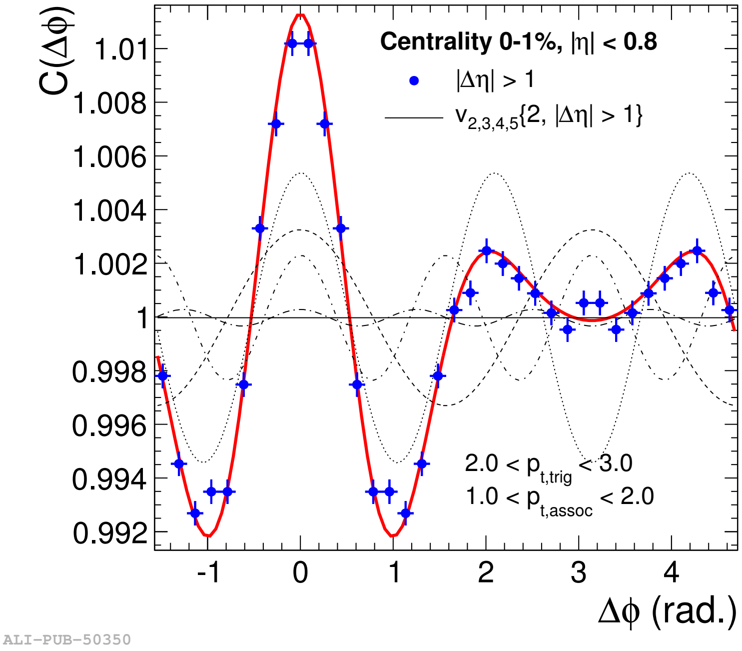

Figure 2.12: Two-particle azimuthal correlation (blue points) and the sum (solid red line) / each one (dashed gray lines) of the anisotropic flow coefficients measured in Pb–Pb collisions at $\sqrt{s_{\mathrm{NN}}} = 2.76$ TeV from the ALICE collaboration. The correlations were measured in $0 < \Delta\varphi < \pi$ and extended symmetrically over 2π. (figure taken from [115]).

preted as a signal of a Mach cone in the QGP [110]. After the first observation of the double bump, lots of studies regarding this phenomenon have been performed in theory and experiment [111, 109, 112, 113, 114]. However, a recent flow result added another perspective on the double peak. Figure 2.12 shows the summation of the contribution of different flow coefficients.

The summation distribution also exhibits two peaks on the away side ($\Delta\varphi > \frac{\pi}{2}$), which does not require the Mach shock waves to explain the two peaks. Although, Shuryak and Staig still argued the possibility of the Mach shock wave in QGP [116, 117]. They also studied the model predictions of a sound/shock wave propagation in the QGP medium based on hydrodynamics [118, 108, 119].

Figures 2.13 and 2.14 show model predictions of a shock wave propagation and induced temperature changes by jets depending on the position of the shock wave and on the viscosity-to-entropy density ratio of the QGP. The model predictions clearly show the possibility of a Mach shock wave (or sound perturbation) in the QGP medium. However, its signal is sensitive to the position of the sound perturbation (equivalent to jet position in the QGP medium, fireball) and the medium properties, like viscosity.

To develop the theoretical studies of the Mach shock wave, inputs from the experimental side are essential. In the following, our specific analysis approach to search for evidence of a Mach cone in the QGP is described.

2.4 Angular correlation with respect to the jet axis

The particles produced by the Mach shock wave (called the Mach cone in the following) have the same angle (the Mach angle) with respect to the jet (or parton) direction. The angular correlation analysis is the preferred method to analyze the angular relationship. In the past, high p_{T} particles were used as a trigger particle in two-particle correlation analyses, instead of jets [89, 91, 92, 120], since high p_{T} fragments tend to be more collimated to the original jet axis. However, it is not necessary to use high p_{T} particles as proxy of jets because more direct observable (jet) was accessible for this analysis. Therefore, jets were used for the correlation analysis in this work.

2.4.1 Jet-hadron correlations

Jet-hadron correlations show the angular difference of particles with respect to the jet axis, a proxy of the direction of hard scattered parton. Here, the main interest is estimating the direction of the hard scattered parton, which makes the Mach cone in the QGP. The parton's direction can be estimated by the vector sum of all fragments in the jet originated from the parton. Although the estimation can be biased due to the limitation of the jet clustering algorithm (explained in Sec. 3.5.4), it is still a much more accurate proxy of the parton direction, compared to that based on the high p_{T} particles. The preceding study was done by Jochen Klein [121] with the data measured in Pb–Pb collisions in 2011, but the study could not draw a conclusive statement due to the limitation of statistics. Therefore, in this work, the jet-hadron correlations was studied with much higher statistics, for example, Pb–Pb collisions in 2015.

2.4.2 Transverse momentum range for analysis

Shuryak *et al.* [108] wrote that the sound propagation signal is more significant in a particular kinematic range, $p_{\mathrm{T}} \sim 2$ - 4 GeV/c. When the origin of the jet propagation is close to the surface of the fireball, the sound signal is more observable since smearing effects due to the phase transition are avoided. In this kinematic window, hadrons are more likely to come from jets that make sound signals near

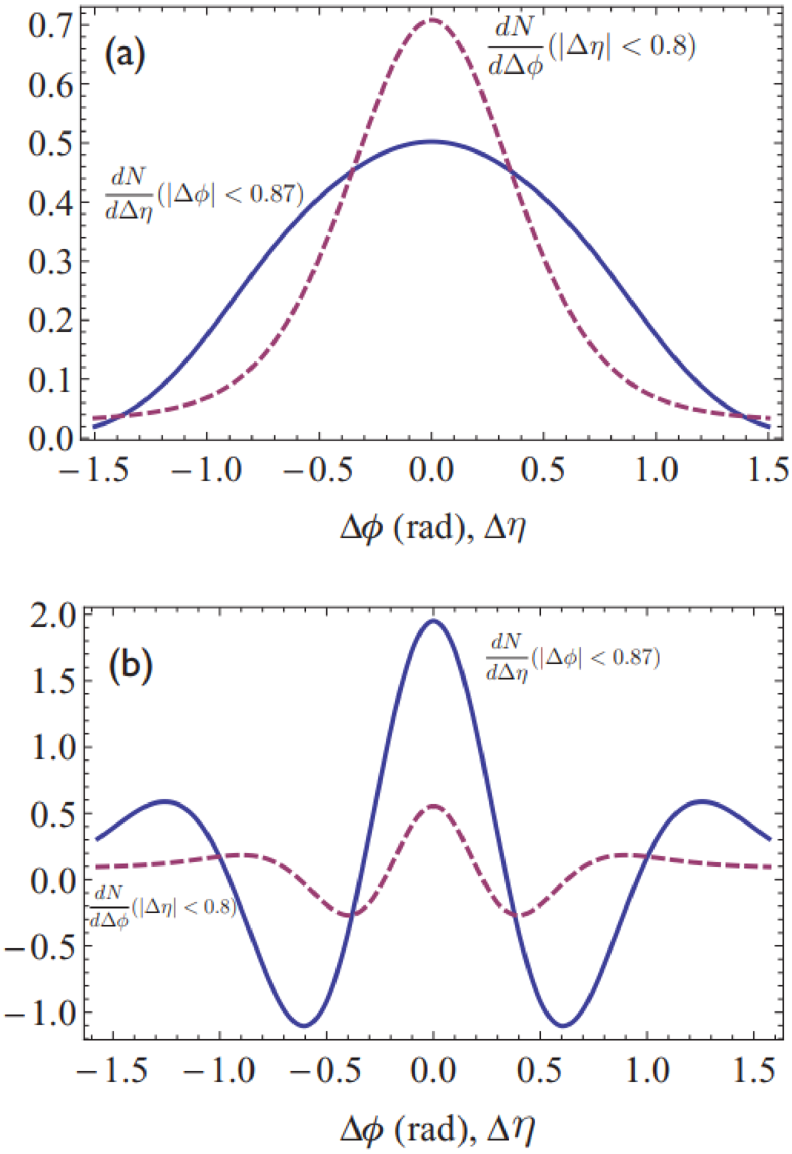

Figure 2.13: Theoretical prediction for two-particle correlation functions. The upper and lower plots show different cases that the Mach cone-like signal is produced at (a) r = 6 fm and (b) r = 6.5 fm from the center of the fireball. The solid blue line shows the correlation in $\Delta\eta$ with $|\Delta\varphi| < 0.87$, and the dashed magenta line represents the correlation in $\Delta\varphi$ with $|\Delta\eta| < 0.8$. Single-particle distribution functions for two-particle correlations are normalized to 1. (figure taken from [119]).

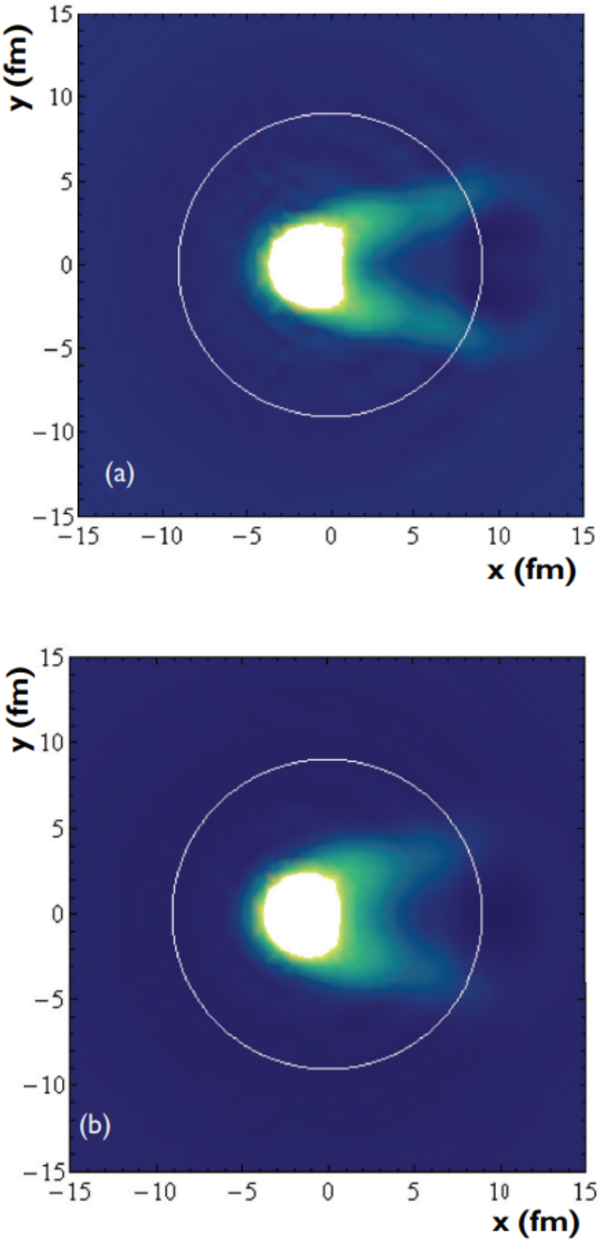

Figure 2.14: Simulation of the temperature change caused by a jet. In the simulation, the jet was initially generated at x = 6.1 and y = 0 and moving to the left side with the speed of light. The upper and lower plots show different energy deposition from jets and the viscosity of the QGP medium. (a) (upper plot) shows the case that the energy deposition $\mathrm{d}E/\mathrm{d}x = \text{const}$ and the viscosity is zero. (b) (bottom plot) shows the case that $\mathrm{d}E/\mathrm{d}x \sim x$ (travel distance) and the viscosity-to-entropy density ratio, $4\pi\eta_{shear}/s = 2$. (figure taken from [108]).

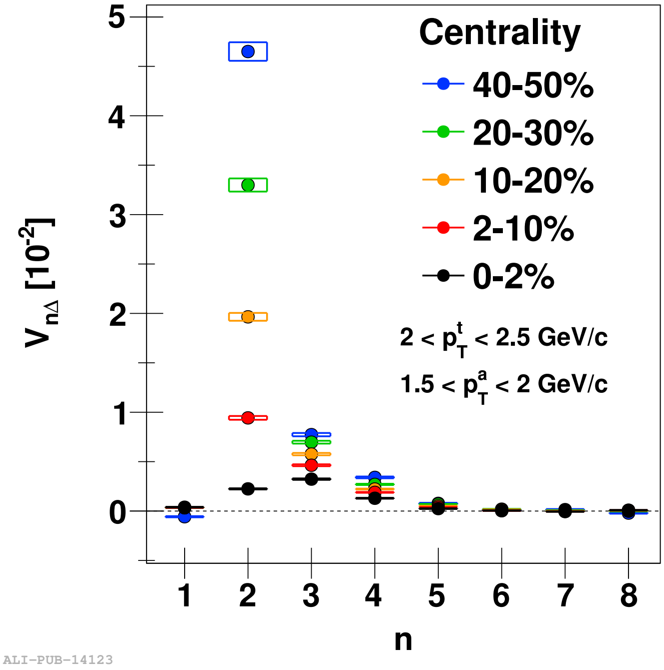

Figure 2.15: Extracted flow coefficients from different centrality bins in Pb–Pb collisions. (figure taken from [122]).

the edge of the fireball [108, 119]. Moreover, it was proposed that the front of sound signals is measurable in the given range, since the signals are boosted by flows [108]. Therefore, the suggested momentum range, 2 - 4 GeV/c, was used in this work.

2.4.3 Flow effect

As described in the previous section, the flow effect from the QGP medium is the predominant background source in this analysis. Since the flow is originated from the collision geometry for v_2 and the density fluctuation at the initial collisions for $v_{n>2}$, it shows a much lower amplitude in central collisions [122]. Figure 2.15 shows the magnitude of each flow coefficient in different centrality bins. v_2 (almond-shaped density) has a more substantial contribution than the others. v_3 (triangular) and v_4 (quadrangular) are the following contributions. These coefficients are reduced substantially in more central collisions. The most central events (0 to 10 %) are selected and analyzed in this research to suppress the flow contribution.

2.4.4 Jet-proton correlations

Jet-hadron correlations with the analysis strategies discussed above are enough to study the Mach cone in the QGP. Nevertheless, this study also proceeded with a jet-proton correlation analysis to comprehend the fragmentation contribution in the correlation function. Fragmentation occurs around the hard scattered parton, and it is one of the parts of jet production. Therefore, it is one of the elements making a peak structure in the correlation function. However, the focus of this work is the medium-produced particle, possibly relevant to Mach cone in QGP, rather than the fragmentation. Baryon (proton) abundance in the QGP is employed to enhance the signal from the medium.

It is known that baryons are more often created in heavy-ion collisions compared to the baryon production in proton-proton collisions. This is understood as the QGP medium contribution because three quarks can be combined much easier in the QGP state. Figure 2.16 shows the baryon (Λ) to meson (K^0_s) yield ratio in Pb–Pb collisions. Different colors represent different contributions to baryon production. Colored points (blue and red) are from jet fragmentation, and inclusive (black) results contain the QGP medium effect and fragmentation. There is a significant difference of the baryon enhancement between the inclusive and the jet cases. Through this phenomenon, when the jet-proton correlation is explored, it is expected for the proton correlation to follow the highlighted medium signals rather than the hadron correlation.

According to the above reasoning, jet-hadron and jet-proton correlation analyses were performed in Pb–Pb collisions measured in ALICE (see Ch. 4 and Ch. 5). Newly developed methods to study the expected Mach cone signal shape in the correlation function and exclude the flow with hadron-hadron correlations with the away-side tracks are discussed in Ch. 6.

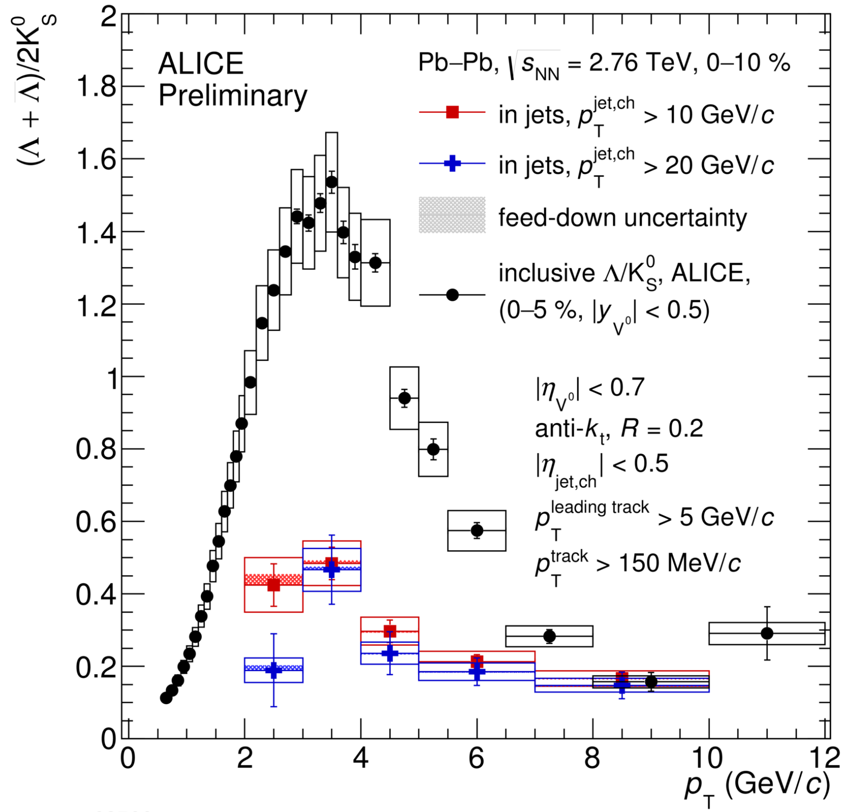

ALI-PREL-93799

Figure 2.16: Λ to K^0_s ratio measured in Pb–Pb collisions. The colored points (red and blue) are the particle ratio from the jet fragmentation, and the p_T cuts for jets are different, 10 GeV/c and 30 GeV/c, respectively. The black points shows the inclusive ratio containing both QGP medium effect and fragmentation. (figure taken from [123]).

3 Experimental setup

3.1 ALICE collaboration

A Large Ion Collider Experiment (ALICE) is one of four large experiments (ALICE [101], ATLAS [124], CMS [125], LHCb [126]) at the Large Hadron Collider (LHC) [127]. It is an international collaboration consisting of 176 institutes and about 2000 collaborators from 41 countries worldwide. Its primary research aims to investigate the properties of the Quark-Gluon Plasma (QGP) produced in heavy-ion collisions.

The ALICE collaboration was formed in 1993, and the LHC committee approved it for design and construction in 1997 [101]. After decades of research and development efforts for detectors, ALICE measured data from the first pp collisions in 2009 and the first Pb–Pb collisions in 2010 at the LHC. It worked successfully during the LHC Run 1 (2009-2013) and Run 2 (2015-2018) periods [128]. The present analysis has been done with recorded data from Pb–Pb collisions in 2015.

3.2 ALICE coordinate system

ALICE has a right-handed Cartesian coordinate system with the origin $(x, y, z) = (0, 0, 0)$ at the designed beam interaction point [129]. The beam interaction point is a technical term to describe the point where the proton (or lead) beam is crossing with the anti-proton (or anti-lead) beam. So, it corresponds to the collision point in experiments.

The z-axis is along with the beam pipe, pointing away from the muon trackers, as shown in Fig. 3.1. The half of the detectors on the positive z is called the A-side, while the other is called the C-side. The x-axis is perpendicular to the beam direction (z-axis), and the positive x is pointing left on the z-axis, facing to the A-side. The positive x is from the origin point toward the LHC center, and the negative x is outward. The y-axis is also perpendicular to the x and z axes, and the positive y points upward toward the surface, and the negative y points downward.

The azimuthal angle (φ) between the x and y-axis counts clockwise, facing the A-side. $\varphi = 0$ on the positive part of x-axis and $\varphi = \pi/2$ on the positive part of y-axis. The polar angle (θ) increases from the positive part of the z-axis (A-side), towards the $x - y$ plane. $\theta = 0$ on the positive part of z-axis (A-side), $\theta = \pi/2$ on the $x - y$ plane, and $\theta = \pi$ on the negative part of z-axis (C-side). The longitudinal direction means the beam (z) direction, and the transverse plane indicates the $x-y$ plane.

For hadron collisions, the initial conditions are usually described in the center of mass system, like (E, p). Detectors measure produced particles from collisions in the laboratory system. Therefore, Lorentz invariance is a useful feature in experiments. In this context, a Lorentz invariant quantity, the rapidity is used. The rapidity is defined as:

$$y = \frac{1}{2}\ln\left(\frac{E+p_z}{E-p_z}\right) \tag{3.1}$$

where E is the energy of a particle, p_z is the longitudinal momentum of the particle along the z-axis and the midrapidity refers to $y = 0$. The pseudorapidity (η) is related to the rapidity and defined as:

$$\eta = -\ln[\tan(\frac{\theta}{2})] \tag{3.2}$$

with the polar angle, θ. Since the pseudorapidity is calculable without the knowledge of the particles' energy and is equivalent to the rapidity for mass-less relativistic particles ($m = 0$), the pseudorapidity is widely used in experiments. For $\eta = 0$, the polar angle of a particle is 90°, and for $\eta \rightarrow \infty$, the polar angle is 0°.

3.3 Detectors in ALICE

As shown in Fig. 3.1, ALICE mainly consists of cylindrical-shaped detectors at mid-rapidity and muon trackers in the forward direction, on the C-side. Its total size is $16 \times 16 \times 26$ m^3 and the weight is about 10,000 t [128].

The central barrel is fully surrounded by a solenoid magnet taken over from the LEP (Large Electron-Positron Collider) L3 experiment at CERN. The magnet supplies a static B field (nominal value, 0.5 T) parallel to the beam axis in the experiment. It makes particle trajectories bent depending on each particle's electrical charge and momentum (specifically, the ratio of momentum to mass), which helps to distinguish the tracks and to identify particles' species.

The function of each sub detector is as following: (1) the central barrel detectors (ITS - Inner Tracking System, TPC - Time Projection Chamber, TRD - Transition Radiation Detector, TOF - Time of Flight), having a full azimuthal coverage, provide particle tracking and particle identification; (2) The muon trackers dedicated to muon measurements; (3) The sub detectors close to the beam pipe (V0, T0, PMD - Photon Multiplicity Detector, FMD - Forward Multiplicity Detector, and ZDC - Zero Degree Calorimeter), used for multiplicity measurements and event triggers; (4) Calorimeters (EMCal - ElectroMagnetic Calorimeter, DCal - Di-jet

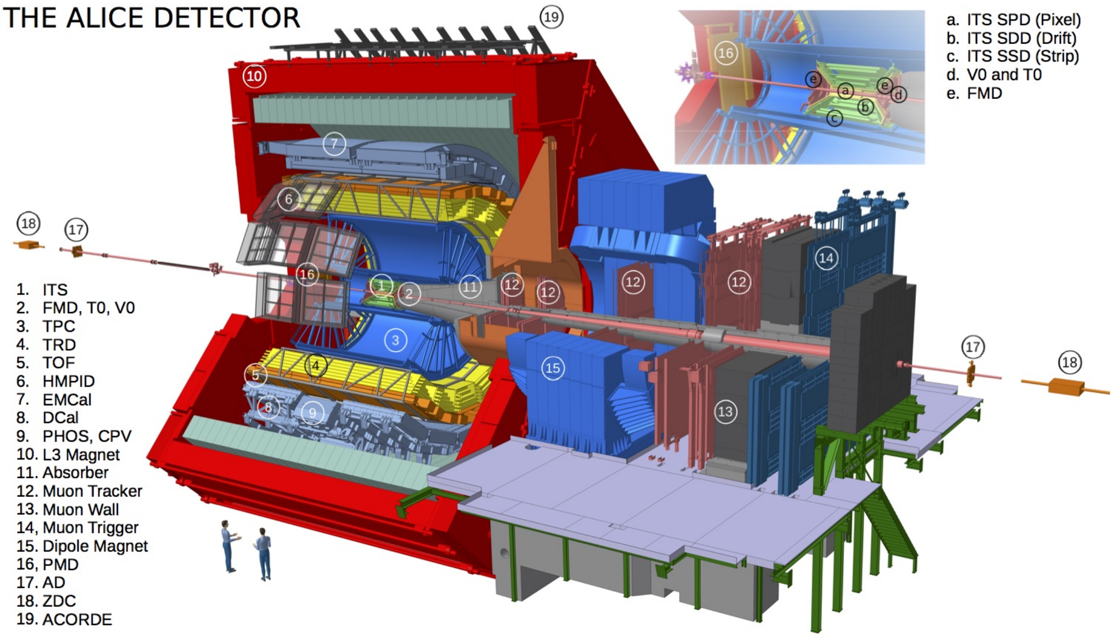

Figure 3.1: Schematic of the ALICE detector. (figure taken from [130]).

Calorimeter) measure energy deposit from neutral and charged particles.

In the following section, only the relevant detectors for the present analysis are described.

3.3.1 V0

The V0 system is made of two disk-shaped scintillator arrays positioned asymmetrically (V0A and V0C, $z = 329$ and 87 cm) close to the collision point [131, 132]. It covers a large pseudorapidity range (η) from 2.8 to 5.1 for the A-side and -1.7 to -3.7 for the C-side. Thanks to its position and much faster readout than other detectors, it has a crucial role in the trigger system of ALICE. The highest momentum, p, particle is likely to fly along the beam direction because it carries a large portion of the momentum from the colliding nuclei. It leaves a signal in the V0, which is used as a trigger signal for the ALICE system. The fast readout of the V0 allows us to transfer the trigger signal to other detectors with minimized dead time and start measurements efficiently.

The V0 is also employed in multiplicity measurements, and its multiplicity determines the centrality classification of the collision. See more information in Sec. 3.5.1. The V0 multiplicity is also used to find pileup events based on the multiplicity correlation with other slow detectors like the TPC. Related analysis is discussed in Sec. 4.2.3.

3.3.2 Inner Tracking System (ITS)

The ITS is a six-layered cylindrical-shaped silicon detector and is positioned closest to the beam pipe [101, 133]. The layers have radii from 4 cm to 44 cm. A combined acceptance coverage is ± 0.9, but the first layer has a more extended coverage, ± 1.98 to help multiplicity measurements with the FMD.

It consists of three different types of silicon detectors: pixel (SPD), drift (SDD), and strip (SSD). The innermost two layers are the SPD, and then the SDD and the SSD follow. The SPD requires high granularity due to the large track density. The individual pixel size is 50×300 μm in $r\varphi$ and the z-directions, providing 100 μm spatial resolution and a good signal-to-noise ratio. The SSD and SDD provide a 2-D spatial reconstruction with strip sensors. By measuring the drift time of electrons created by a charged particle, the x, y positions where the charged particle passed are reconstructed. The SDD and SSD, in particular, measure particle energy loss ($\mathrm{d}E/\mathrm{d}x$), which enables the identification of particle species.

Since primary particles are measured in the innermost ITS layers, it is exploited to find a primary vertex in the collision. Furthermore, the ITS is also used in the general tracking procedure to find particle trajectories. During Run 1 operations, some sectors of the ITS drift detector were damaged and not usable. To avoid the impact of the damaged part in the general tracking, a set of tracks, called hybrid tracks, is employed in many analyses, as described in Sec. 4.3.1.

3.3.3 Time Projection Chamber (TPC)

The TPC is placed in the central barrel and has a cylindrical geometry with an inner radius of 85 cm and an outer radius of 250 cm [134]. The diameter and the length (z-axis) are 5 meters. The TPC η coverage is ± 0.9 for long tracks, and it has full azimuthal coverage. As a gas chamber detector, a mixture of Ar (88%) and CO_2 (12%) is employed [135]. In the middle of the TPC, the central electrode is placed to apply an uniform axial electric field with 100 kV in the TPC volume. Multi-Wire Proportional Chambers (MWPC) with cathode pads are used as the readout. The MWPC is divided with the Inner Read-Out Chambers (IROC) and the Outer Read-Out Chambers (OROC). They have different pad sizes 4×7.5 mm^2 ($r\varphi \times r$) for the IROC and 6×10 and 6×15 mm^2 for the OROC. The total number of readout channels is 557,568.

When a charged particle passes through the TPC gas volume, it produces electrons and ions via ionization. Due to the electric field inside the TPC, the created electrons/ions drift toward the MWPCs in the endcaps. The collected signal in each readout channel gives the x, y coordinate of the charged particle. And due to the static electric field, the z position can be obtained by the drift time together with the collision time provided by the T0 and the calibrated drift velocity. The deposited charges of the individual channels indicate energy loss of the charged particles in the TPC. Such information is vital in the general tracking and particle identification in ALICE.

3.3.4 Time of Flight (TOF)

The TOF detector is in the central barrel and has a cylindrical geometry with its inner radius of 3.7 m [136, 101]. Its coverage in η is ± 0.9, and the entire detection area of the TOF is 141 m^2. The TOF consists of 1593 Multigap Resistive Plate Chamber (MRPC) strips and is exploited to measure the flight time of particles. When a charged particle creates the ionization on the resistive plate, the signal is immediately amplified through the electron avalanche due to the applied electric field and measured as an arrival time. Since the collision time is measured by the T0, the time of flight can be calculated as the difference between the arrival time on the TOF and the start time on the T0. Thanks to the tracking detectors (ITS and TPC), the flight path of particles is measured. Combined with the path length and the time, the particle velocity (β) is obtained and used for particle identification. The time resolution is 80 ps.

3.4 ALICE Analysis software

For data analysis of particle and nuclear physics, a software package called ROOT is widely used [137, 138]. It is an open-source program and library developed by CERN and written in C++. As ROOT was originally designed for high-energy physics analysis, it enables us to work with massive amounts of data from experiments and contains plentiful functions and features for research. It helps us from data acquisition to visualization of data in the experiments.

AliROOT is based on ROOT with additional libraries and functions dedicated to the ALICE experiment. While AliROOT is a computational tool for analysis, AliPhysics is a supplementary library consisting of physics-oriented objects and functions. It includes two different types of databases, OADB (Offline Analysis DataBase) and OCDB (Offline Condition DataBase). The OADB contains correction and calibration information for analysis observables. The OCDB includes detector-oriented correction and calibration information. All data analyses in ALICE have been performed with AliROOT and AliPhysics [139].

Since the software is maintained and consistently developed by ALICE users, it is stored and updated with daily tags. In the present analysis, AliPhysics version vAN-20200421-1 and the compatible AliROOT-5 were used in the analysis process. AliROOT-6 was utilized partially for the visualization process in the drawing macros because it is more convenient to use PyROOT scripts (a Python-based wrapper for ROOT).

The AliEmcalFramework is one of the classes designed for jet-related analysis in AliPhysics. The framework contains primary selections for events and tracks and the jet reconstruction process (with the Fastjet package [140]) so that analyzers can quickly access the reconstructed jets in their analysis task. The analysis script for the present research was written in the AliEmcalFramework and employed reconstructed charged jets in the present research.

To operate the analysis task code, the Worldwide LHC Computing Grid (WLCG) system, called the Grid, has been used. It is a project of global computing resources organized by CERN, consisting of clusterized computers worldwide. Find details about the Grid in this [141].

3.5 Analysis

This section introduces the basic analysis procedures, such as centrality determination, general tracking procedure, particle identification and jet clusterization, which are widely used in the ALICE collaboration for the analysis of identified particles and jets.

3.5.1 Centrality determination

As briefly discussed in Sec. 1.3.2, the initial geometry of a heavy-ion collision affects the properties of the collision result, like flow effects. A fundamental value to describe the collision geometry is the impact parameter. The impact parameter, b, is defined as the distance between the nuclei centers of the colliding ions in the transverse plane, as shown in Fig. 3.2. When a collision is head-on, the impact parameter is zero or close to zero. In this case, the overlapping area between the colliding ions is maximal, having the maximum number of participants. On the other hand, a collision with larger b value means a smaller overlapping area between the ions having fewer participants. Depending on the collision geometry, the number of participants ($\mathrm{N_{part}}$), the number of nucleon collisions between participants ($\mathrm{N_{coll}}$) and the cross-section of inelastic collision ($\sigma^{\mathrm{tot}}_{\mathrm{inel}}$) are different. Furthermore, the shape of the overlapping area influences the flow. These effects change the number of produced particles (multiplicity) as well. High multiplicity results from a larger overlapping area with small b, while low multiplicity comes from a smaller overlapping area with large b. To distinguish different physical effects from different collision geometries, one should handle experiments depending on the collision geometry.

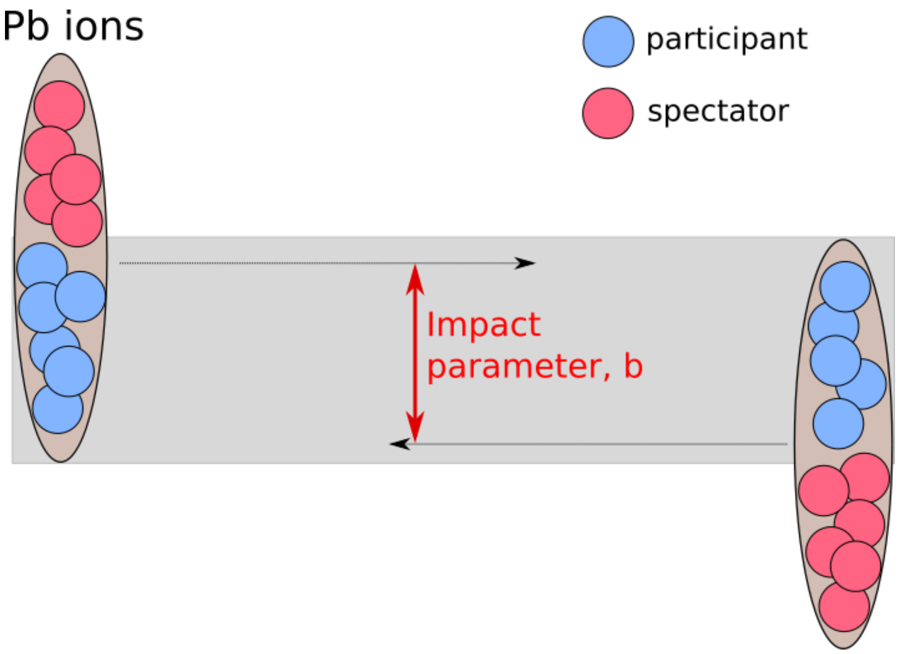

Figure 3.2: Impact parameter, b, in Pb–Pb collosion.

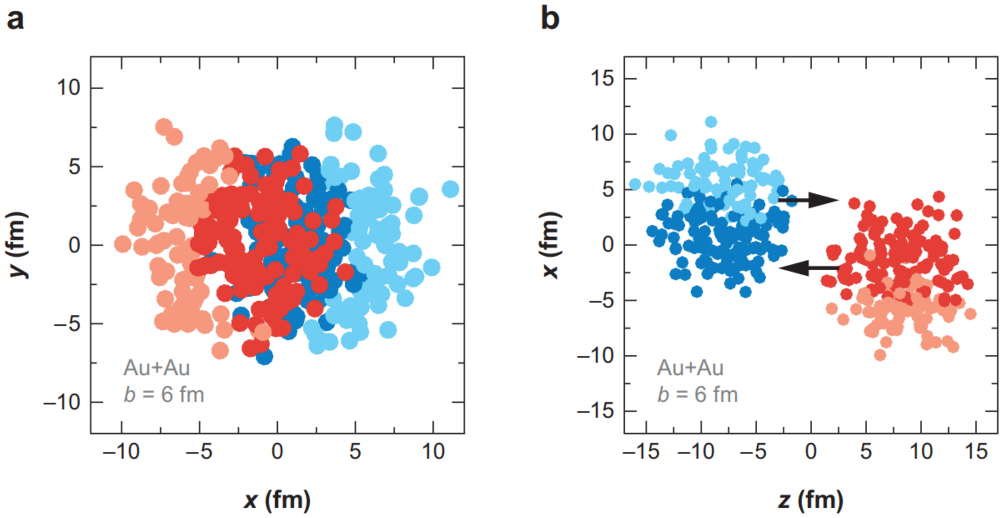

Figure 3.3: Examples of Glauber model simulation for Au–Au collision. (a) (left) nucleons distribution on the $x - y$ plane. (b) (right) nucleons distribution on the $x - z$ plane. The impact parameter for the collision is 6 fm. Dark red and blue points are participants in the collisions. (figure taken from [142]).

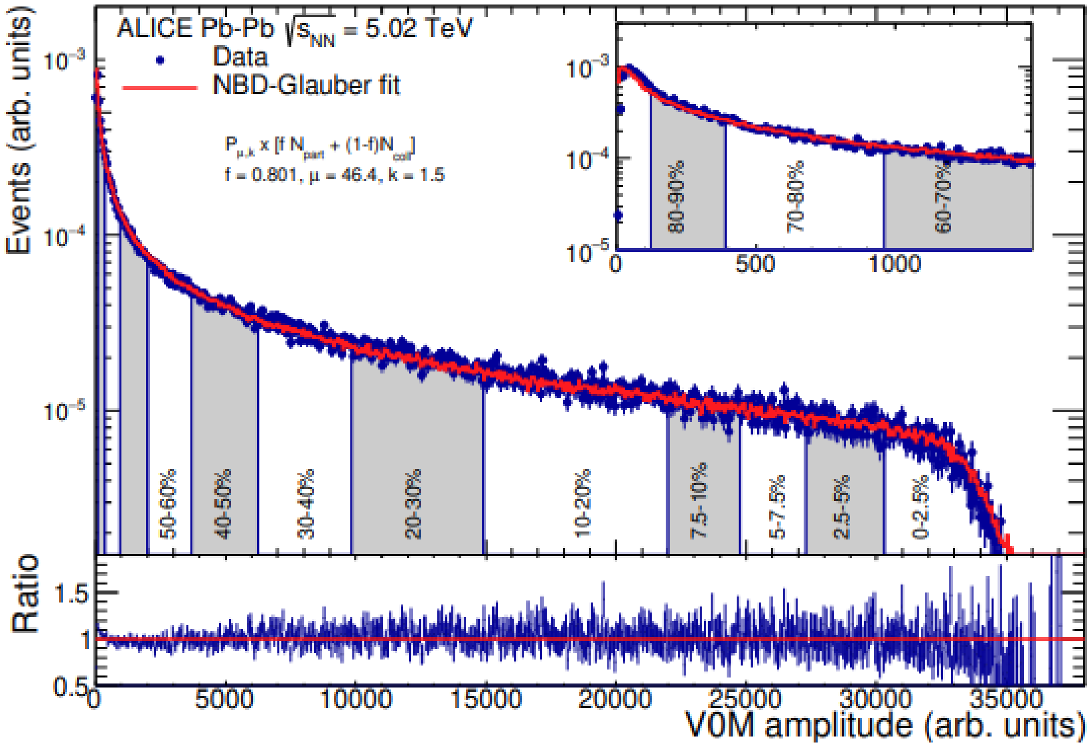

Figure 3.4: V0 multiplicity distribution with NBD-Glauber fit result. (figure taken from [132]).

Since the impact parameter is not accessible in experiments, centrality is used to describe the collision geometry. As multiplicity has a correlation with the collision geometry, the centrality is defined as the percentage of the multiplicity event. In this analysis, the V0 multiplicity was used to calculate the centrality. To estimate non-accessible parameters, like $\mathrm{N_{part}}$, $\mathrm{N_{coll}}$, and $\sigma_{\mathrm{inel}}^{\mathrm{tot}}$, the Glauber model is employed. In this model, a basic assumption is that a common probability density of nucleon $\rho_{\mathrm{A}}(x, y, z)$ is given in colliding ions, and is not changed by individual collisions. And the integrated value over the beam direction, $T_{\mathrm{A}}(\vec{s}) = \int \rho_{\mathrm{A}}(\vec{s}, z)\mathrm{d}z$ can be obtained for each ion. As two ions overlap in a collision, the nuclear overlap function can be defined for a given impact parameter $\vec{b}$:

$$T_{\mathrm{AB}}(b) = \int T_{\mathrm{A}}(\vec{s})T_{\mathrm{B}}(\vec{s} - \vec{b})\mathrm{d}^2 s \tag{3.3}$$

where A, B indicates a label for colliding nuclei. Based on the Glauber Model, the numerical approach, Glauber Monte Carlo simulation is commonly used. In the simulation, nucleons are initially distributed according to the density profile for different b, as shown in Fig. 3.3. By iterating the simulations sufficiently, the values for $\mathrm{N_{part}}$ and $\mathrm{N_{coll}}$ for a given b can be extracted.

Figure 3.4 shows a multiplicity measurement with the V0 and the Glauber MC result with a Negative Binomial Distribution (NBD). To obtain the measured multiplicity from the Glauber MC, a particle production model based on the negative binomial distribution is employed. As mentioned above, the centrality is defined as the percentile of the V0 multiplicity events, which is shown as the percentage values in Fig. 3.4. Except for the low multiplicity region at less than 1000, the non-hadronic collision region, the measured multiplicity by the V0 and by the Glauber MC are in good agreement within statistical fluctuations. Thanks to the Glauber simulation, non-accessible parameters, like $\mathrm{N_{part}}$ and $\mathrm{N_{coll}}$, in the given centrality are calculated from the simulation. And using the Glauber result, the anchor point (AP) for 100% is defined to get a percentage of the centrality in the measurement. Since actual measurements are affected by detector efficiency and signal threshold and so on, the Glauber result provides the AP point expecting to the impact parameter close to zero. When the centrality is close to 0, it represents a very central collision. When the centrality is higher, it means a peripheral collision. The present analysis is done in 0 - 10% centrality.

3.5.2 General tracking procedure

Track reconstruction means making a complete expected trajectory of a flying particle based on the point-like signals in the tracking detectors. The reconstruction starts with a location in the outer barrel of the TPC, and moves inward through the TPC. The reason for beginning from the outer side is due to the density of

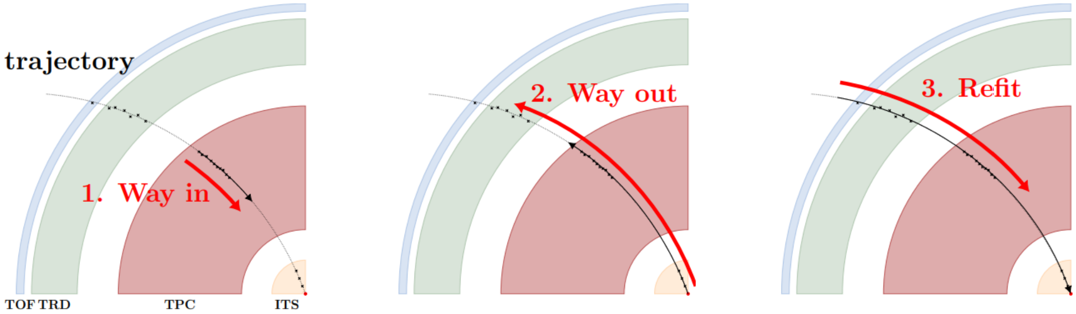

Figure 3.5: Diagrams of the general tracking procedure. The track reconstruction procedure starts with the outer barrel of the TPC and moves inward, to the ITS. After that, the tracking procedure repeated outward, from the ITS to the TOF. The final refit is done with all clusters in the tracking detector. (figure taken from [143]).

tracks. More tracks are closely packed in the given volume when it is close to the primary vertex. In the outer regions of the TPC, tracks have enough distance between each other to separate them distinctly. Such a less-dense condition allows us to get a plausible expected trajectory conveniently.

At the beginning of the reconstruction process, 3 TPC clusters (3 signals in the TPC outer layers) and the primary vertex are used for the fit. Based on the Lorentz force in the given magnetic field in the ALICE detector, an initial trajectory between the 3 TPC clusters and the primary vertex is obtained. Since the first fit line would be not perfectly matched with the next clusters, therefore by using the first trajectory, the track was reconstructed with the next 3 TPC clusters in the inward direction. For the track reconstruction, a Kalman filter [144] was used to merge the following 3 TPC clusters (the measurement) and the prediction from the previous fit, to obtain a weighted average between the prediction and the measurement. By using the weighted signal points, an improved prediction of the trajectory is obtained with 6 TPC clusters in the end. By repeating this process, the whole TPC and ITS clusters were fitted by three clusters at a time with the Kalman filter, as shown in Fig. 3.5, left panel.

After the track reconstruction from TPC to ITS (way-in), the same process is repeated again from ITS to TOF (way-out), including outer tracker, the TOF. Finally, the global trajectory was obtained by refitting all available clusters across the four detectors, the ITS, TPC, and TOF. More detailed information about the general tracking procedure can be found [128, 143].

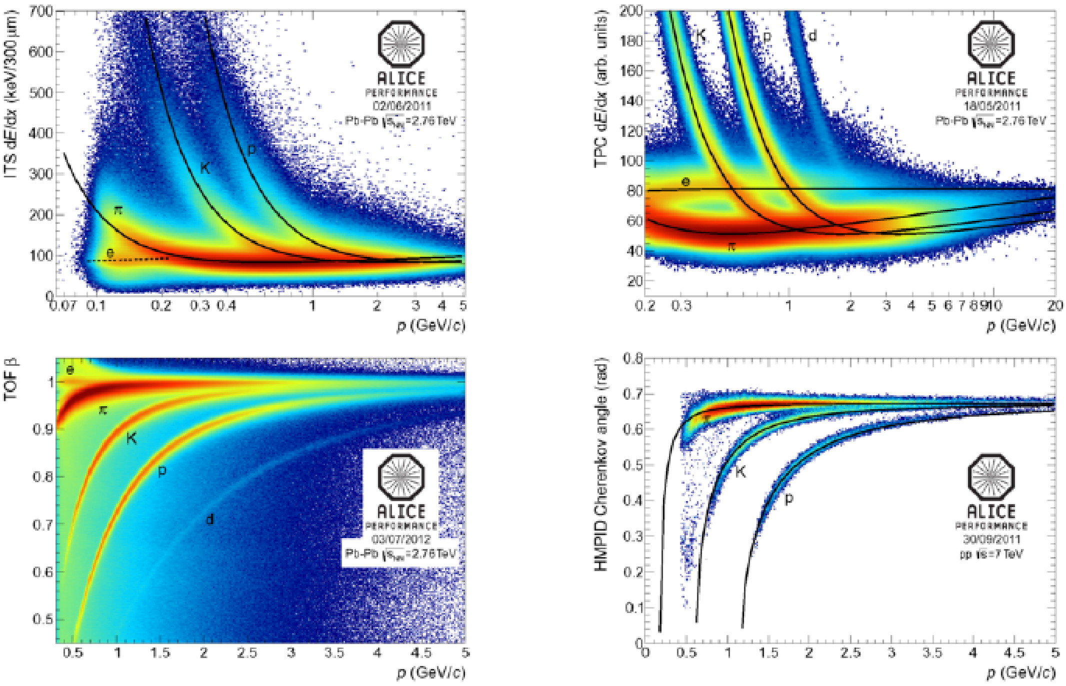

Figure 3.6: Particle Identification performance of the ALICE detectors. From the top left to the bottom right, ITS dE/dx, TPC dE/dx, TOF velocity (β), and HMPID Cherenkov radiation angle. (figure taken from [145]).

Table 3.1: Summary of variables used in the Bethe-Bloch formula

Symbol	Definition	Unit or Value
K	$4\pi N_A r_\mathrm{e}^2 m_\mathrm{e} c^2$ (Coefficient for $\mathrm{d}E/\mathrm{d}x$)	0.307075 MeV mol^{-1} cm^2
z	Charge number of incident particle	
Z	Atomic number of absorber	
A	Atomic mass number of absorber	g mol^{-1}
$m_\mathrm{e}c^2$	Electron mass × c^2	0.5109989461(31) MeV
W_max	Maximum possible energy transfer to an electron in a single collision	MeV
I	Mean excitation energy	eV
β	v/c (velocity)	
γ	$(1-\beta^2)^{-1/2}$ (Lorentz factor)	
N_A	Avogadro's number	$6.022140857(74) \times 10^{23}$ mol^{-1}
r_e	Classical electron radius	2.8179403227(19) fm
δ	Density effect correction to ionization energy loss	

3.5.3 Particle Identification (PID) in ALICE

Particle identification means identifying the species of a particle according to information from detectors. There are four different types of particle identification detectors in ALICE.

One type of detector measures ionization characteristics in the detector volume, like in the TPC. When a charged particle passes through any material, it loses its energy by ionization and atomic excitation. Such energy loss ($\mathrm{d}E/\mathrm{d}x$) is characterized by physical properties of the incident particle and the atomic matter. As shown in Eq. 3.4, the mean energy loss rate is defined according to the Bethe-Bloch function [38] in the given variables defined in Table 3.1. Although there are many parameters in the formula, most variables are fixed by the experimental conditions.

$$\left\langle -\frac{\mathrm{d}E}{\mathrm{d}x} \right\rangle = Kz^2 \frac{Z}{A}\frac{1}{\beta^2}\left[\frac{1}{2} \ln \frac{2m_e c^2 \beta^2 \gamma^2 W_{max}}{I^2} - \beta^2 - \frac{\delta(\beta\gamma)}{2} \right] \tag{3.4}$$

Suppose many particles travel in the TPC gas, having constant Z (gas atomic number) and A (gas mass number). In that case, the mean energy loss of each particle can be illustrated by a single Bethe-Bloch line as a function of $\beta\gamma$. However, if one coverts the mean energy loss rate to the momentum axis by multiplying by the particle mass, the Bethe-Bloch line separates depending on the particle species for a given momentum due to different particle masses. Taking advantage of the Bethe-Bloch line separation, the TPC measures the energy loss of a traveling particle in the TPC volume as a charge.

The DPG provides official TPC splines to analyzers. The process to make official splines is as following: when new data is recorded, the TPC performance Quality Assurance (QA) is performed. The sets of recorded data in continuous measurement, or runs, which passed the QA are listed in the corresponding dataset. With the list, a dedicated analysis task [146] was performed based on the official spline in previous datasets. In the analysis task, pion, kaon, proton and electrons are obtained with different detector combinations ITS, TPC and TOF. V0 particles (secondary particles produced by a decay of primary particles) also used in the process. The reason why different combination of detectors and particles is that $\mathrm{d}E/\mathrm{d}x$ values of those particles are used as a template for the Bethe-bloch fit, so it is important to obtain a high purity in each particle specie. The Bethe-bloch fit was performed on the average $\mathrm{d}E/\mathrm{d}x$ of measured particles as a function of $\beta\gamma$. The obtained Bethe-bloch line from the fit is replicated and separated to each particle species by multiplying the mass of particles. While low momentum tracks travels in the TPC volume, their momenta are largely changed due to the energy loss ($\mathrm{d}E/\mathrm{d}x$). The measured $\mathrm{d}E/\mathrm{d}x$ for those tracks is averaged over different momenta, therefore the $\mathrm{d}E/\mathrm{d}x$ values in the low momentum region have a deviation from the Bethe-bloch line. Therefore, the low momentum correction is needed to the obtained Bethe-bloch lines, and the lines are corrected based on a n-polynomial fit on the measured $\mathrm{d}E/\mathrm{d}x$ at the low momentum range in different particle species. The Bethe-bloch lines corrected the low-momentum effect is called splines. Different track η (precisely, the polar angle θ) implies different inclination of tracks in the TPC volume, which leads to change of effective track length over the TPC pad, modifying $\mathrm{d}E/\mathrm{d}x$ values. This effect shows η dependence of $\mathrm{d}E/\mathrm{d}x$ and should be calibrated. For the calibration, the deviation between the $\mathrm{d}E/\mathrm{d}x$ and the spline as a function of η in a given momentum bin is used. Since there is no dependence of particle species for η calibration, only $\mathrm{d}E/\mathrm{d}x$ of protons are employed. These processes are performed for the splines in pp collisions, and multiplicity dependence is additionally calibrated like η dependence for only Pb–Pb collisions. After the correction and calibration, the new splines and the calibration map for η dependence are produced. Then, the same analysis task is performed again based on the new splines and calibration map to improve the quality of splines and calibration. At least, 4 or 5 iterations are required in each dataset, then the official splines are updated in the ALICE software. This work was done as a service work during the doctoral research. During the work, the splines were produced for all pp collsions in 2017 and several pp and Pb–Pb collisions in 2015, 2016 and 2018.

A deviation between a measurement and prediction (splines) can be calculated for every particle spline. For instance, when we calculate the deviation between the measurement and the pion splines, the deviation can be expressed:

$$n_{\sigma,\mathrm{pion}}^{\mathrm{TPC}} = \frac{(\mathrm{d}E/\mathrm{d}x)_{\mathrm{measured}} - (\mathrm{d}E/\mathrm{d}x)_{\mathrm{expected}}^{\mathrm{pion}}}{\sigma_{\mathrm{expected}}^{\mathrm{pion}}} \tag{3.5}$$

This deviation parameter for pions has a normal distribution with the mean equal to zero and the sigma (σ) close to 1. Other particles are likely to have a value further from zero. Based on this principle, a σ cut can be utilized in the PID process. The commonly used cut value is 2σ. In the normal distribution, the $\pm 2\sigma$ contains 95% of total statistics. $\mathrm{d}E/\mathrm{d}x$ measurements can also be performed in the ITS (SSD and SDD) as well.

The second PID type is a Time Of Flight (TOF) measurement. In the TOF, the arrival time of a particle to the detector is measured. Combined with the T0 measurement of the collision time, the TOF provides the total flight time of a particle from the collision point to the TOF. Thanks to the central tracking detectors, the ITS, TPC, and TRD, the particle's trajectory (track length) and transverse momentum are measured. The velocity of the particle is calculated from the length and the flight time. If one knows the velocity and the momentum of the particle, one can obtain its mass. Each particle species has its distinct mass, so particle identification is possible based on this information. Like the TPC PID, the σ calculation has been done with a deviation between the TOF prediction and the data.

The other two PID detectors are the TRD and HMPID. The TRD employs transition radiation from particles that enables it to distinguish hadrons from electrons by looking into different radiation signal shapes. The HMPID is a RICH (Ring Imaging Cherenkov detector). When a particle produces Cherenkov radiation in the detector volume, the radiation angle is different depending on the particle's species. The angle is estimated from measured ring size on the Photomultiplier Tube (PMT) in the HMPID. Therefore, it allows us to identify the particle in the measurement.

3.5.4 Jet clustering in the experiment

As discussed in Ch. 2, hard scattered partons produce jets. Since jets are a bunch of dense particles in a confined volume, it can be considered as a spray of collimated particles, as well as a high energy concentrated in the volume. Two types of jets are accessible in the ALICE measurement: charged jets and full jets. The charged jets refer to the jets measured by the central trackers. In this case, jets are clusterized based on only the measured charged tracks by the central trackers, so neutral particles cannot be included. The full jets refer to the jets not only measured by

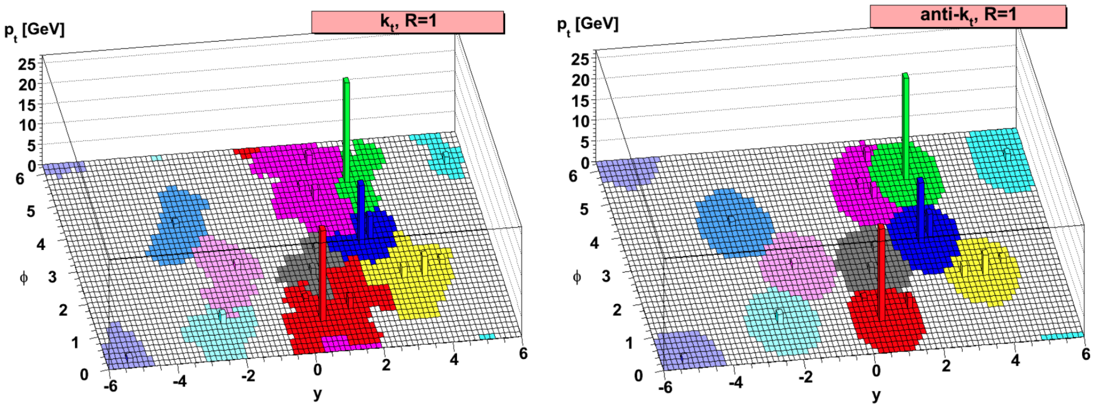

Figure 3.7: Jet clustering with two different jet algorithms (k_T and anti-k_T) in the simulation. Colored areas show clusterized jets' areas. (figure taken from [147]).

the central trackers, but also additionally measured with the calorimeters, EMCal (or EMCal + DCal), and therefore it contains the energy of both the charged particles and also the neutral particles. However not all jets can be measured by calorimeters, because the ALICE detector only have a small coverage of the EMCal, in the azimuthal angle ($80^\circ < \varphi < 187^\circ$). Although taking account of the full energy profile of jets would be beneficial, but due to the insufficient coverage of the EMCal, it cannot be obtained uniformly. Thus, in this analysis we used the charged jets which can be uniformly obtained in the azimuthal angle.

The charged jets can be obtained by jet clustering algorithms. In this analysis, the anti-k_T algorithm [147] was employed for jet clusterization, which is the jet clustering algorithms available from the FastJet computational framework [140]. The algorithm of the anti-k_T works by clustering measured tracks according to the comparison with two defined distances:

$$\begin{aligned} d_{i,j} &= min(p_{\mathrm{T},i}^{2p}, p_{T,j}^{2p})\frac{\Delta_{ij}^2}{R^2}, \\ d_{i,\mathrm{B}} &= p_{\mathrm{T},i}^{2p} \\ \Delta_{i,j}^2 &= (\eta_i - \eta_j)^2 + (\varphi_i - \varphi_j)^2 \end{aligned} \tag{3.6}$$

where i, j are the indices for tracks in a event, and R is the jet radius parameter fixed by analyzers. Suppose that there is a list of measured tracks per event. Starting with the first track in the list, this distance $d_{1,2}$ with the second track and $d_{1,\mathrm{B}}$ can be calculated. If $d_{1,2}$ is smaller than $d_{1,B}$, then the first and second tracks are merged to form a proto-jet, 1. The second track is added to the list of particles for the proto-jet, 1. In the case, $d_{1,2}$ is the same or larger than $d_{1,B}$, the first and second tracks are regarded as two separated proto-jets and the second track is not included in the particle list for the proto-jet, 1. This process can continue with the proto-jets and following tracks until all tracks are clustered into jets or no more merging occurs. This method is called a sequential recombination method. The anti-k_{T} algorithm uses p = -1 and the k_{T} use p = 1. In the anti-k_{T}, clustering starts with the highest momentum track, while k_{T} starts with the lowest momentum track. Figure 3.7 shows jet clustering with the k_{T} and anti-k_{T} in the simulation. As jet clustering in the anti-k_{T} algorithm is insensitive soft (low momentum) particles, the jet area tends to be circular than the k_{T}.

In the clusterization, $p_{\mathrm{T}}^{\mathrm{jet}}$ is calculated as a scalar sum of transverse momenta of tracks belonging to the jet.

$$p_{\mathrm{T}^{\mathrm{jet}}} = \Sigma p_{\mathrm{T}}^{\mathrm{track}} \tag{3.7}$$

This is called p_{T} recombination scheme, and this scheme is chosen for the present analysis. This $p_{\mathrm{T}}^{\mathrm{jet}}$ can include particles coming from the background, which are not related to jets. Therefore, a background subtraction for $p_{\mathrm{T}}^{\mathrm{jet}}$ is needed.

3.5.4.1 Jet background subtraction

Since tracks are clustered into jets based on the sequential recombination method, irrelevant tracks can be also clustered. This background should be subtracted in $p_{\mathrm{T}}^{\mathrm{jet}}$. As the k_{T} algorithm is based on the sequential recombination, but is more sensitive to soft particles, it can be used to estimate the background density in jets. The background density (ρ) can be calculated event-by-event:

$$\rho = \underset{i \in I}{\mathrm{median}} \left\{ \frac{p_{\mathrm{T,i}}^{\mathrm{jet}}}{A_i^{\mathrm{jet}}} \right\} \tag{3.8}$$

where A^{jet} means the area of each jet. The highest and the second-highest momentum jets are excluded in the calculation, because those are likely to be real jets, not the background. With the obtained background density, the background subtraction for jets is done with:

$$p_{\mathrm{T,corr}}^{\mathrm{jet}} = p_{\mathrm{T}}^{\mathrm{jet}} - \rho \cdot A^{\mathrm{jet}} \tag{3.9}$$

where $p_{\mathrm{T}}^{\mathrm{jet}}$ and A^{jet} are obtained from the anti-k_{T} algorithm. The A^{jet} in the anti-k_{T} is calculated with πR^2. This corrected transverse momentum of jets ($p_{\mathrm{T,corr}}^{\mathrm{jet}}$) is used in the present analysis.

4 Analysis

As described in Ch. 2, this research concerns the interaction between jets and the QGP medium, in particular one of the anticipated mechanisms, the Mach shock wave. Since such an interaction signal has an angular relation with the jet axis, an angular correlations analysis helps to search for and study the features of the interaction. In the present analysis, jet-hadron and jet-proton correlations have been employed. This chapter explains the selections and cuts for events, tracks, and jets, and the datasets used in the analysis.

4.1 Dataset

We analyzed Pb–Pb collisions at a center of mass energy of $\sqrt{s_{\mathrm{NN}}} = 5.02$ TeV, collected in 2015 in ALICE at the LHC. The measured raw data in the collisions are processed and reconstructed for analysis by the ALICE DPG and provided with a certain nametag to distinguish them, e.g., pass1, pass2_lowIR. The higher number after the *pass* corresponds to the latest reconstructed dataset, which has improvements from the previous reconstructions, like detector calibration, fixes of specific signal issues, etc. In the present analysis, LHC15o.pass1 and LHC15o.pass5_lowIR were used. The *lowIR* indicates one of the sub-groups divided according to different interaction rates (IR) of the collisions. The interaction rate indicates the number of collisions that happen per second.

Different IR affects the performance of detectors in the measurement, and can impact the analysis results. Different IR data were analyzed and corrected for detector efficiency separately to prevent/minimize the IR effect in the results. After independent analysis and corrections, the final outputs were merged into a single result to get higher statistics. Table 4.1 shows the used divisions in the analysis. Note that the analyzed events in the table correspond to the number of events used in the present analysis, after event selections, like centrality, are applied, as described in the following sections.

Monte Carlo (MC) simulations were employed to study detector efficiency. Specific datasets that we used are LHC16g1 for pass1 and LHC17c5 for pass5_lowIR. Both are general-purpose *HIJING* (Heavy Ion Jet INteraction Generator) simulations anchored to LHC15o. HIJING [148] is a QCD-inspired MC model of jet production with the Lund model [149] for jet fragmentation and hard/semi-hard parton scattering with transverse momenta of a few GeV/c, which is expected to dominate high energy heavy-ion collisions. It has been developed and employed to treat mini-jets in pp, p–A and A–A collisions at high energies experiments. The simulated events by HIJING are propagating through a GEANT3 model [150] of the ALICE detector. (GEANT is a platform to simulate the passage of particles through matter, using the MC method. The GEANT3 model of the ALICE detector contains accurate and specific information about the detectors, like geometry, materials, and so on.) And then, all events and tracks are reconstructed from the GEANT simulation in the same way as real data. A comparison of generated events/tracks and reconstructed events/tracks is possible in simulations. Therefore, with that information, we obtain detector efficiency corresponding to the experimental conditions. The same division according to IR is used in MC as well, but note that the run number '246148' in the sub4 is missing in the MC.

There are two types of data formats widely used in ALICE: Event Summary Data (ESD) and Analysis Object Data (AOD). The ESD is the first reconstructed output from raw data and thus includes much more raw information on detectors and triggers. On the other hand, since AODs are the output of post-processing the ESDs, they have essential and compact information of analysis observables. In order to reduce the consumption of CPU and needed storage space, the AOD format is recommended for analyzers to use without a particular reason to use ESD. We analyzed data with AOD files, and the up-to-date filtered AODs were used in the data (AOD198) and MC (AOD194).

4.2 Event selection

4.2.1 Event cuts

An event in high-energy particle and nuclear physics means a collision of accelerated particles approaching from opposite directions or a collision between an accelerated particle and a fixed target. During the experiments, millions of events are generated, so it is important to distinguish good events worthy to be analyzed.

To figure out whether one event is good or not, a trigger system can be used as an assessment tool. When a collision occurs, some detectors send a signal to the ALICE Central Trigger Processor (CTP). Based on such input signals, the CTP assesses and decides which detectors start to do a read-out process to record detector information from the event. By using the trigger system, one can distinguish a real event from a fake event from the experimental background, e.g. beam and gas collision, and adjust the operation of detectors having different dead times (no detection during the read-out process) efficiently and optimally.

A trigger class is a set of requirements of fired inputs and there are many trigger classes based on detector properties and targeting different physics. Minimum bias

	Interaction Rate	Run numbers	Number of runs	Number of analyzed events
sub1	pass5_lowIR, IR <2 kHz	244918, 244975, 244980, 244982, 244983, 245064, 245066, 245068, 246391, 246392	10	0.25 M
sub2	pass1, 2 <IR <4 kHz	245702, 245705, 245831, 245833, 245949, 245952, 245954, 246003, 246012, 246053, 246089, 246276, 246763, 246765, 246766, 246810, 246989, 246991, 246994	19	1.23 M
sub3	pass1, 4 <IR <5.5 kHz	245692, 245700, 245829, 246001, 246049, 246052, 246153, 246182, 246185, 246222, 246225, 246275, 246493, 246495, 246759, 246760, 246808, 246809	18	1.18 M
sub4	pass1, IR >5 kHz	245683, 245923, 246036, 246037, 246042, 246048, 246087, 246113, 246115, 246148, 246151, 246152, 246178, 246180, 246181, 246217, 246271, 246272, 246424, 246428, 246431, 246434, 246487, 246488, 246750, 246751, 246757, 246758, 246804, 246805, 246807, 246844, 246845, 246846, 246847, 246851, 246928, 246945, 246948, 246980, 246982, 246984	42	2.45 M

Table 4.1: Sub groups and run numbers in different IRs.

(MB) is one of the trigger classes commonly used in ALICE and requires a signal from V0-A and V0-C. (Note that the definition of MB is changed in different run periods. This definition is valid for LHC15o.) As very forward and backward detectors, the simultaneous signal in V0-A and C guarantees a particle collision (event) is produced in the experiment. Since the MB trigger requires minimum input signals to the trigger in the collision, it allows us to accumulate event statistics with minimal bias and also to be mixed various types of events produced in the experiment, e.g. from high multiplicity events to diffractive collision events. In the present analysis, the MB trigger (called 'kINT7') was used, and more precise selections for events are explained as following.

After the trigger selection, there are remaining events to be rejected in the analysis. For rejection, the class '`AliEventCuts`' was employed, which includes a list of parameters of event cuts generally used in the collaboration. The best cuts are optimized depending on the period of the dataset; one can impose the cuts corresponding to the targeted data period and modify them independently for additional needs. This analysis used the default event cuts for the 2015 PbPb collision data called with the function '`AliEventCuts::SetupLHC15o()`' and imposed additional correlation-based event cuts for stronger pileup rejection. The pileup events and rejection are discussed in Sec. 4.2.3. The applied cuts with the AliEventCuts are listed in Table 4.2.

The default cuts for 2015 PbPb data contains various cuts to discriminate good events based on the magnetic field configuration, precise vertex parameters, correlation cut, and so on. In the default cut, at least one contributor (or candidate) of the primary vertex is required from the SPD or from global tracks. The z_{vertex} is the position of the primary vertex along the the beam (z) axis, and it should be within ± 10 cm. The absolute distance on z between the primary vertexes from the SPD and from global tracks is required to be less than 0.2 mm. Parameters with Nsigma (fMaxDeltaSpdTrackNsigmaSPD, fMaxDeltaSpdTrackNsigmaTrack) are calculated as a ratio of the absolute distance on z between the vertexes and the covariance matrix (σ) of the vertexes. Both values should be less than 10 and 20 for the SPD vertex and the global track vertex, where σ is a spatial resolution. Then, the maximum SPD resolution should be less than 2.5mm. The default trigger setup for LHC15o is the MB trigger, kINT7 and incomplete DAQ (Data AcQuisition) events are rejected. The sign of the magnetic field does not affect to the event selection. 'Pileup' is multiple nuclear collisions (in pp or Pb–Pb) that occur within the readout time resolution of the detectors in the experiment. Since a event refers to a single collision in the analysis, those pileup events should be rejected. In the case of high or low multiplicity events, the required cut for pileup is changed with fSPDpileupMinContributors: in higher multiplicity events, 5 contributors are allowed in the SPD vertexes, while in lower multiplicity events, only

Default cuts in `SetupLHC15o()`	
Parameter name	**Setup value**
fRequireTrackVertex	true
fMinVtz, fMaxVtz	-10, +10 cm
fMaxDeltaSpdTrackAbsolute	0.2
fMaxDeltaSpdTrackNsigmaSPD	10
fMaxDeltaSpdTrackNsigmaTrack	20
fMaxResolutionSPDvertex	0.25
fTriggerMask	AliVEvent::kINT7
fRejectDAQincomplete	true
fRequiredSolenoidPolarity	false
fUseMultiplicityDependentPileUpCuts	true
fSPDpileupMinContributors	3
fSPDpileupMinZdist	0.8 cm
fSPDpileupNsigmaZdist	3.0
fSPDpileupNsigmaDiamXY	2.0
fSPDpileupNsigmaDiamZ	5.0
fTrackletBGcut	false
Additional correlation cuts for pileup events	
fUseVariablesCorrelationCuts	true
fUseStrongVarCorrelationCut	true

Table 4.2: Applied event cuts in the class AliEventCuts.

3 contributors are accepted. If the distance on z between the SPD vertexes is less than 0.8, this event is likely to be pileup, so it should be rejected. And the resolution is calculated with the covariance matrix with the SPD vertexes and applied the cuts on z and $x-y$. In this analysis, additional cuts were used for pileup events: the correlation cut between event variables (fUseVariablesCorrelationCuts) and the correlation cut based on the multiplicities in the TPC and V0 (fUseStrongVarCorrelationCut). Multiplicity correlation method to reject pileup events is discussed in Sec. 4.2.3. All default cuts for LHC15o were employed, and Fig. 4.1 shows event statistics after the selection upon each event cut. The powerful cuts after the trigger selection are vertex position cuts for the SPD and track vertexes, multiplicity selection (centrality between 0 to 90 %), and correlation-related cut.

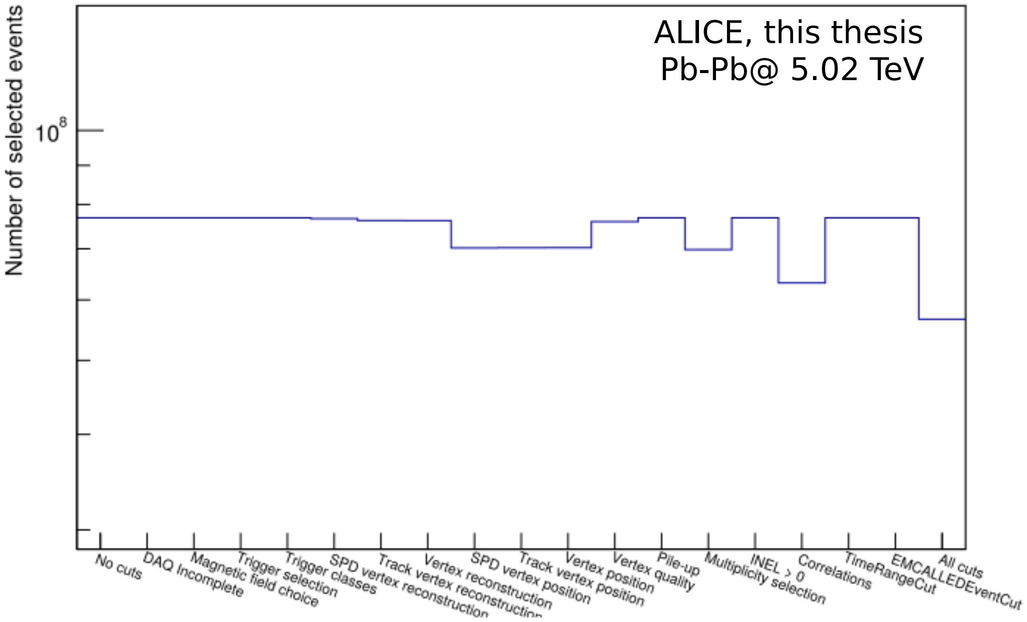

Figure 4.1: Event statistics after trigger selection('kINT7') from Pb–Pb collisions at $\sqrt{s_{\mathrm{NN}}} = 5.02$ TeV. Each bin shows the number of events that passed the labeled event cut in the AliEventCuts class. In the last column, the "all cuts" bin indicates the finally selected events through the AliEventCuts.

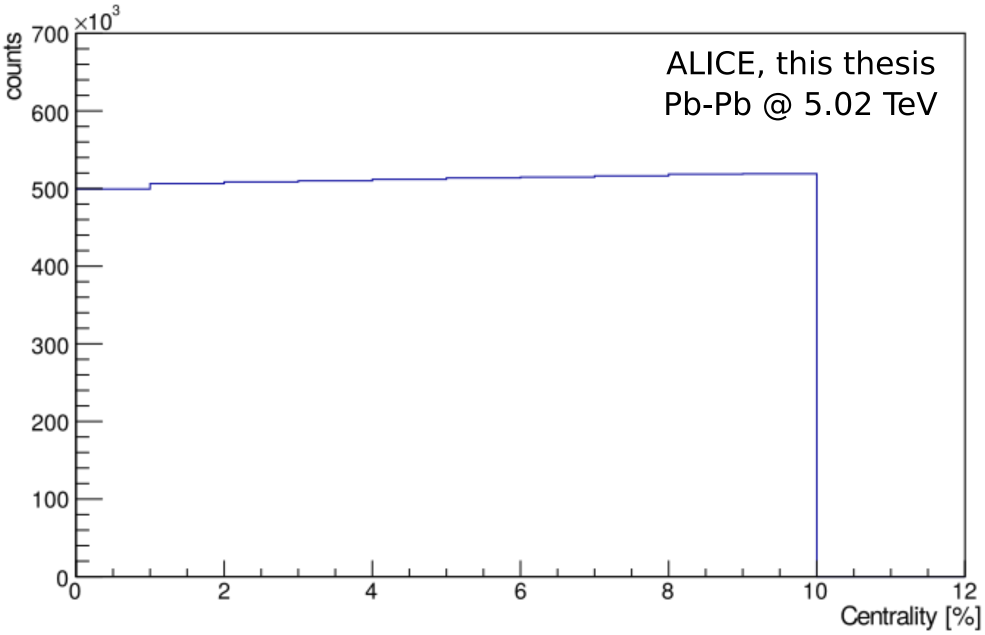

Figure 4.2: Centrality distribution of central events (0-10%) from Pb–Pb collisions at $\sqrt{s_{\mathrm{NN}}} = 5.02$ TeV. The events have passed all applied cuts from AliEventCuts and the manual pileup cut (described in Sec. 4.2.3). This figure shows a merged result from different IR datasets.

4.2.2 Centrality and Z-vertex

Figure 4.2 shows the centrality distribution of the selected events. It is mainly flat, but a minor increase exists as it goes to the more peripheral region. The additional pileup rejection (described in Sec. 4.2.3) induces a minor effect in the centrality distribution. The pileup cut introduced a decrease going towards more central events since pileup produces events with high multiplicity. The decrease is negligible, and the introduced pileup cut eliminated significant remaining pileup events. Pileup events can affect the correlation results because they makes unphysical correlations but are not corrected via standard corrections, like the acceptance correction and the event-mixing correction. Thus, the analysis proceeded with the current centrality distribution.

Since the ALICE central barrel detectors have limited acceptance in pseudorapidity, the z-position of the primary vertex can impact the detector performance and its acceptance. A particular z_{vertex} cut (commonly less than ± 10cm) is applied to guarantee uniform detector acceptance in the experiment. A ± 8cm cut was used in the present analysis to avoid detector efficiency drop at the edges of

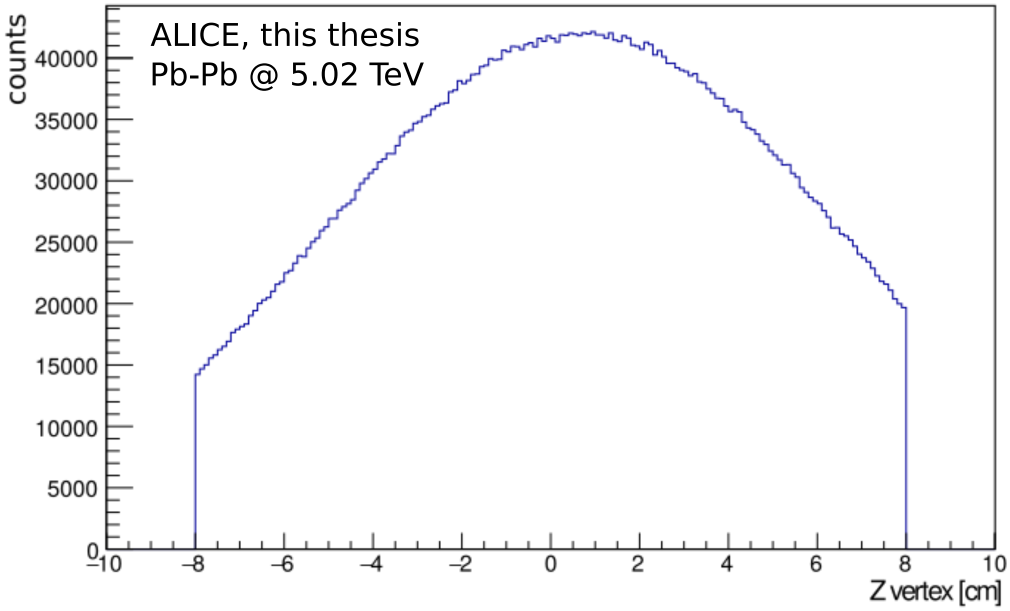

Figure 4.3: z_{vertex} distribution from Pb–Pb collisions at $\sqrt{s_{\mathrm{NN}}} = 5.02$ TeV, with 0-10% events. The events have passed all applied cuts including the AliEventCuts and the manual pileup cut (described in Sec. 4.2.3). This figure shows a merged result from different IR datasets.

the detector.

Figure 4.3 shows the z_{vertex} distribution in the selected events. It has a wide Gaussian distribution in the given range. However, the mean of the distribution is slightly shifted to the positive side. This effect comes from the beam-beam crossing. The proton and lead beams in the accelerator are tilted and bent with a strong magnet. Both beams are tilted and adjusted to get a crossing point at the center. Due to this alignment process, the z_{vertex} distribution can show a minor shift of the mean. Nevertheless, the overall distribution seems well-aligned at the center.

4.2.3 Pileup rejection

In the analysis, a single event means a single collision between two accelerated nuclei in the beam. Analyzers design physical observables and proceed to data analysis based on a single event. Then later, we accumulate multiple events for statistics. Therefore, if the pileup happens in the experiment, one should avoid recording and using these events as a single event in the analysis.

Thanks to the brilliant performance of the ALICE tracking detectors, we obtain

	Event reduction
IR < 2 kHz	0.3%
2 < IR < 4 kHz	7.9%
4 < IR < 5.5 kHz	11.6%
IR > 5.5 kHz	17.2%

Table 4.3: Event reduction after pileup cut.

reconstructed tracks and find primary vertices under pileup conditions. An actual nuclear collision has to come from one primary vertex, so thus numerous tracks from different collisions can be grouped in each event and distinguished. Among those events, we choose the best primary vertex and tracks belonging to it. The others are rejected in the analysis. Such a selection process has been done by the DPG and the applied event cuts.

After the process, however, some remaining pileup contributions can exist in the recorded data since the reconstructed tracks can be mismatched to a primary vertex. To remove the remaining pileup, we use a multiplicity-based pileup cut in this analysis. As mentioned above, the pileup signal in the detectors depends on each detector's readout time. The TPC has a much longer readout time, 100 μs, than other detectors in ALICE. The V0 has 25 ns readout time in each section, overall 2.5 μs, much shorter than the TPC. If one compares multiplicity measurements between TPC and V0, it shows the effect from different readout times.

Figure 4.4 shows multiplicity measured in the TPC outer barrel with OROC (TPCoutMult) vs. multiplicity measured in V0 (V0 multiplicity). As one can see in Fig. 4.4, the distribution is diagonal for most events. However, notable outliers have much higher multiplicity in the TPC than in the V0, coming from the pileup events. Due to the slow readout of TPC, it is more vulnerable to pileup.

Although pileup rejection has been done with AliEventCuts, it turned out that there are substantial pileup events between TPC and V0 multiplicity in Fig. 4.4. As such events should be rejected, a linear cut in the correlation (shown as the dashed line in Fig. 4.4) was applied. The linear cut is acquired with this relation:

$$\text{TPCoutMult} - 0.285 * \text{V0 multiplicity} < 1040 \tag{4.1}$$

Table 4.3 shows event reductions after the linear cut in each IR dataset. The reduction is much more significant in higher IR datasets, which agrees with our expectation that higher IR runs have more pileup events.

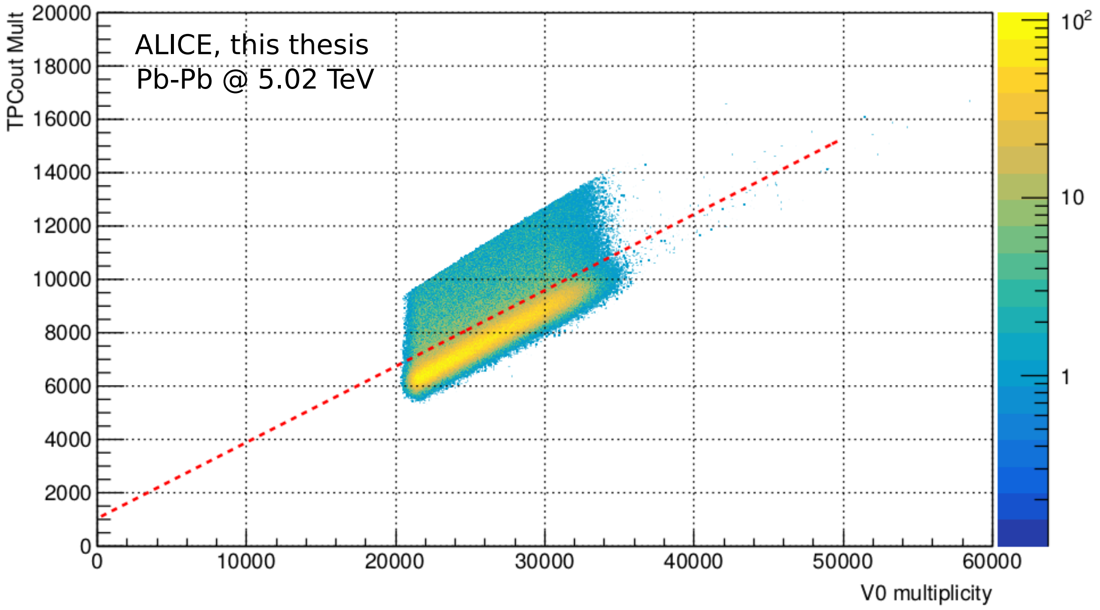

Figure 4.4: Multiplicity distribution from TPC-out and VZERO detector with accepted events after AliEventCuts, z_{vertex} cut (± 8cm), and centrality cut (0-10%). The red dashed line is our linear cut to remove remaining pileup events. This plot is from the highest IR dataset (IR > 5.5 kHz).

4.3 Track selection

This section focus on used track selection and tracking efficiency in selected tracks for the present analysis. Information about the general tracking procedure in ALICE can be found in Sec. 3.5.2

4.3.1 Hybrid track

Among the reconstructed tracks, we applied a few track cuts to select appropriate ones for this analysis. Since general quality assurance cuts are used commonly in many analyses and tuned threshold values are obtained through dedicated detector studies, Aliroot (described in Ch. 3) stores relevant information on the cuts and lets the user call the accepted tracks through the cuts with a track bit depending on their analysis purposes.

We used *'hybrid tracks'* in this analysis, corresponding to AOD track bit 768 (sum of two different track bits, 256+512). Hybrid tracks were defined first in the 2010 Pb–Pb dataset (LHC10h) to compensate for a hole in the azimuthal distribution caused by the partial missing channels of the SPD. Filter bit 768 consists of two groups of tracks; one is called global hybrid tracks (track bit 256), and the other is complementary hybrid tracks (track bit 512).

Global tracks are required to pass standard ITS+TPC cuts and have SPD hit required and golden χ^2 cut. The global tracks are good reconstructed tracks in the ITS and the TPC but are missing in some areas because of dead channels in the SPD. Complementary tracks are exploited to make up for the constraint in the global tracks. They pass through the standard ITS+TPC cuts but have no requirement of a hit in the SPD.

Figure 4.5 is φ_{track} distribution from global (red), complementary (blue) and sum of both tracks (black) from one run (246329). Using the hybrid tracks provides a flat track distribution in φ and allows for a uniform jet distribution in φ later. Table 4.4 has information about the detailed parameters of hybrid track cuts. Such parameters can be defined and adjusted by using the listed functions in the code but also the whole list of the cuts is easily called and applied with the function '`SetAODFilterBits(768)`' to the list of tracks (track container).

In this analysis, we employed the default values for the track cuts. A minimum number of crossed rows in the TPC is required above 70, close to half of the total pad rows, 159. The fraction of crossed rows over findable clusters (possible crossed pad rows when predicting a tracked trajectory over the TPC) in the TPC is used as a cut parameter, above 80%. The χ^2 cuts (SetMaxChi2PerClusterTPC, SetMaxChi2PerClusterITS, SetMaxChi2TPCConstrainedGlobal) are related to the general tracking procedure with the Kalman filter. During the tracking process, a fit result is obtained between an expected track line and measured clusters. The

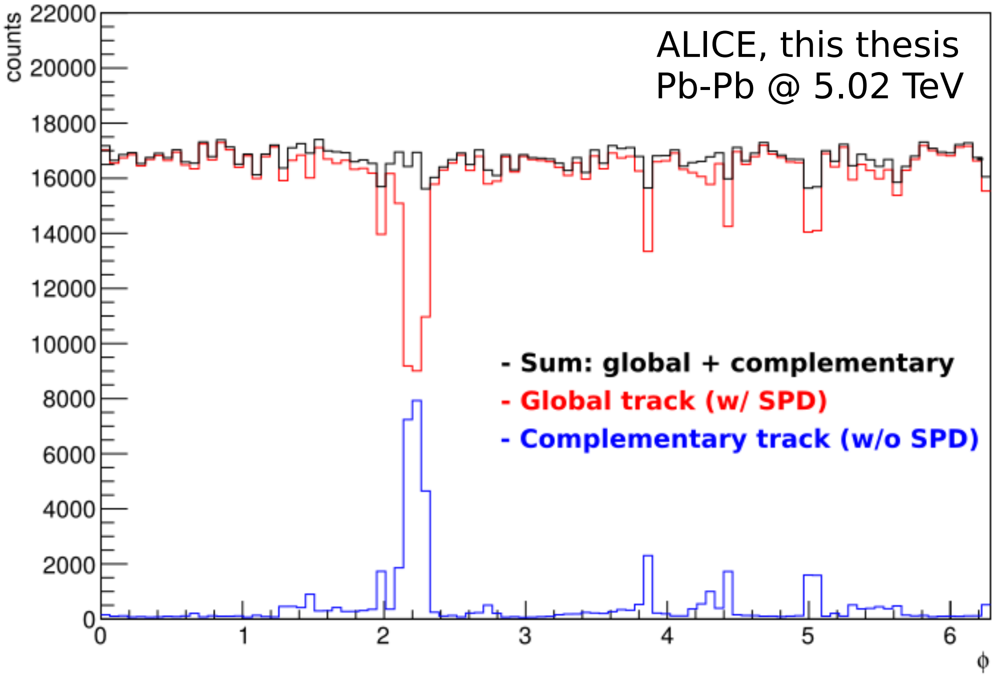

Figure 4.5: φ distribution of charged tracks in one run (246392). Red is from global tracks with required SPD hit, and blue is from complementary tracks with no requirement of SPD. Black (hybrid tracks) shows the sum of both types of tracks.

discrepancy between the track line and the clusters can be expressed as χ^2. Both TPC and ITS refit are required: After obtaining an expected track line from iterated Kalman filter processes, a refit is performed including all clusters in the ITS and the TPC. As explained earlier, the SPD clusters are required for global tracks but not for complementary tracks. The golden χ^2 cut (corresponding to SetMaxChi2TPCConstrainedGlobal) calculates χ^2 between a TPC constrained track (only tracking within the TPC clusters) and a global track to the primary vertex. Its deviation between two tracks should not be above 36. This golden cut is helpful to remove secondary tracks. DCA (Distance of Closest approach to the primary vertex) cuts are also employed for track selection, 2.4 cm and 3.2 cm in the $x - y$ and the z-direction. The number of shared TPC clusters to the total clusters is also used as a cut parameter.

Applied cuts for hybrid tracks (AOD track-bit: 768 = 256 + 512)	
Used function name	**Value**
SetMinNCrossedRowsTPC	70
SetMinRatioCrossedRowsOverFindableClustersTPC	0.8
SetMaxChi2PerClusterTPC	4
SetAcceptKinkDaughters	kFALSE
SetRequireTPCRefit	kTRUE
SetRequireITSRefit	kTRUE
SetClusterRequirementITS	kSPD, kAny
SetRequireSigmaToVertex	kFALSE
SetMaxChi2PerClusterITS	36
SetMaxChi2TPCConstrainedGlobal	36
SetMaxDCAToVertexXY	2.4 cm
SetMaxDCAToVertexZ	3.2 cm
SetDCAToVertex2D	kTRUE
SetMaxFractionSharedTPCClusters	0.4
additionally valid for only bit 512	
SetClusterRequirementITS	kSPD, kOff

Table 4.4: Applied track cuts for hybrid tracks.

4.3.2 Single track reconstruction efficiency

As described earlier, since tracks are measured and reconstructed based on the information from detectors, they are affected by the efficiency of detectors. To study and correct the detector effect on tracks, we utilize Monte-Carlo simulation (MC) results.

In the MC, we obtain generated particles and reconstructed tracks. The generated particles are obtained relying on implemented theoretical physics principles in the MC. On the other hand, the reconstructed tracks are acquired based on predicted detector responses and track reconstruction in the simulation. Consequently, the generated particles represent physics results, and the reconstructed tracks correspond to measured results in the experiment. The specific information about the MC used in this analysis can be found in Sec. 4.1.

Detector effects cause a difference between the generated and the reconstructed tracks so that one can calculate single track efficiency as the ratio of the yield of reconstructed tracks to the yield of generated particles:

$$\varepsilon = \frac{yield\ of\ reconstructed\ tracks}{yield\ of\ generated\ tracks} \tag{4.2}$$

Except for the simulated detector performance, other conditions should be equal in both sets of tracks. For the generated particles, only charged and primary particles were used. For the reconstructed tracks, the same track selection (hybrid track cut) was used like the real data. The same track η cut ($|\eta| < 0.8$) and the p_{T} cut ($p_{\mathrm{T}} > 150$ MeV/c) was applied in both cases.

4.3.2.1 Unidentified hadron efficiency

The 3-D efficiency as a function of z_{vertex}, η_{track}, and $p_{\mathrm{T}}^{\mathrm{track}}$ was employed in this analysis. Figures 4.6, 4.7, and 4.8 show the inclusive hadron efficiency projected onto each parameter. This is the efficiency for inclusive hadrons so no particle identification information is required.

As the target p_{T} range is between 2 to 4 GeV/c in the present analysis, the efficiency projected on z_{vertex} and η_{track} contains only tracks in that p_{T} range. The efficiency is close to 0.77 (in the lowest IR, close to 0.79) and looks roughly flat with respect to z_{vertex} and η_{track}. Compared to z_{vertex}, the efficiency in η_{track} has a little structure in it. The decrease on both edges is because of the limited acceptance of the TPC. The drop on the center is due to the TPC central electrode, so the tracks crossing the electrode are not fully measurable.

The efficiency with $p_{\mathrm{T}}^{\mathrm{track}}$ has a curved shape related to the trajectory of flying particles and the TPC detector structure. Since higher-p_{T} particles bend much less inside the magnetic field and fly more straight, they are more likely to be lost

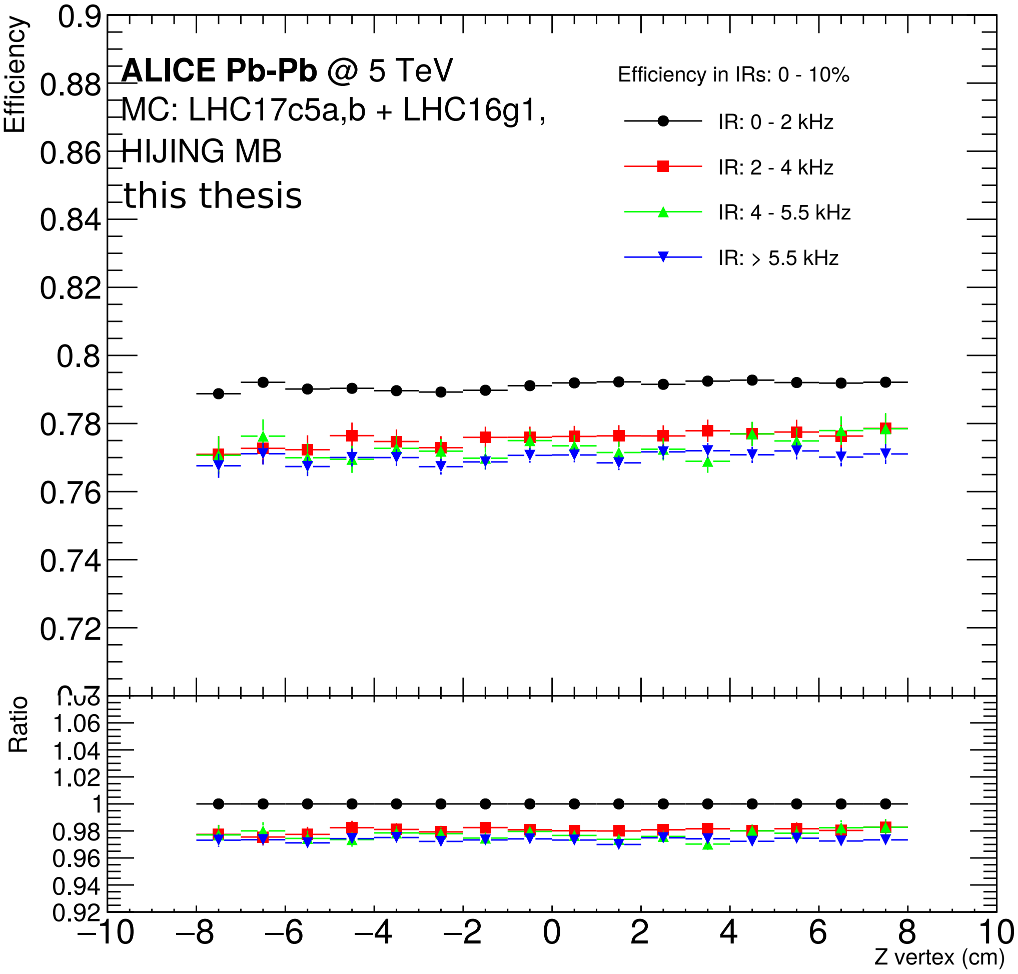

Figure 4.6: Single track reconstruction efficiency for hadrons projected on the z_{vertex}. The used MC simulation is from HIJING Minimum-Biased events (MB). LHC17c5a,b for IR in 0 to 2kHz and LHC16g1 for IR larger than 2kHz. The projected z_{vertex} efficiency is for particles with $p_{\mathrm{T}} = 2$ to 4 GeV$/c$ and the full range of η_{track} (± 0.8). The bottom panel shows the efficiency ratio relative to the lowest IR result (0-2kHz).

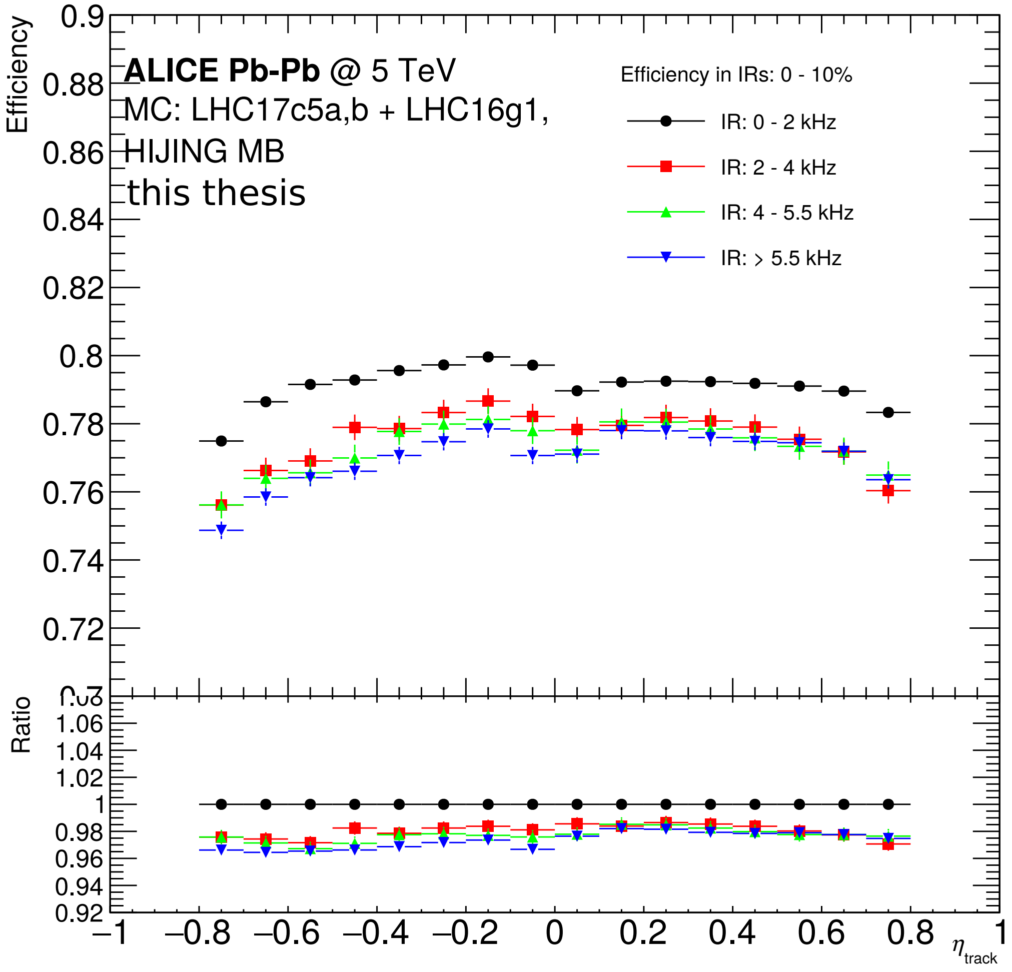

Figure 4.7: Single track reconstruction efficiency for hadrons projected on the η_{track}. The used MC simulation is from HIJING Minimum-Biased events (MB). LHC17c5a,b for IR in 0 to 2kHz and LHC16g1 for IR larger than 2kHz. The projected η_{track} efficiency is for particles with p_{T} $= 2$ to 4 GeV$/c$ and the full range of z_{vertex} (±8cm). The bottom panel shows the efficiency ratio relative to the lowest IR result (0-2kHz).

within the TPC sector boundaries, a non-measurable area. This contributes to a drop in the efficiency in the higher p_T regime.

Despite this, there is a minor increase above 3 GeV/c. It is related to the energy loss ($\mathrm{d}E/\mathrm{d}x$) measurement in the TPC. According to the Bethe-Bloch equation, describing the mean rate of energy loss, the mean energy loss rate decreases rapidly to the minimum ionization (for pions approximately below 1 GeV/c, and for protons around 3 GeV/c) and increases slightly again. The energy loss contributes to producing TPC clusters. For instance, if a particle loses only the minimum energy in the TPC, it can lead to small or negligible clusters. This can affect the general tracking performance due to insufficient reconstructed clusters. At higher p_T above 3-4 GeV/c, most particles are beyond the minimum ionization range, so the efficiency rises again due to the increasing mean energy loss.

We studied the hadron efficiency differentially depending on different IR groups for all the parameters. Although there is no pileup in the simulation, we looked into the IR-dependent efficiencies to estimate different detector responses in the changed collision conditions. As seen in Figs. 4.6, 4.7, and 4.8, the general efficiency trend looks similar in the different IRs. However, higher IR groups have a little lower efficiency in every parameter compared to the lowest IR. The bottom panel of the efficiency plots displays the ratio between the lowest IR and higher IR sets. The maximum deviation is about 3 - 4 % for all the parameters. We corrected our jet-hadron correlations with the obtained efficiencies to compensate for the detector effects in the measured results. The correction has been done separately in each IR group. About the contamination effect, for example, secondary hadrons from decays, is expected to be negligible in the targeted p_T ($2 < p_\mathrm{T} < 4$ GeV/c) range in this work.

4.4 Proton Identification

This section discusses the proton identification method, cut optimization, and tracking efficiency for selected protons in the present analysis. General information about particle identification detectors and methods in ALICE can be found in Sec. 3.5.3

4.4.1 PID cut optimization

Two types of associated particles were employed in the correlation function in the present analysis: unidentified hadrons and protons. For hadrons, we used inclusive charged hadrons in the given p_T range without PID selection. For proton identification, we utilized the TPC (n_σ^TPC) and TOF (m^2) information. Using a combination of the TPC and TOF information for PID is useful to supplement

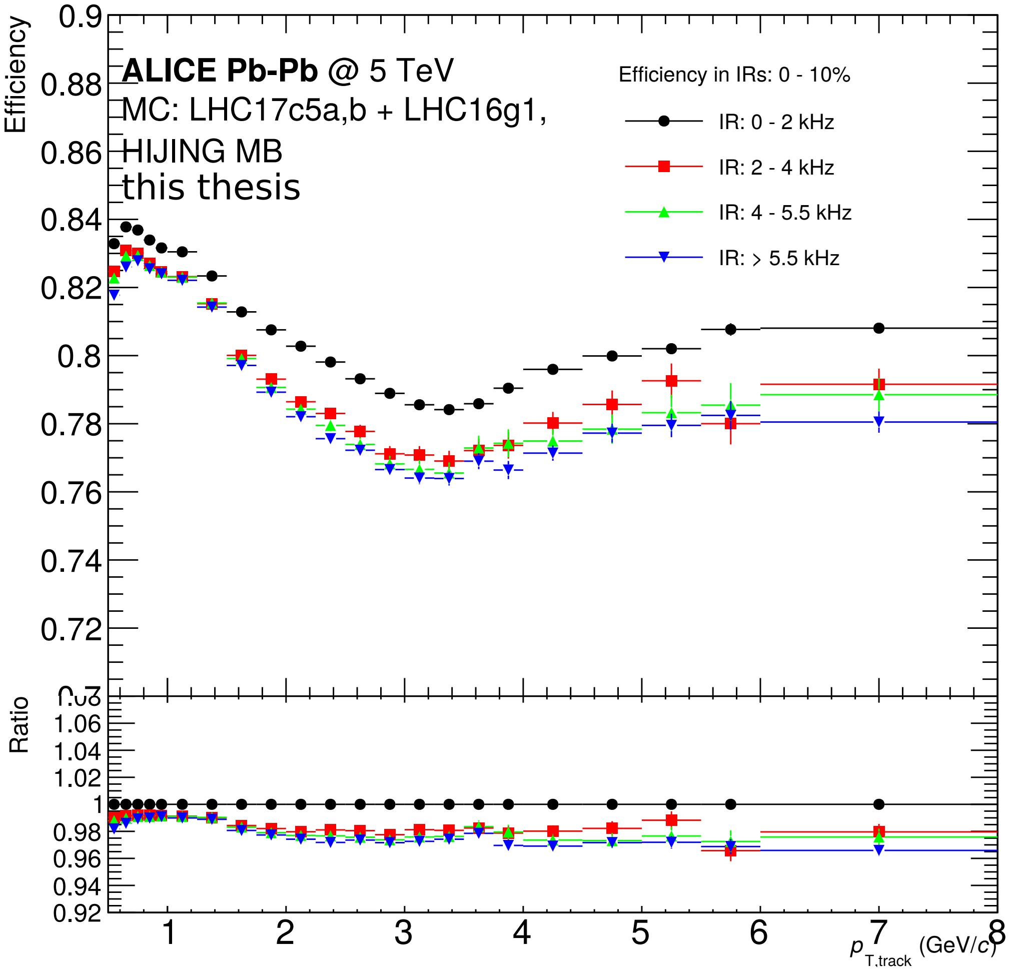

Figure 4.8: Single track reconstruction efficiency for hadrons projected on the $p_{\mathrm{T}}^{\mathrm{track}}$. The used MC simulation is from HIJING Minimum-Biased events (MB). LHC17c5a,b for IR in 0 to 2kHz and LHC16g1 for IR larger than 2kHz. The projected $p_{\mathrm{T}}^{\mathrm{track}}$ efficiency is for particles with the full range of z_{vertex} and η_{track} (±8cm, ±0.8). The bottom panel shows the efficiency ratio relative to the lowest IR result (0-2kHz).

the constraints of each detector PID method, which is induced by the overlap with other particles. For example, the TPC Bethe-bloch spline for protons is overlapped with the splines for electrons and pions above 1 GeV/c. Due to the overlapping of the splines, when protons are selected based on $n_{\sigma}^{\mathrm{TPC}}$ with respect to the proton spline, the proton samples are contaminated by pions and electrons. However, at this p_{T} region, the TOF β signal shows a clear separation between protons and other particles. Thus, the TOF signal can supplement the TPC signal to identify protons from other particles. Note that $n_{\sigma}^{\mathrm{TPC}}$ refers to the $n_{\sigma,\mathrm{proton}}^{\mathrm{TPC}}$, and $n_{\sigma}^{\mathrm{TOF}}$ refers to the $n_{\sigma,\mathrm{proton}}^{\mathrm{TOF}}$ below, since the PID was performed for only protons. And also σ^{TPC} and σ^{TOF} mean the $\sigma_{\mathrm{proton}}^{\mathrm{TPC}}$ and the $\sigma_{\mathrm{proton}}^{\mathrm{TOF}}$, respectively.

In the case of TPC PID, a general $2\sigma^{\mathrm{TPC}}$ cut was applied initially. While proceeding with our research, we found that the TPC PID signals were not optimally calibrated in the different IR datasets, so we optimized the σ^{TPC} cut value in each IR set as described below. Figure 4.9 shows the comparison of the $n_{\sigma}^{\mathrm{TPC}}$ distribution between different IR sets in the data.

As seen in Fig. 4.9, the lowest IR shows a much wider peak than the other IR sets. However, such s larger width is not seen in the comparison between data and MC with the lowest IR in Fig. 4.10. From the data and the MC comparison, we figured out that the wider width is presumably caused by the PID data process in the data only. To avoid this mismatch between data and MC and get the same proportion of yields corresponding to $2\sigma^{\mathrm{TPC}}$ (95% of statistics), we had to apply an optimized cut, which has the correct 2σ value for the data, from -2.88 to 2.88 in the lowest IR. This modified cut value, ± 2.88, was obtained from Gaussian fit on data to get the correct 2σ having 95% statistics.

In the higher IR sets, we found a different mismatch between data and MC in the $n_{\sigma}^{\mathrm{TPC}}$. As shown in Fig. 4.9, the higher IR curves have shifted means to the negative side around -0.2. However, such mean-shifting was not shown in the comparison between data and MC for the higher IR datasets in Fig. 4.11. Figure 4.11 displays one example comparison between the data and the MC with the highest IR set ($>$ 5.5kHz), but we confirmed the same behavior in all other IR sets (2-4, 4-5.5 kHz). The $2\sigma^{\mathrm{TPC}}$ cut was moved according to the shift, from -2.2 to $+1.8$, in the higher IRs.

For TOF PID, we use the m^2 value instead of $n_{\sigma}^{\mathrm{TOF}}$. A significant benefit in using m^2 is that the mean value of each particle in the m^2 distribution is predicted theoretically. It allows us to clearly distinguish the distribution of proton signals from other particles.

Clean separation of protons and other particles is also crucial to estimate more accurate efficiency and purity in the given datasets. The following section addresses our study to determine a m^2 cut value for protons and the expected efficiency and purity resulting from the given cut.

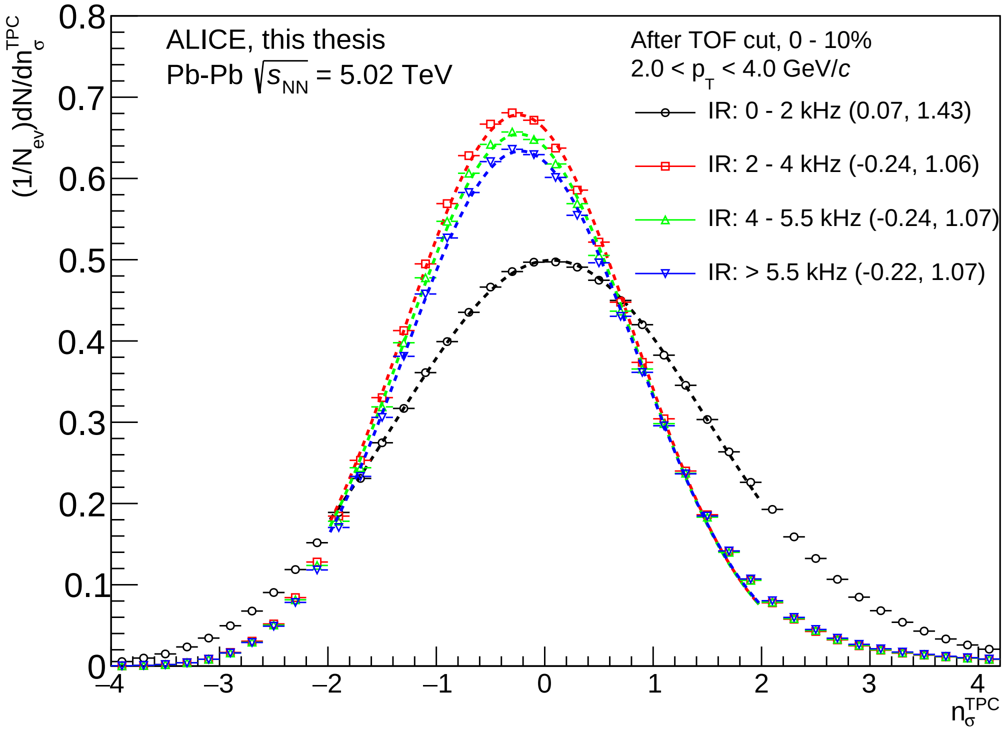

Figure 4.9: $n_\sigma^{\rm TPC}$ distribution after TOF cut ($n_\sigma^{\rm TOF}$ <2) in different IRs. Only $p_{\rm T}$ = 2 - 4 GeV/c tracks are selected. In the legend, the two numbers in parentheses are the mean and the width from the Gaussian fits. All histograms are normalized with the number of events in each IR.

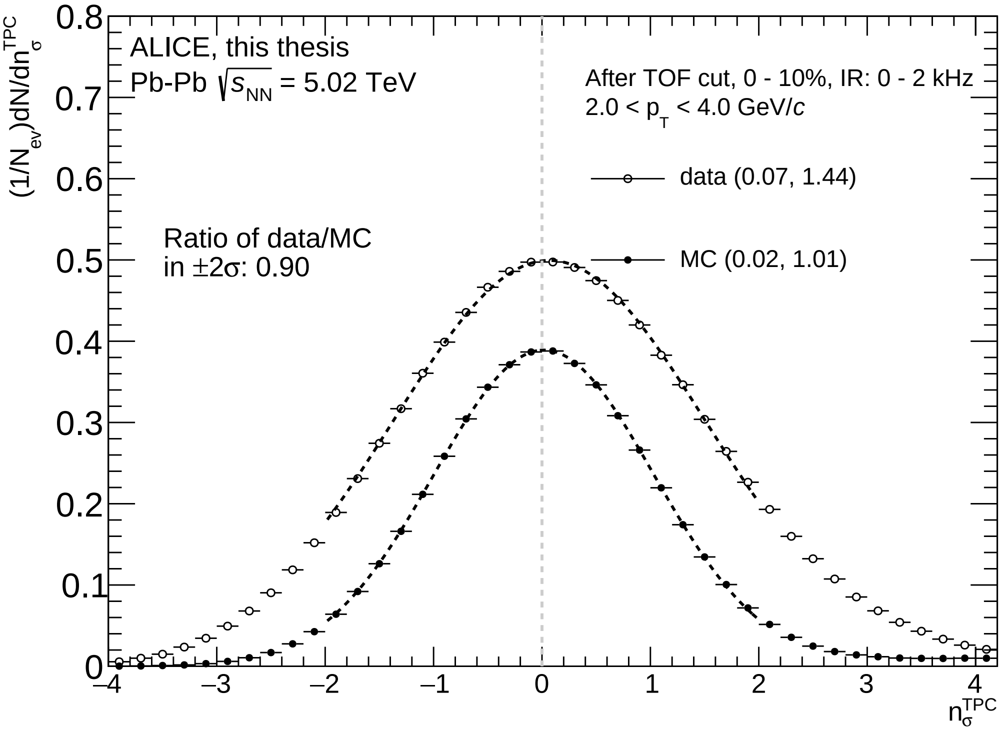

Figure 4.10: Comparison of the n_σ^{TPC} distributions after TOF cut with (n_σ^{TOF} <2) between MC and data in the lowest IR (0-2kHz). In the legend, the two numbers in parentheses are the mean and the width from the Gaussian fits. On the left side, the ratio is the integration ratio between data and MC in ±2.

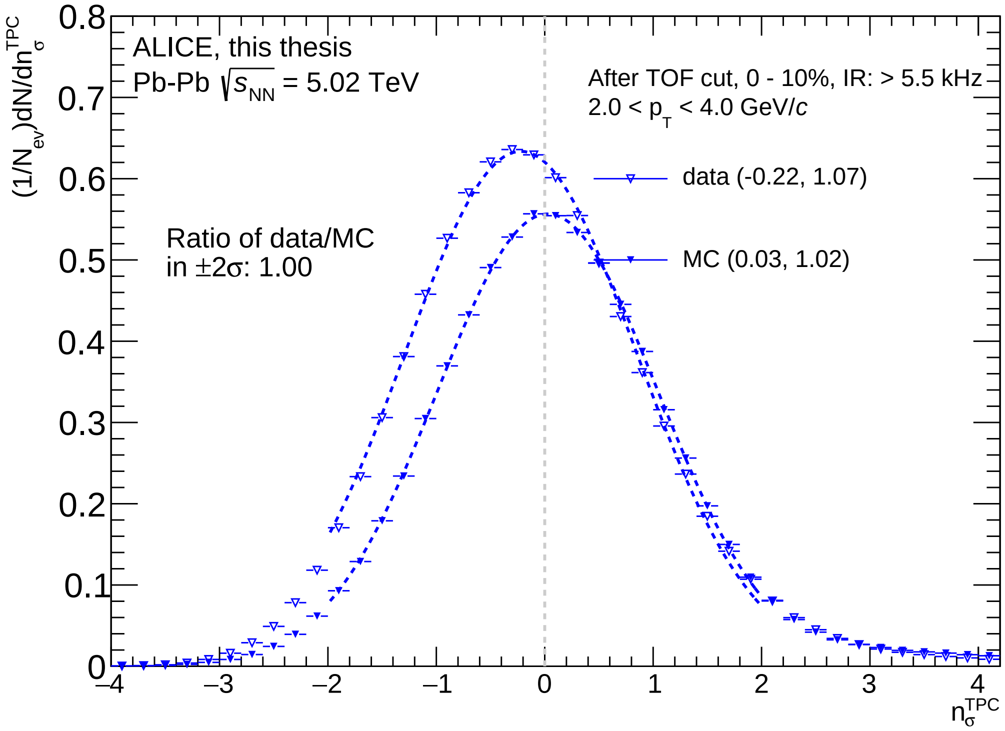

Figure 4.11: Comparison of the $n_{\sigma}^{\mathrm{TPC}}$ distributions after TOF cut with ($n_{\sigma}^{\mathrm{TOF}}$ <2) between MC and data in the highest IR (>5.5kHz). In the legend, the two numbers in parentheses are the mean and the width from the Gaussian fits. On the left side, the ratio is the integration ratio between data and MC in ±2.

4.4.2 Proton efficiency and purity for different mass cut

The template fit method was used to optimize the purity and efficiency of the proton PID. The template fit method is a way to use a fit to estimate particles' distribution using a template instead of an analytical function. This method is useful when it is difficult to obtain a fit function, but there is a good template for the fit.

The template fit was used in the present analysis because of the widths of particles' distribution. As mentioned above, m^2 is known from measurements. However, the width of each particle's distribution is unknown and is sensitive to detector performance. For instance, the momentum resolution of the TPC affects the width of the m^2 distribution, and the resolution depends on p_{T}. Therefore, MC results were exploited to acquire good templates for different particle species (pion, kaon, and proton). In MC, we can access reconstructed tracks having detector responses and generated particles together. Through a matching between reconstructed tracks and generated particles based on the Particle Data Group (PDG) code [38], we checked the identities of the used particles. Then, we obtained templates with identified reconstructed tracks, which include realistic widths from MC tuned on data.

With the obtained templates from MC, we fitted the m^2 distributions after a $2\sigma^{\mathrm{TPC}}$ cut was applied. There can be a deviation between the data distribution and the MC templates in the initial fit because sophisticated detector effects and limited detector resolutions are convoluted in the actual measurement. The χ^2/ndf value is calculated in every fit to reduce the deviation between the data and the templates. In the code, a single fit includes hundreds of repeating steps which minimize the deviation between the templates and the data with a minimizing process based on `GSLMinimizer` [151]. When we start to fit with more optimized templates from the last fit, it returns improved fit results and much lower χ^2/ndf in the end. If we repeat a fit with optimized templates, fit results are improved, and the fit quality is saturated at some point. Therefore, iterating the fit was required for optimization. Figure 4.12 shows the development of the fit template as repeating iterations. After more than 5 iterations, we obtained reliable fit results, and the χ^2/ndf is very close to 1.

We learned the expected distribution for pion, kaon, and proton in the data through the fit method. Thanks to that, the efficiency and purity of protons for the given m^2 cut value were estimated. Figure 4.13 shows the efficiency and purity as a function of m^2 cut value. The m^2 cut has lower and upper values, and the upper one is fixed at 2 GeV^2/c^4 because the proton distribution vanishes above that. Therefore, the cut value on the x-axis in Fig. 4.13 indicates the lower cut. The efficiency increases when the m^2 cut is loose because it covers the whole proton distribution. However, the purity becomes lower since the lower m^2 cut also contains many pions and kaons. Purity is an essential factor, but the lack of statistics is more vital in the present analysis. For that reason, we decided to use $0.3 < m^2 < 2$ GeV$^2/c^4$ to ensure high efficiency and good-enough purity for protons.

4.4.3 Single track reconstruction efficiency for proton

As calculated for the hadron single track efficiency, the proton single track efficiency is estimated using MC simulations:

$$\varepsilon = \frac{yield\ of\ reconstructed\ protons}{yield\ of\ generated\ protons} \times \frac{1}{1-\delta} \tag{4.3}$$

$$\delta = \frac{yield\ of\ fake\ protons\ among\ reconstructed\ protons}{yield\ of\ all\ reconstructed\ protons} \tag{4.4}$$

Equation 4.3 shows the formula for the efficiency of protons. Unlike the hadron efficiency, the efficiency of protons has an additional term, δ. Since the proton efficiency includes the PID process, the probability of fake protons in the reconstructed protons (δ) has to be considered.

Note that this single track reconstruction efficiency is different from the efficiency that we addressed in the template fit method. The efficiency in the template fit is related to the efficiency of particle identification performance depending on the PID cuts. This efficiency extracted from MC is related to the reconstruction process of ALICE tracking detectors for proton tracks. Although PID is used to confirm if the reconstructed track is a proton or not in the single track efficiency, the efficiency value addresses how many identified proton tracks are reconstructed of the total of the generated protons.

Like the hadron case, the 3-D efficiency as a function of z_{vertex}, η_{track}, and $p_{\mathrm{T}}^{\mathrm{track}}$ was calculated for protons. Figures 4.14, 4.15, and 4.16 show the efficiency projection results on each parameter. The efficiency in z_{vertex} and η_{track} contains only protons in our target $2 < p_{\mathrm{T}} < 4$ GeV$/c$ range.

The efficiency for protons is around 0.4, much lower than for the unidentified hadrons. This efficiency drop is because the single track reconstruction efficiency for protons is affected by the tracking performance as well as the PID performance in the TPC and TOF to be identified as protons. Both performances impacts to the efficiency for protons, so it shows a significant drop compared to the efficiency for unidentified hadrons.

Besides, the discontinuous efficiency is shown for protons in the η_{track}. This discontinuity is induced by the TOF, due to the non-instrumented part in the TOF for the PHOS calorimeter. (The non-instrumented area is $4.4 < \varphi < 5.4$ and $|\eta| < 0.2$.) The discontinuity in η_{track} was disappeared, when the efficiency was

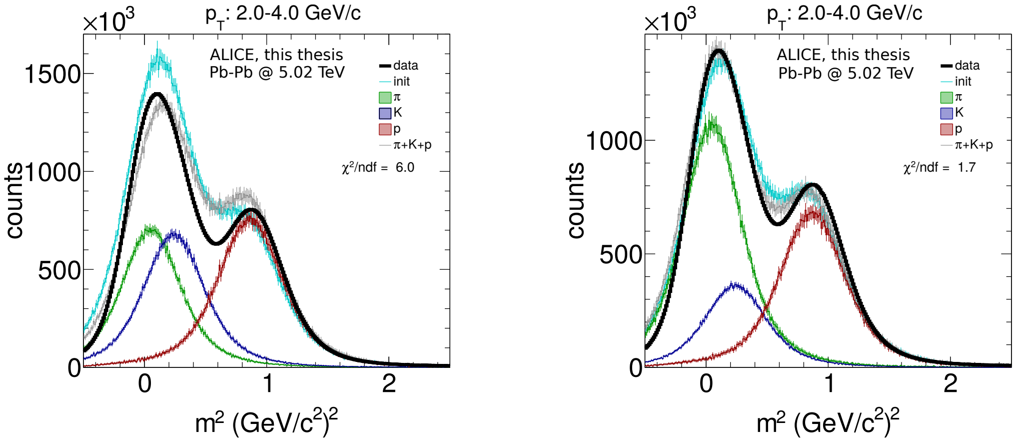

(a) Iteration 1

(b) Iteration 2

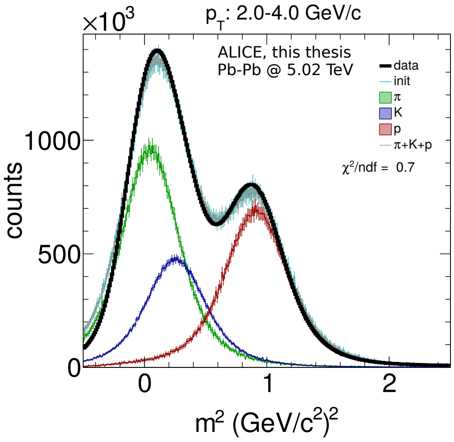

(c) Final iteration result

Figure 4.12: m^2 distribution for the template fit method. (a), (b), and (c) shows template fit results in the iterating process. Black is the m^2 distribution after a TPC cut ($|n_\sigma^{\mathrm{TPC}}| < 2$) was applied from data, and the colorful templates for pion, kaon, and proton are from MC. Cyan represents the initial fit function before χ^2/ndf optimization, and gray shows the final fit function.

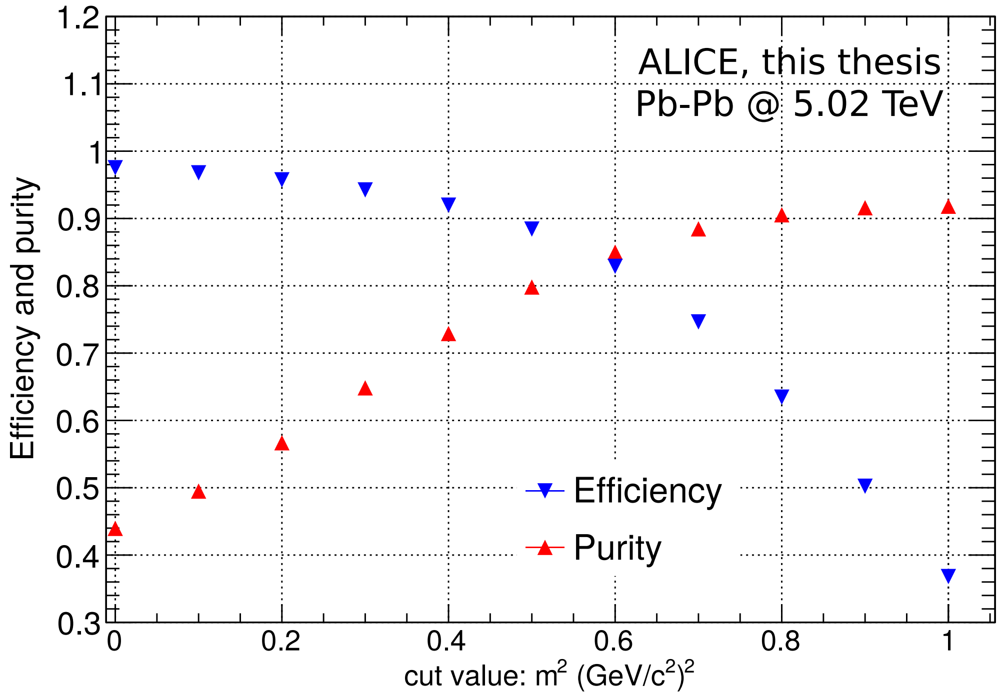

Figure 4.13: Efficiency and purity based on the template fit result in the given m^2 cut (the lower bound). The upper bound cut value is fixed at 2 GeV^2/c^4. Track p_{T} range is $2 < p_{\mathrm{T}} < 4$ GeV/c.

obtained with only the TPC information.

The efficiency in $p_{\mathrm{T}}^{\mathrm{track}}$ has a smooth drop above 3GeV/c. This efficiency involves general tracking and PID performance, significantly different from the hadron's efficiency trend. In our targeted p_{T} range ($2 < p_{\mathrm{T}} < 4$ GeV/c), all efficiencies from different IR sets are close to 0.4. The deviation between IR sets (shown in the bottom panel) is a maximum of 10 to 15%, somewhat larger than the deviation in the hadron efficiency. With the efficiency, we corrected the jet-proton correlation function. The correction has been done separately in each IR set.

4.5 Jet selection

This section explains how the jet selection is done for the present analysis. Information about the jet clusterization process can be found in Sec. 3.5.4.

4.5.1 Jet selection

As described in Sec. 3.5.4, the anti-k_{T} algorithm was used for jet clusterization. Charged jets were used to guarantee a uniform jet distribution in φ and η. Only charged tracks above 0.15 GeV/c were employed for the jet clusterization. A jet radius of $\mathrm{R} = 0.2$ was used in this work to reduce the background for the jets. A jet area cut was also applied: the clusterized jet area (spatial area sum of involved tracks) should be higher than 60% of the jet area ($\pi \mathrm{R}^2$). The jet η is within ± 0.6 (η-R), determined by the track η range ± 0.8. A leading constituent cut (the highest momentum track in a jet), $p_{\mathrm{T}}^{\mathrm{track}} > 5$ GeV/c, was used. After the jet background subtraction (see Sec. 3.5.4.1), a jet p_{T} cut, $p_{\mathrm{T,corr}}^{\mathrm{jet}} > 25$ GeV/c, was applied to reduce combinatorial jets, which are not true jets but can be produced by the jet clustering due to the background. These are the used jet criteria in this work. Further studies about the leading constituent cut and the jet p_{T} cut are explained as following.

Real jets from hard scattered partons are obtained after jet clustering, but combinatorial jets are also included. A leading constituent cut was employed to reduce combinatorial jets in our selections. The leading constituent means the track carrying the highest p_{T} inside of the jet. The leading constituents were required to be above 5 GeV/c. To test the effectiveness of the leading constituent cut, the particle spectra as a function of p_{T} and a Blast-Wave (BW) fit on each particle species was compared in Fig. 4.17.

The BW function [152] describes thermal production induced by the radial flow in the QGP medium, so it shows a good agreement with the spectra at low p_{T} and an increasing discrepancy at higher p_{T} above 1.5 GeV/c due to the particles not coming from the thermal production. Through this comparison, we calculated

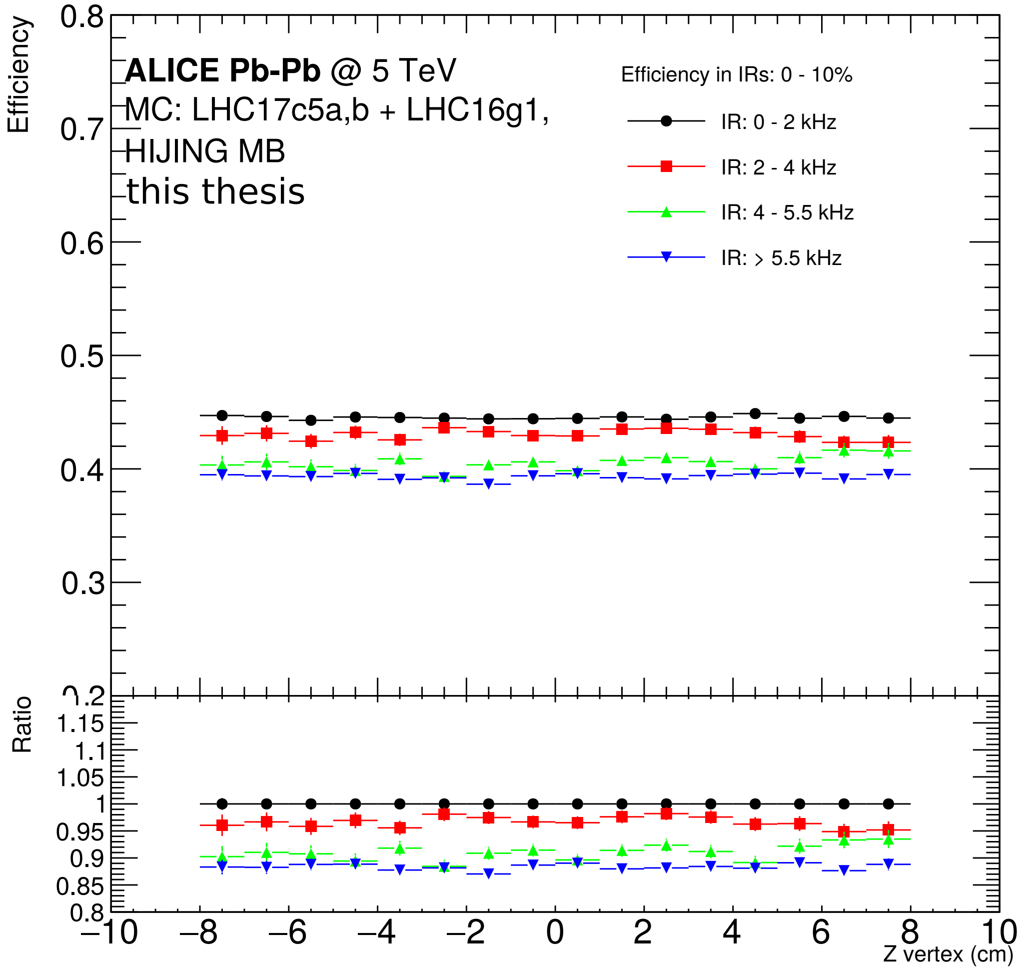

Figure 4.14: Single track reconstruction efficiency for protons projected on the z_{vertex}. The used MC simulation is from HIJING Minimum-Biased events (MB). LHC17c5a,b for IR in 0 to 2kHz and LHC16g1 for IR larger than 2kHz. Projected z_{vertex} efficiency is for particles with $p_{\text{T}} = 2$ to 4 GeV/c and the full range of η_{track} (± 0.8). The bottom panel shows the efficiency ratio relative to the lowest IR result (0-2kHz).

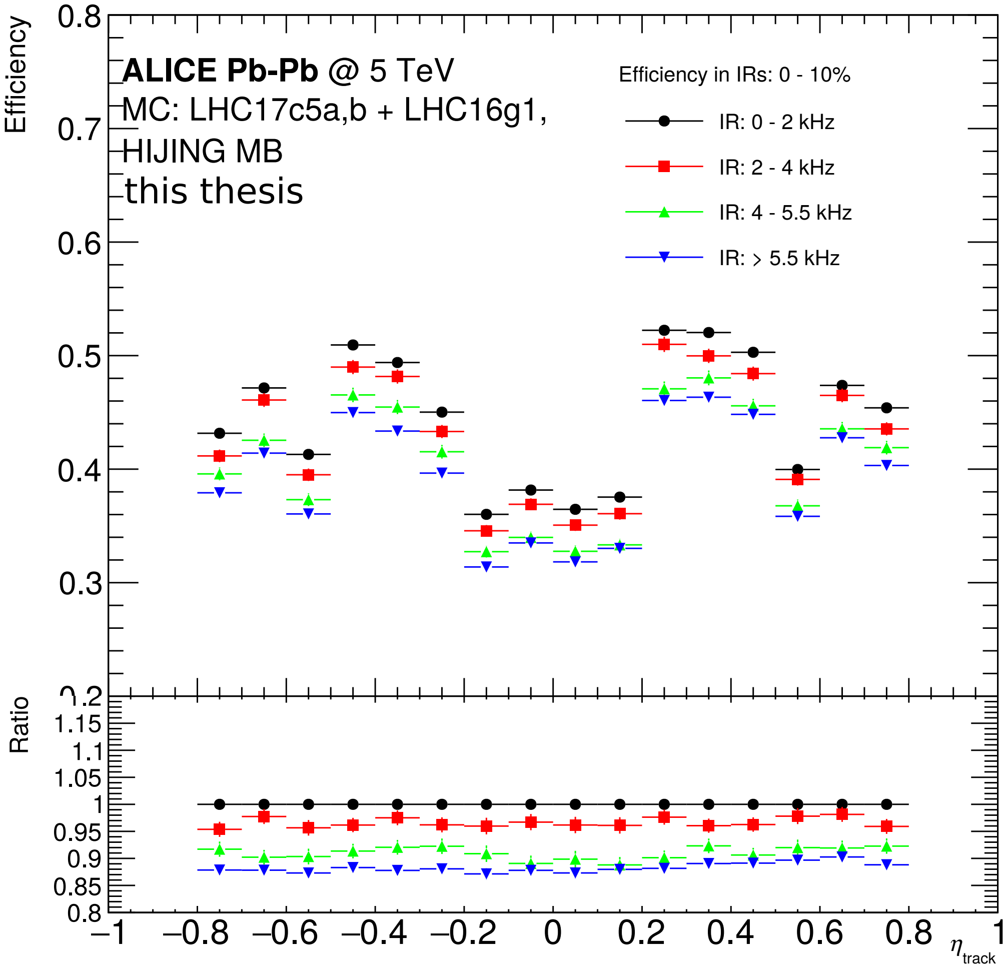

Figure 4.15: Single track reconstruction efficiency for protons projected on the η_{track}. The used MC simulation is from HIJING Minimum-Biased events (MB). LHC17c5a,b for IR in 0 to 2kHz and LHC16g1 for IR larger than 2kHz. Projected η_{track} efficiency is for particles with $p_{\text{T}} =$ 2 to 4 GeV/c and the full range of z_{vertex} (±8cm). The bottom panel shows the efficiency ratio relative to the lowest IR result (0-2kHz).

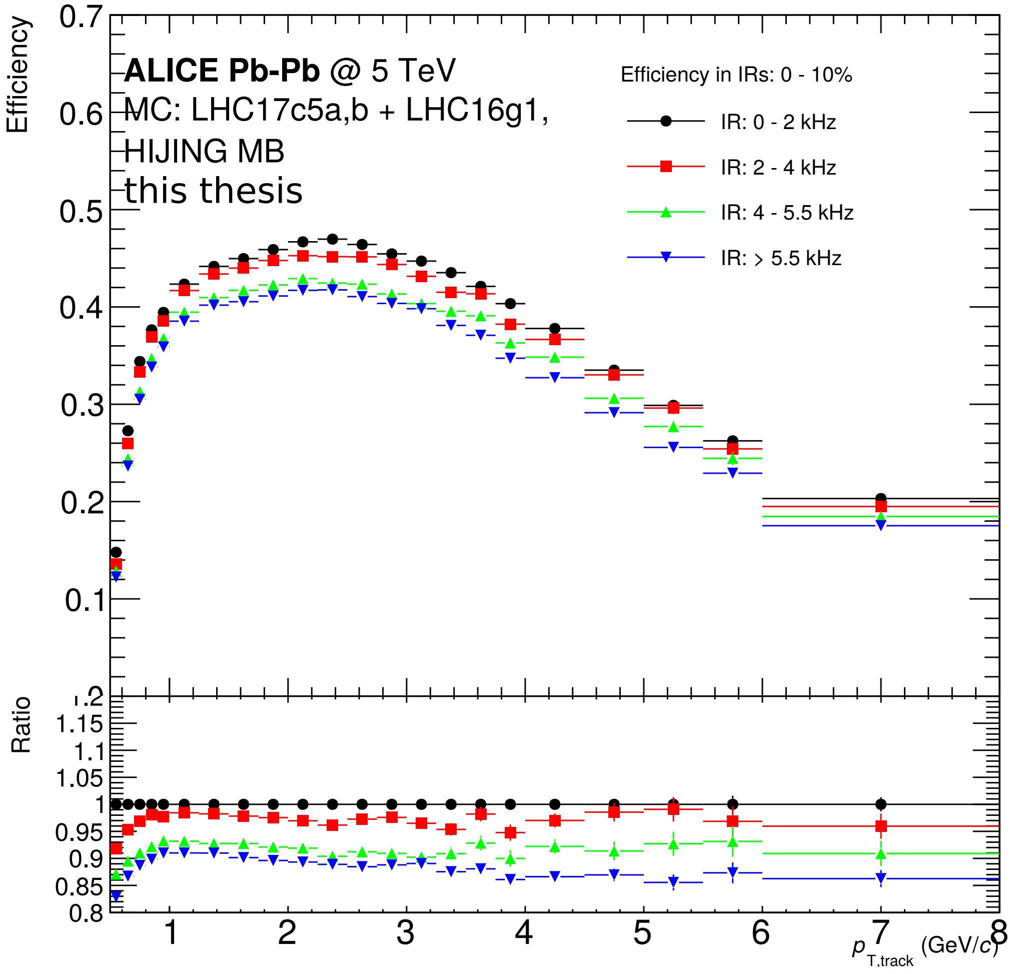

Figure 4.16: Single track reconstruction efficiency for protons projected on the $p_{\mathrm{T}}^{\mathrm{track}}$. The used MC simulation is from HIJING Minimum-Biased events (MB). LHC17c5a,b for IR in 0 to 2kHz and LHC16g1 for IR larger than 2kHz. Projected $p_{\mathrm{T}}^{\mathrm{track}}$ efficiency is for particles with the full range of z_{vertex} and η_{track} (±8cm, ±0.8). The bottom panel shows the efficiency ratio relative to the lowest IR result (0-2kHz).

how many soft (thermal) particles are above 5 GeV/c. In other words, the fraction of hard scattered particles at particular p_{T} can be estimated from the comparison. The species-averaged fraction is about 90% at 5 GeV/c. This study concluded that the leading constituents above 5 GeV/c are mostly induced from hard scattered particles, and this cut helps avoid combinatorial jets consisting of soft thermal particles only. Hence, this leading constituent cut was used in the present analysis.

Although the leading constituent cut works for reducing combinatorial jets, there are some remaining fake jets. Another p_{T} cut was applied to remove the remaining fake jets, the background-subtracted jet $p_{\mathrm{T,corr}}^{\mathrm{jet}}$ should be above 25 GeV/c. The background subtraction in jets is described in Sec. 3.5.4.1. The Random Cone (RC) method was used to check the effectiveness of the $p_{\mathrm{T,corr}}^{\mathrm{jet}}$ cut. This method is commonly used in jet-related analyses. In the RC method, a random axis in φ-η is assigned in every event in data. Based on the random axis (called the RC axis), an RC "jet" is formed with nearby tracks. In this process, the jet algorithms are not used. All tracks in an event are checked about a spatial distance between the track and the RC axis, based on the φ, η position:

$$\Delta_{\mathrm{RC},i} = \sqrt{(\eta_{\mathrm{RC}} - \eta_i)^2 + (\varphi_{\mathrm{RC}} - \varphi_i)^2} < R \tag{4.5}$$

The tracks are included in RC if the distance is smaller than the jet radius (R). The p_{T} of the RC is calculated as the sum of the p_{T} of all included tracks.

RC jets usually contain lots of background tracks, so it is interesting to see the background-subtracted jet p_{T} in RC jets. The background subtraction in the RC gives us information about possible background fluctuations in the subtraction method. The background-subtracted p_{T} for RC jets is called background density fluctuation (δp_{T}) and calculated like this:

$$\delta p_{\mathrm{T}} = p_{\mathrm{T}}^{\mathrm{RC}} - \rho \cdot \mathrm{A}^{\mathrm{RC}} \tag{4.6}$$

Figure 4.18 shows the obtained δp_{T} distribution in our data. There are δp_{T} distributions from three different RCs: gray points show a basic RC result, and blue and red points have additional processes to exclude true jet contributions in the RC jets. A leading jet (with the highest $p_{\mathrm{T}}^{\mathrm{jet}}$) and sub-leading jet (with the second highest $p_{\mathrm{T}}^{\mathrm{jet}}$) are used in the additional processes. Both jets are clustered in the standard way with the anti-k_{T} algorithm. Note that the used $p_{\mathrm{T}}^{\mathrm{jet}}$ to determine the leading and sub-leading jets is the background-subtracted jet p_{T} ($p_{\mathrm{T,corr}}^{\mathrm{jet}}$). These two jets are most likely to be true jets in an event. So, in the RC method, if the RC axis is close to the leading jet/sub-leading jet within 2R, such an RC jet is excluded from the δp_{T} distribution. The blue points show the case where only the leading jet is removed, and the red points show the result when the leading and sub-leading jets are rejected.

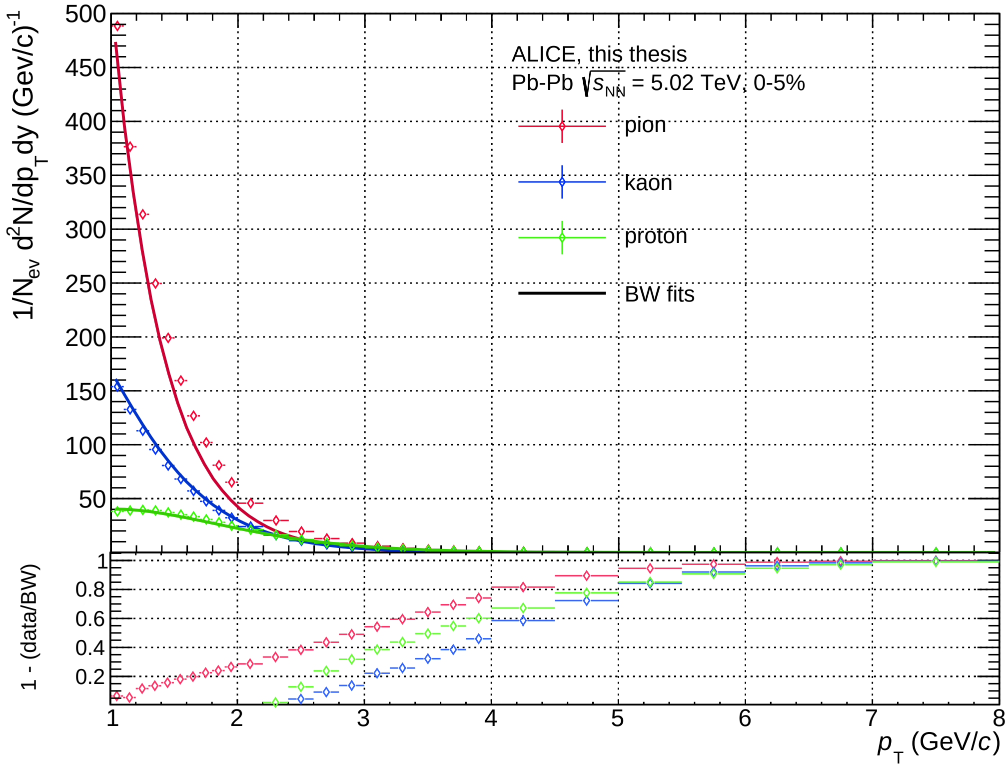

Figure 4.17: Comparison between particle p_{T} spectra measured in Pb–Pb collisions at $\sqrt{s_{\mathrm{NN}}} = 5.02$ TeV and Blast-wave fits to the data. Only 0 - 5% centrality results are plotted. The fit and spectra were obtained from this paper [153] (internally contacted to the author). The bottom panel shows the fraction of hard particles defined as 1-(data/BW). No separation between different interaction rates (IRs) was done for this study.

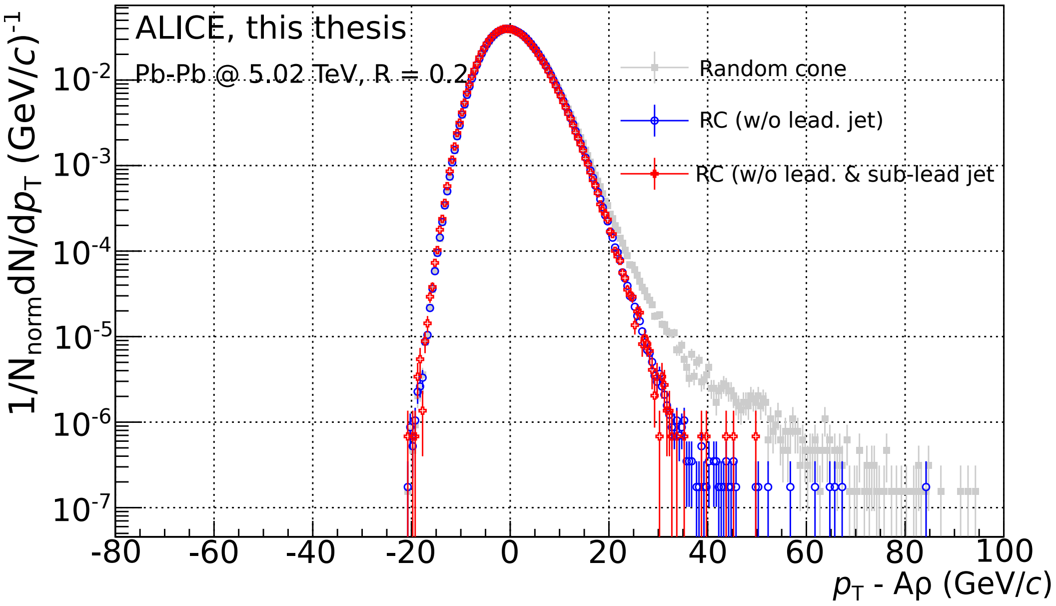

Figure 4.18: Distribution of δp_{T} obtained by the RC method. 0-10% centrality results are plotted. This plot was obtained from the lowest IR result (0-2kHz). The leading and sub-leading jets are real jets, clustered by the anti-k_{T} algorithm with nominal cuts. All histograms are normalized to be matched with the same integral value between -20 to 0 (background-dominant area).

All three distributions are mainly Gaussian shaped and centered around 0, with a tail on the right side. The right-side tail comes from the true jet contribution or other hard scattered particles. Thus, this tail is reduced when excluding the RC jets close to the leading and sub-leading jets. The difference between removing the leading jet only or both jets is not significant. 2σ of a Gaussian fit to the δp_{T} distribution on the negative sign of δp_{T} is used to estimate the size of background fluctuations in data. Although we cannot ignore possible contributions from true jets on the positive side, the negative distribution is assumed to be fully due to the background fluctuations.

The δp_{T} study explained above is commonly done in similar analyses to estimate background fluctuations with the RC method [121]. However, we checked another effect in this study, considering the leading constituent cut applied in the jet selection.

The leading constituent cut and the jet p_{T} cut (determined by 2σ in the background density fluctuation) are used together for the present analysis. Thus, we needed to check δp_{T} when the leading constituent cut is applied in RC jets. Several approaches were used to adapt the leading constituent bias in RC jets. First, we made a δp_{T} distribution shifted by 5 GeV/c from the previous RC results. They are shown in blue and magenta in Fig. 4.19. They have a similar trend as before, and the difference between 'without leading jet' (blue) and 'without leading and sub-leading jets' (red) is negligible.

Another approach was to replace a track in the RC by one having $p_{\mathrm{T}} \geq 5$ GeV/c manually. The replaced p_{T} in the RC jets was randomly picked according to the measured track p_{T} distribution above 5 GeV/c. Those results are seen in Fig. 4.19 with green and orange points. The difference between the online (green) and the offline (orange) is when the track p_{T} is replaced. The online way replaces the track during the RC jet clusterization, and the offline way replaces the track in an already-filled RC jet histogram, re-filling it with the p_{T} modification. Both results show a significant tail on the higher δp_{T} range. Such a tail looks similar to the tail in anti-k_{T} jet distribution (black). These anti-k_{T} jets were obtained via the standard jet clusterization with a leading constituent cut of 5 GeV/c. The background-subtracted jet p_{T} corresponds to δp_{T}. Thus those distributions can be directly compared. The long tail in the replacement method (green and orange), like anti-k_{T} jets, is because an extremely high p_{T} track is rarely picked up and implemented in RC jets. Since we used the measured p_{T} distribution to replace a p_{T}, some high p_{T} tracks seriously affect the RC jets' p_{T}. Moreover, these high p_{T} tracks can originate from jets. This interpretation led us to make the final approach shown as pink in Fig. 4.19.

What we want to know is if the pure background fluctuation distribution has a constituent cut bias. Therefore, the replaced track should not originate from a jet or

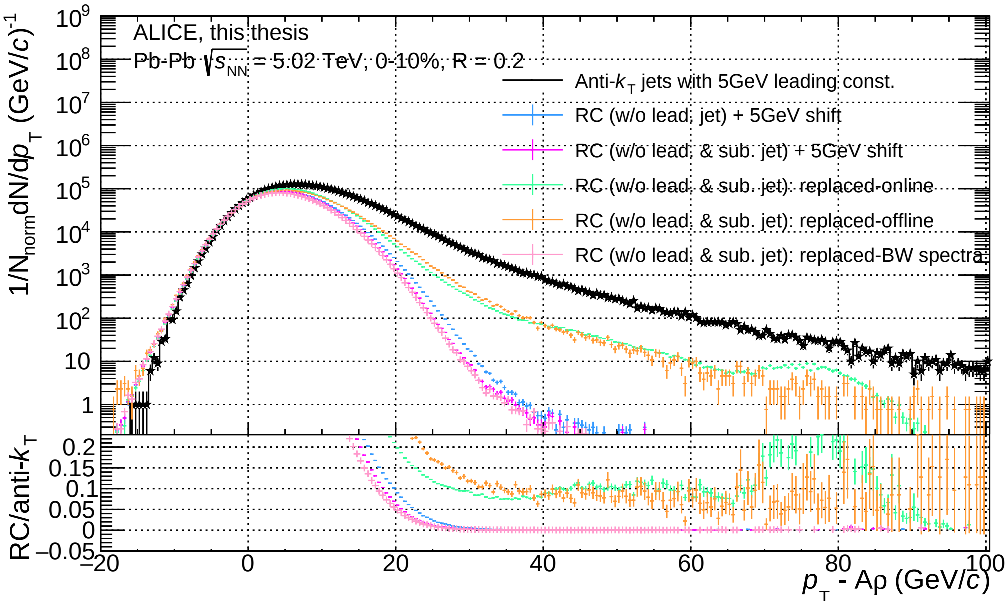

Figure 4.19: Distribution of δp_T from different random cone methods. 0-10% centrality results are plotted. This plot was obtained from the full statistics of LHC15o. The leading and sub-leading jets are jets, clustered by the anti-k_T algorithm with nominal cuts. All histograms are normalized to be matched with the same integral value between -20 to 0 (background-dominant area). The bottom panel shows the ratio of different RC results (colored points) to anti-k_T jets result (black), showing the fraction of possible fake jets.

any hard scattered process but from the background like thermal production. The blast-wave fit spectra, describing soft thermal production, provide such information to us. In the final approach, we replaced a track in an RC jet, sampling a p_{T} from the blast-wave fit above 5 GeV/c. So, the final (pink) represents a pure background density fluctuation having a leading constituent bias.

The blast-wave replacement (pink) result looks similar to the basic shifted methods (blue and magenta). It implies that the RC method is working well to account for the background fluctuation, and the shape of background fluctuation is not changed with the leading constituent bias.

Via comparison between the anti-k_{T} jets (black) and the RC with blast-wave replacement (pink), we obtained an estimation of expected fake jets in the given δp_{T} (equivalent to background-subtracted $p_{\mathrm{T}}^{\mathrm{jet}}$). Finally, we concluded that applying a jet p_{T} cut $= 25$ GeV/c in the present analysis results in less than 3% combinatorial jets in our jet selection.

4.5.2 Final selected jets

We have discussed all jet cuts and selections to be adapted in this analysis. Finally, we obtained 89k jets in the LHC 15o dataset, listed in Table 4.5. With those jets, we correlated all unidentified hadrons/protons produced in the same event as described in Ch. 5.

IR	**Num of jets**	**Proportion [%]**
<2 kHz	4 k	4
2 - 4 kHz	22 k	25
4 - 5.5 kHz	21 k	24
>5 kHz	42 k	47
Total	89 k	100

Table 4.5: Number of analyzed jets in each IR dataset.

5 Jet-hadron and Jet-proton correlation

As discussed in Ch. 2, our interest in this research is looking into the QGP medium response to search for a sound shock wave that can be produced by hard-scattered partons. An angular correlation analysis is useful to see the spatial distribution of produced particles around jets. Since the sound wave signal is created at a certain angle (depending on the medium properties: viscosity and v_{s}) from the parton axis, the signal can be observed as a particular structure in the angular correlation.

In this analysis, jets are used as a proxy for hard-scattered partons. The jets and unidentified hadrons/protons used in the correlation functions measured here are discussed in Ch. 4.

5.1 Correlation analysis method

With the selected jets and unidentified hadron/proton tracks, an angle difference between the jet axis and every track per event is calculated as:

$$\begin{aligned} \Delta\varphi &= \varphi_{\mathrm{jet}} - \varphi_{\mathrm{track}}, \\ \Delta\eta &= \eta_{\mathrm{jet}} - \eta_{\mathrm{track}} \end{aligned} \tag{5.1}$$

Since $\Delta\varphi$ is periodic, it is shifted to always be in the range $-\frac{\pi}{2} < \Delta\varphi < \frac{3\pi}{2}$. If it is outside the range, the $\Delta\varphi$ value is corrected as follows:

$$\begin{aligned} \Delta\varphi' &= \Delta\varphi - 2\pi, \quad \text{when } \Delta\varphi > \frac{3\pi}{2} \\ \Delta\varphi' &= \Delta\varphi + 2\pi, \quad \text{when } \Delta\varphi < -\frac{\pi}{2} \end{aligned} \tag{5.2}$$

Such a pair calculation between jets and tracks is accumulated over events. The angular correlation is the distribution of the pairs with the relative angles defined in Eq. 5.1:

$$\frac{\mathrm{d}^2 N}{\mathrm{d}\Delta\varphi \mathrm{d}\Delta\eta} = \frac{1}{N^{\mathrm{trig}}} N^{\mathrm{pair}}(\Delta\varphi, \Delta\eta) \tag{5.3}$$

where the correlation function is normalized with the number of jets (considered triggers in the present analysis). This correlation function is the averaged spatial distribution of particles with respect to the jet axis.

5.2 Raw correlation and corrections

The raw correlation function includes non-physical correlations and effects of detector performance, therefore correction procedures are needed to obtain the true correlation function. The applied corrections are described in the following sections.

5.2.1 Event-mixing

The event-mixing technique is a way to remove the contribution of some of the non-physical correlations induced by limited detector acceptance. The correlation functions obtained in the same event include both physical correlations and non-physical correlations from the detector effect. However, if one measures correlation functions between jets and tracks from different events, they contain only non-physical correlations but not physical correlations. This feature is used in the mixed event method.

The correlation functions were calculated in the same events and mixed events in the analysis. Figures. 5.1 and 5.2 show examples of the correlation functions. In both results, a visible triangular shape along $\Delta\eta$ is observed.

This triangular shape in $\Delta\eta$ is statistically produced when the correlation functions are calculated with uniformly distributed jets and tracks in a given range of η. In the case of a uniform distribution of jets and tracks in η, the maximum deviation $\Delta\eta$ can only be obtained when a jet and a track are located at the ends respectively. This case is much rarer than others, while the deviation close to 0 is the most probable case in the correlation functions. The reason why this shape does not show up in $\Delta\varphi$ is because the φ coordinate is periodic. In particular, a triangular shape with a plateau at some range at the center is shown. This plateau range is dependent on the different η ranges for tracks and jets. This triangular shape is one of the non-physical correlations, and the mixed event method corrects it.

The correlation functions in the same events and in the mixed events are referred to $S(\Delta\varphi, \Delta\eta)$ and $B(\Delta\varphi, \Delta\eta)$. The corrected correlation function is obtained by dividing the same event correlation by the mixed event correlation function:

$$\frac{\mathrm{d}^2N}{\mathrm{d}\Delta\varphi\mathrm{d}\Delta\eta} = \frac{1}{N^{\mathrm{trig}}}\frac{S(\Delta\varphi, \Delta\eta)}{\frac{1}{\alpha}B(\Delta\varphi, \Delta\eta)} \tag{5.4}$$

For this step, a normalization is required for the mixed event correlation function. The normalization factor (α) is determined to make the correlation to be 1 on the top (plateau) of the triangle shape. It was obtained by a zero-polynomial fit on the plateau range. This normalization is important because it enables us to

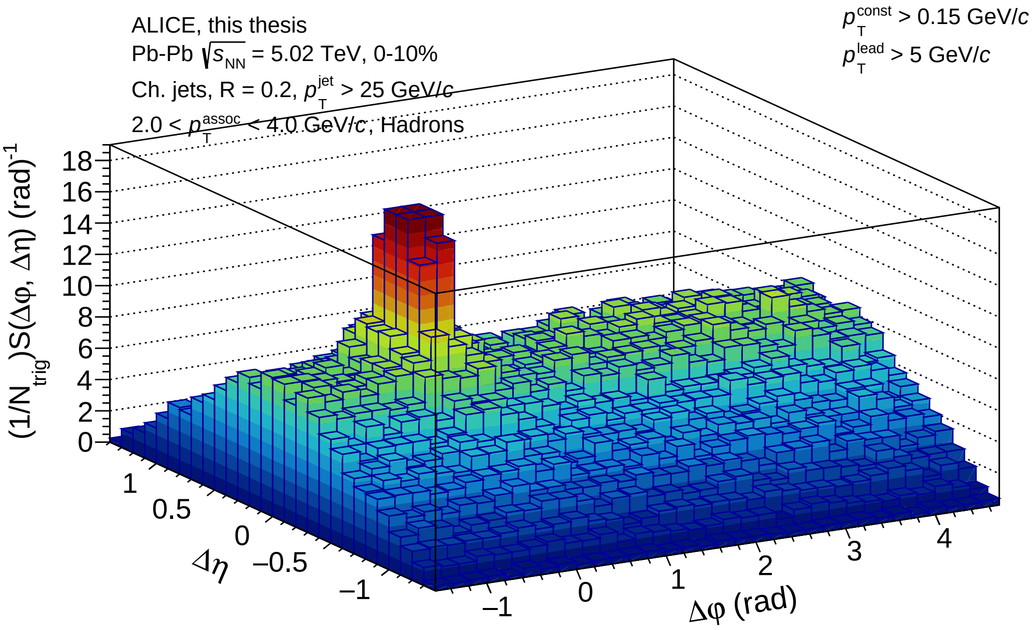

Figure 5.1: Raw correlation functions between jets and unidentified hadrons, measured in the same event. Applied cuts are shown in the legend. This result shows the raw correlations at the z_{vertex} between -1 to 0 cm in the highest IR (>5.5kHz).

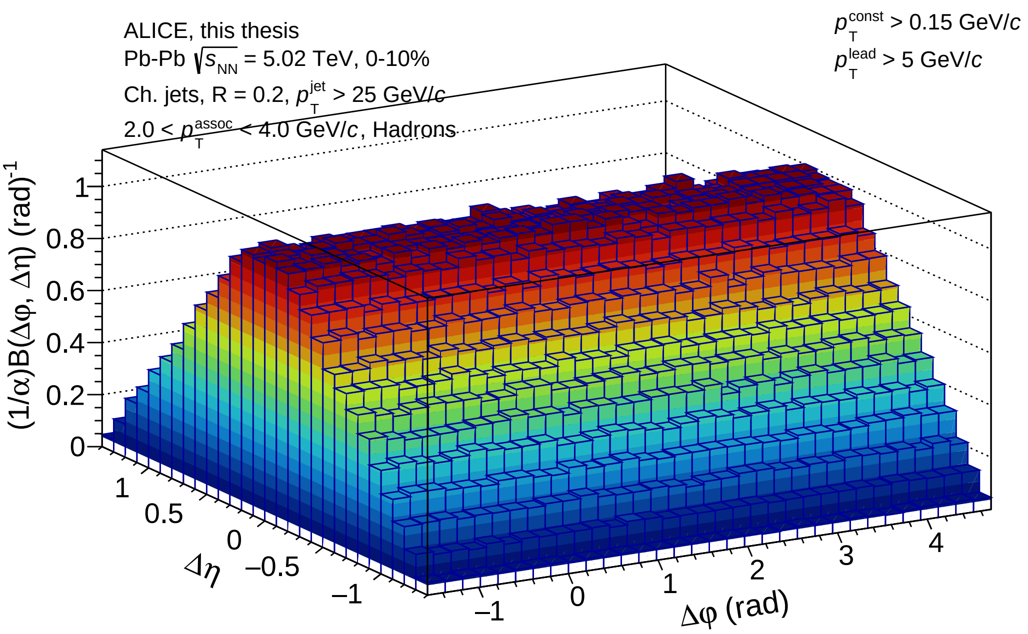

Figure 5.2: Normalized raw correlation functions between jets and unidentified hadrons, obtained in the mixed events. Jet and tracks belong to different events. Applied cuts are shown in the legend. This result shows the raw correlations at the z_{vertex} between -1 to 0 cm in the highest IR (>5.5kHz).

correct the non-physical shape but does not affect counts of physical correlations in the raw function. For that purpose, the mixed-event normalization is always performed to avoid a value change at $(\Delta\varphi,\ \Delta\eta) = (0,\ 0)$, where it corresponds to the location of the jet axis in the correlation functions.

The mixed-event correction functions contain only a statistical shape (triangular shape) but also non-physical correlations induced by the detectors. The detector performance is sensitive to and changes depending on the event conditions like centrality and z_{vertex}, so only events measured under similar conditions are mixed. This allows us to obtain a more improved mixed event distribution containing condition-sensitive detector effects. This analysis considers IR (interaction rate), z_{vertex}, and centrality for different mixed event pools. The mixed event correction and efficiency correction (described in the following section) were done separately in each IR group. Events were categorized into 16 z_{vertex} pools with 1 cm bin width in -8 to 8 cm. In the given mixed event pools, only 0 - 10% of central events were mixed. Events with centrality $>$ 10 % were rejected. These mixed event distributions are used to correct the raw correlation functions (same-event distributions) from the same centrality and z_{vertex} bin. In the end, many possible non-physical correlations are eliminated via the mixed event method.

5.2.2 Tracking efficiency in correlation function

Measured tracks in the experiment are always biased by detector efficiency. As explained in Sec. 4.3.2, the single track reconstruction efficiency was obtained from MC simulation results. We count the number of pairs between jets and tracks in correlation functions and normalize the functions with the number of jets. Therefore, tracks involved in correlation functions should be corrected by the single track efficiency in order to obtain the total number of pairs without detector efficiency.

We used 3-D single track efficiency in η, z_{vertex}, and p_{T} of the tracks. If we have the efficiency value (ϵ) for a track at a certain η, z_{vertex}, and p_{T}, the correction is done by filling the correlation function at the location of the pair $(\Delta\varphi,\ \Delta\eta)$ with the $1/\epsilon$.

For this correction, bin widths in 3-D efficiency plot can work as a sort of resolution. Due to limited statistics in MC, we cannot use infinitely small bin widths since it enhances statistical fluctuations. We scrutinized various efficiency plots, and decided on 1cm bin width for η and z_{vertex}, and 0.25 GeV/c width for p_{T} between $2 < p_{\mathrm{T}} < 4$ GeV/c.

5.3 Fully corrected jet-hadron correlation & jet-proton correlation

After applying the mixed event correction and the single track reconstruction efficiency correction, jet-hadron correlations and jet-proton correlations are shown in Figs. 5.3, 5.4. 2-D distributions for both particles are displayed.

For this final result, individual results in different IRs are merged. Note that the individual results passed through all corrections separately, and the outputs were merged only after rescaling based on the number of events available in different IRs.

In both correlation functions, a single dominant peak is shown around ($\Delta\varphi$, $\Delta\eta$) = (0, 0). The position of (0, 0) means the same φ and η values between jets and tracks. This is an observation of jet fragmentation in the correlation function. There is two regions in the correlation function of $\Delta\varphi$: $\Delta\varphi$ from -$\pi/2$ to $\pi/2$ is called the near-side range and $\Delta\varphi$ from $\pi/2$ to $3\pi/2$ is called the away-side range, which refers to an area nearby trigger jets and the area nearby the opposing jets. These terms are often used in the following for explanation and interpretation of the results.

It is hardly seen in the 2-D histograms, but there are some wide peak structures around $\Delta\varphi = \pi$ along the $\Delta\eta$ axis. A convolution of varied mechanisms produces this peak: first, since jets are back-to-back on the azimuthal plane, the opposing jets (called away-side jets in folliwing) should be placed at $\Delta\varphi = \pi$, and the fragmentation of the away-side jets can produce a peak in the away side. Besides, the jet axis is not back-to-back on $\Delta\eta$, due to the initial momentum fluctuation of the partons in the nucleon. Precisely, the partons have fluctuating momentum values in the longitudinal (or z) direction. The vector sum of these initial values decides the total momentum in the longitudinal direction. This total momentum in the longitudinal direction is different in every hard scattering, and it makes a different position of the away side jet on η every time, satisfying the momentum conservation rule. As a result, the away-side jets are distributed along $\Delta\eta$

Second, assuming that the away-side jet is quenched in the QGP medium, the deposited energy in the medium continues to particle production around the away-side jet. The medium-produced particles are included in jet-hadron and jet-proton correlations and enhance the width of the peak on the away-side because the medium-produced particles largely distributed compared to the jet fragmentation. Then, if the Mach cone is created by the away-side jet in the QGP, that contribution is also resulted in an increase of the width. In addition, after traversing the QGP medium, since the quenched jet (or parton) has a lower energy than the original energy, the quenched jet has a relatively larger opening angle in the gluon emission, since the opening angle depends on the energy of jets, $\theta \simeq \frac{m}{E}$ [154]. This

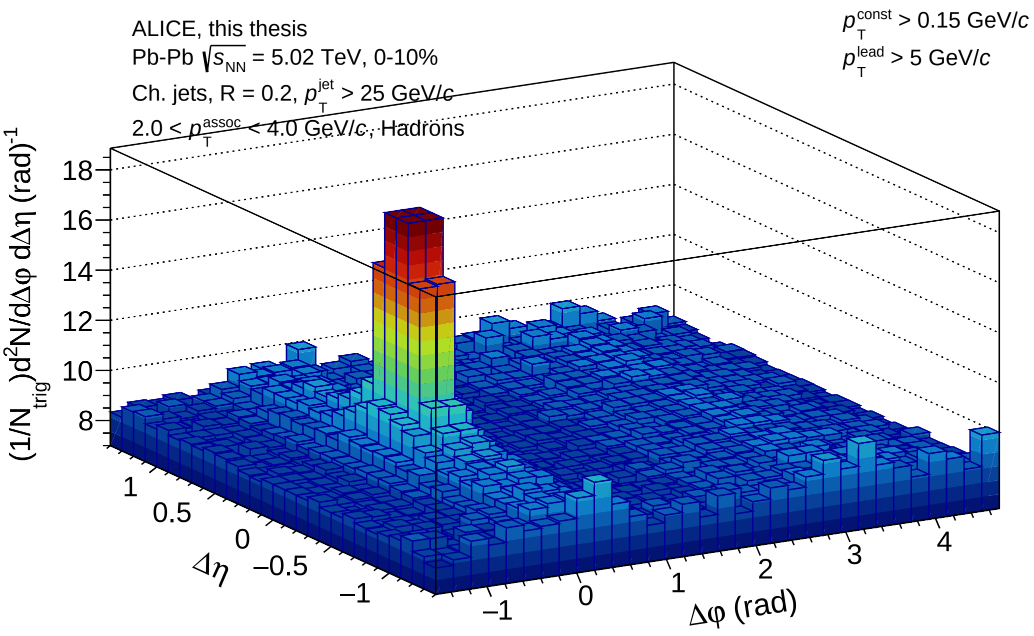

Figure 5.3: True correlation functions between jets and unidentified hadrons, normalized by the number of jets. Mixed event correction and single track reconstruction efficiency correction are done. Results are obtained in 0-10% centrality. This is the full statistics of LHC15o, merging different IRs into the final result. Applied cuts for jets and associated hadron tracks are shown in the legend.

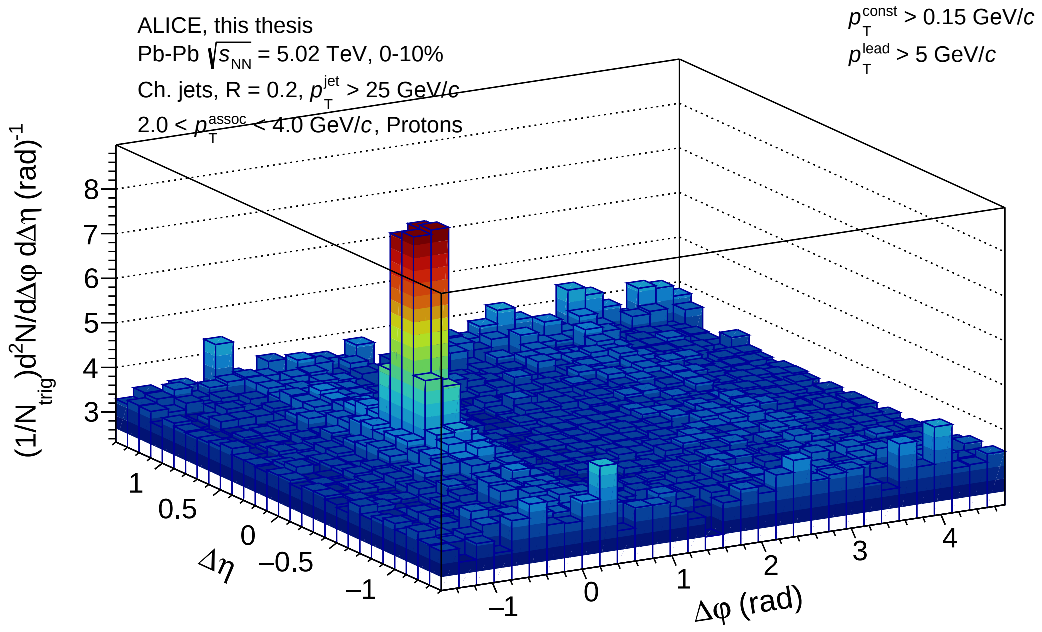

Figure 5.4: True correlation functions between jets and identified protons, normalized by the number of jets. Mixed event correction and single track reconstruction efficiency correction are done. Results are obtained in 0-10% centrality. This is the full statistics of LHC15o, merging different IRs into the final result. Applied cuts for jets and associated proton tracks are shown in the legend.

contributes to the width enhancement as well.

Third, the flow effect is also observed in the correlation functions. This flow, in particular v_2 (a dominant coefficient), contribute the peaks on the near side and the away side, which usually have wider widths compared to the width from the fragmentation. In the case of v_3, since it is expected to be the two peaks on the away side in the correlation functions, it can contribute to the width enhancement on the away-side.

Observations for unidentified hadrons and protons in the 2-D histogram are pretty similar. One visible feature is that there are more significant fluctuations in protons due to limited statistics. Projections on $\Delta\varphi$ and $\Delta\eta$ show more precisely the structure of the peaks. More physics discussion is continued in Sec. 5.5.

5.4 Systematic uncertainty

Before interpreting and discussing the obtained results, systematic biases of the observable from analysis methods or setup of the measurements should be considered. In the study of systematic errors, it is common to check the analysis results according to different cuts applied for the analysis. The resulting difference between the default and a varied cut is regarded as a systematic error.

However, understanding the used cut variations is essential in these kinds of studies. When we use different cut values for systematic checks, it can induce additional statistical fluctuations if the cut value is too loose/strict. Therefore, before taking the result difference as a systematic uncertainty, an additional step is required.

The Barlow test [155] is a way to judge whether this systematic deviation is significant compared to statistical fluctuations among the sub-groups used to check the uncertainty from different cut parameters. In the Barlow test, the difference of the analysis observable (in this analysis, correlation functions) between the default and the varied cut is defined as:

$$\Delta = \text{Correlation(default)} - \text{Correlation(variation)} \tag{5.5}$$

If the default/the varied cut is a sub-group of the other, the variance for the difference (Δ) can be shown as:

$$\sigma = \sqrt{\sigma^2_{\text{def,stat}} - \sigma^2_{\text{var,stat}}} \tag{5.6}$$

where σ refers to a statistical fluctuation, which is calculated as the standard deviation of a given statistics in a given bin. The Barlow criteria is calculated as the ratio between the difference and the variance:

$$\text{Barlow criteria} = \frac{\Delta}{\sigma} \tag{5.7}$$

This Barlow criteria value can be used as an indicator to decide a systematic deviation for a cut has to be considered as a systematic bias or not. If the Barlow criteria are close to a Gaussian distribution, it implies that the systematic deviation for this varied cut is affected by statistical fluctuations. A standard Gaussian distribution has a mean equal to zero and a standard deviation equal to 1. However, we used a cut value of 1.5 to decide whether a variation is statistically significant with limited statistics. Correlation functions and Barlow values were checked for different sources of systematic bias: magnetic field polarity, z_{vertex} range, pseudorapidity range, track filter bit, tracking efficiency, and IR dependence. For each case, if the mean of the Barlow distribution is not close to zero, or if the standard deviation of the distribution is above 1.5, that source is included in the final systematic uncertainty.

In the case of the magnetic field effect, two directions of the magnetic fields were applied in the measurements, ± 0.5 T, and those sets are mixed in the default analysis. For the uncertainty study, jet-hadron correlation functions were obtained for different magnetic field configurations, and compared in $\Delta\varphi$ and $\Delta\eta$, as shown in Fig. 5.5. The default result is shown as black points, and red and blue are the positive and negative signs. The bottom pad shows the ratio between the positive/negative sign and the default result. About a 1% difference is shown in the ratio of the correlation functions. The Barlow criteria distributions have smaller standard deviations than 1.5 in both $\Delta\varphi$ and $\Delta\eta$ (see Fig. 5.6). Based on this, we concluded that the systematic uncertainty due to the magnetic field is not significant and is therefore not taken into account for the final systematic uncertainty.

When it comes to the z_{vertex}, the default range is ± 8 cm, and the variation range is ± 6 cm. Like the magnetic field case, correlation functions were obtained for each z_{vertex} selection, as shown in Fig. 5.7. The Barlow criteria distribution is shown in Fig. 5.8. The difference between the default and 6cm z_{vertex} range is within 1%, except for outliers in the edge of $\Delta\eta$. The Barlow distribution also passed the cuts for the mean and standard deviations. Therefore, the z_{vertex} was also not considered as a factor of systematic uncertainty in the correlation functions.

The Barlow test confirmed that the magnetic field and z_{vertex} do not have significant systematic uncertainty with respect to statistical fluctuations in jet-hadron correlations. Without additional checks on the jet-proton correlations, since jet-proton correlations are a sub-group of hadron correlation statistically, we adopted the same conclusion to the proton case. As a result, the magnetic field and z_{vertex} were not included in the final systematic uncertainty of the jet-proton correlations as well.

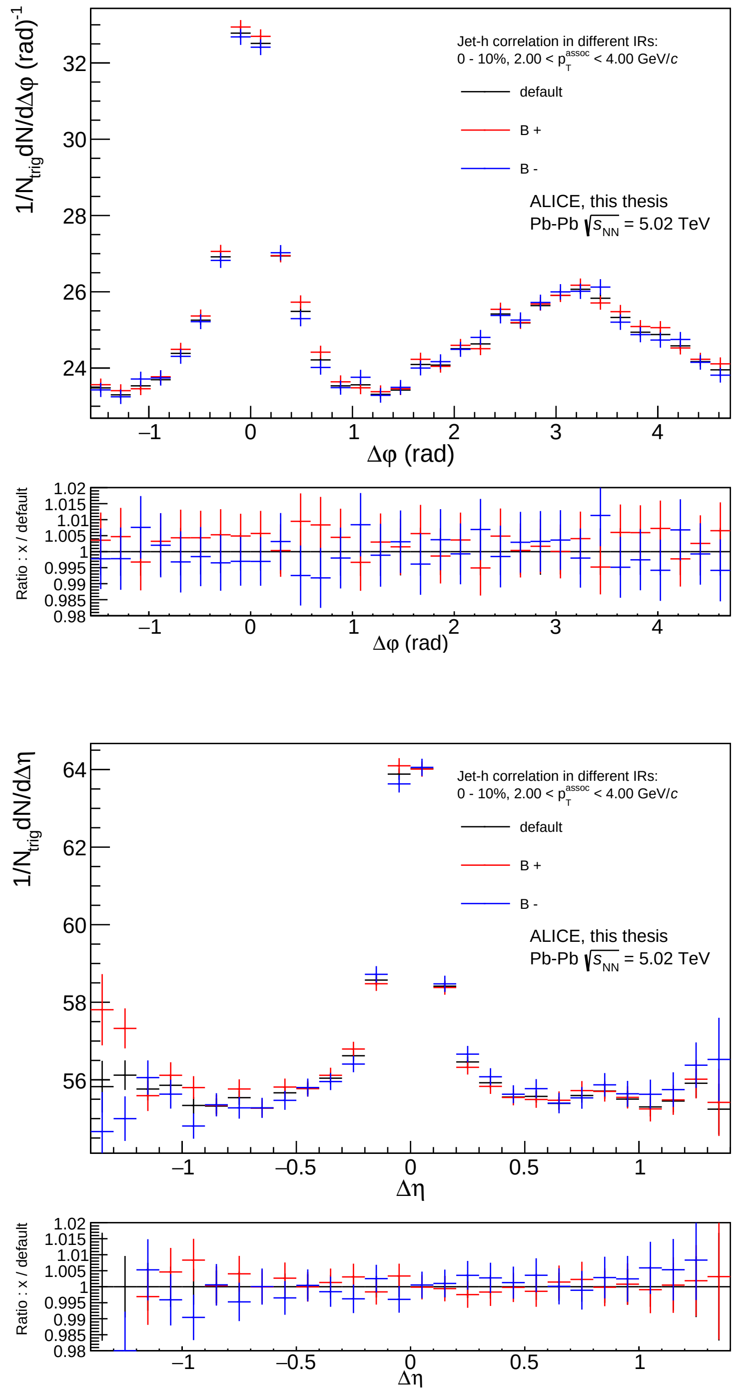

Figure 5.5: Comparison of jet-hadron correlations between different signs of the B field. Correlation function in $\Delta\varphi$ (top) and $\Delta\eta$ (bottom) and the ratio (bottom pad of each plot) of different B signs (±) to default (mixed) are shown. This plot was obtain in the highest IR (>5.5kHz, highest statistics).

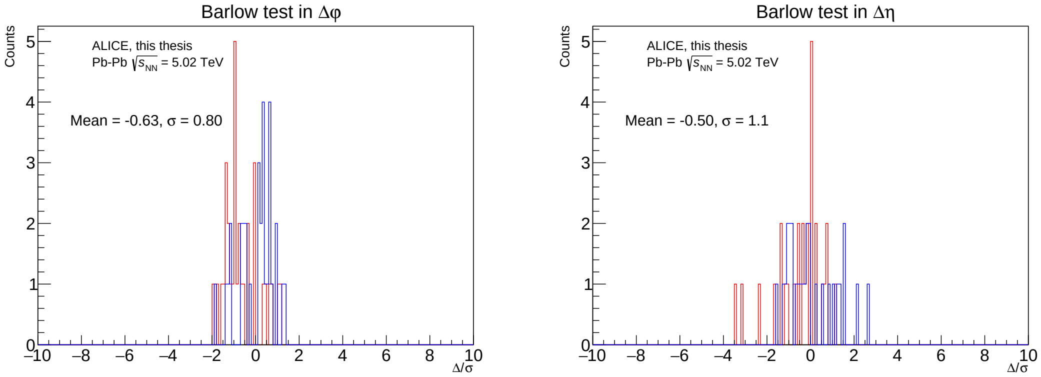

Figure 5.6: Barlow criteria distribution of different sign of the magnetic fields in the $\Delta\varphi$ (left) and $\Delta\eta$ (right). The red and blue histogram correspond to the Barlow criteria distribution for the positive and negative sign of the magnetic field, respectively. The mean and sigma of the inclusive result are shown on the left side of the panels.

In the case of the pseudorapidity (η) range, the default cut ($|\eta| < 0.8$) and a tight cut ($|\eta| < 0.6$) were used for comparisons. Jet-hadron correlations and Barlow test results are shown in Fig. 5.9, and 5.10. In the bottom panels of Fig. 5.9, the differences between the default and the varied cut are about 2% and 1% in $\Delta\varphi$ and $\Delta\eta$, respectively. Note that the default and the tight cut have different ranges in $\Delta\eta$ due to different η cuts. For instance, correlation functions for tracks in $|\eta| < 0.6$ and jets in $|\eta| < 0.4$ (equal to η_{track}- R) have maximum/minimum limits at $\pm$ 1.0 in $\Delta\eta$ range. One more observation in comparisons of correlation functions is that the ratios are systematically below 1. Such trends are observed in both $\Delta\varphi$ and $\Delta\eta$. The Barlow distributions, as shown in Fig. 5.10, are also pretty different from the cases of z_{vertex} and the sign of the magnetic field. The overall distributions are shifted to the positive side, having large mean values 1.1 in $\Delta\varphi$ and 2.6 in $\Delta\eta$. Thus, the η range was included in the final systematic uncertainty. The point-by-point ratio between the default and the tight η cut was taken into account as an uncertainty. The statistical error for a given point is estimated as an error propagation of the statistical error of the default cut and that of the tight η cut for the given point.

As discussed in Sec. 4.3.1, hybrid tracks with filter bit 768 were used in this analysis. We checked uncertainties from different track bit selections with bit 96 and bit 16. Applied cuts in each bit can be found in Table 5.1. More information about the cuts can be seen in Sec. 4.3.1. The main difference between the default bit (768) and one of the standard track bits (96) is the DCA cut. In hybrid track, the cut values are more loose, 2.4 and 3.2 in xy and z, but track bit 96 uses tighter

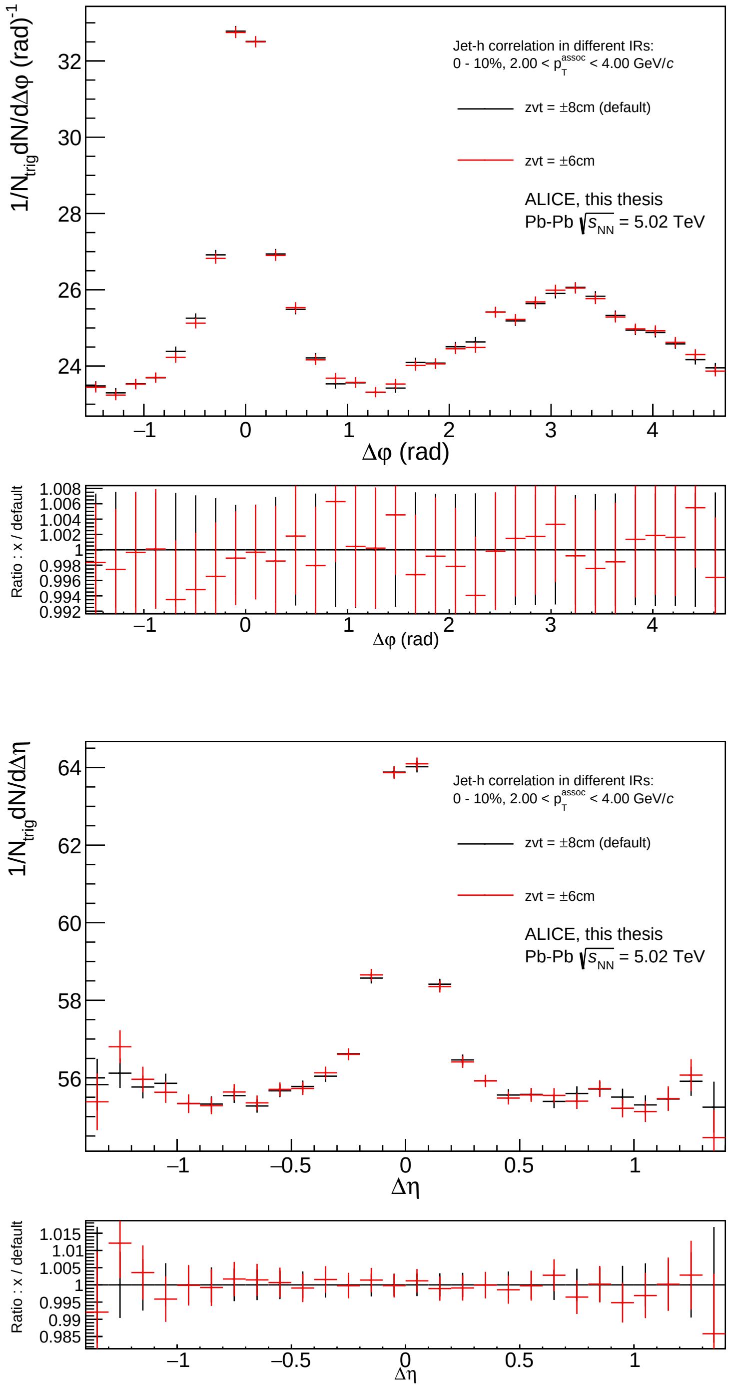

Figure 5.7: Comparison of jet-hadron correlations between different z_{vertex} ranges. Correlation function in $\Delta\varphi$ (top) and $\Delta\eta$ (bottom) and the ratio (bottom pad of each plot) of different z_{vertex} cut (±6 cm) (±) to default cut (±8 cm) are shown. This plot was obtain in the highest IR (>5.5kHz, highest statistics).

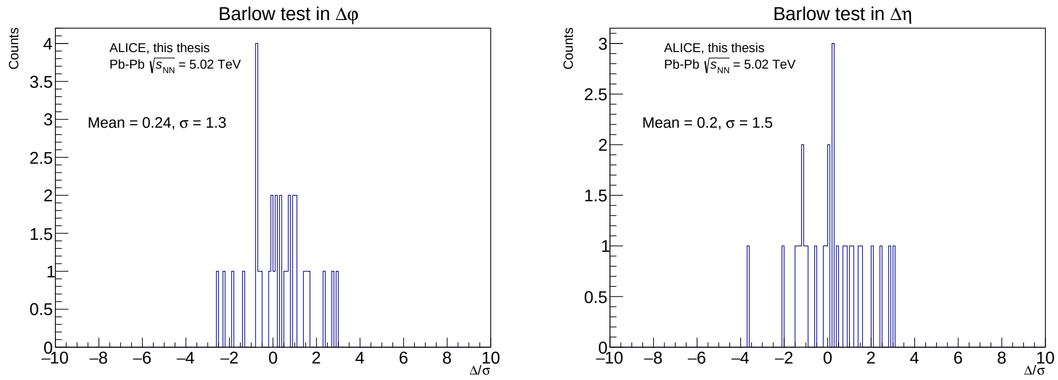

Figure 5.8: Barlow criteria distribution of different $z_{\rm vertex}$ ranges in the $\Delta\varphi$ (left) and $\Delta\eta$ (right). The mean and sigma of the histogram are shown on the left side of the panels.

cuts, a $p_{\rm T}$ dependent cut value in xy, and 2.0 in z. In the case of track bit 16, it has the identical DCA cuts with the default (768). However, two TPC quality cuts regarding the χ^2 value for global track and constrained track and the maximum shared fraction of TPC clusters are not applied. These two cuts are used for the rejection of secondary particles, so the tracks with bit 16 contain more secondary particles than the default track. On the other hand, the tracks with bit 96 include less secondary particles than the default due to the tighter DCA cuts. In this work, hybrid tracks were used to avoid a hole due to the missing channels in the SPD and obtain uniform tracks in φ, as explained in Sec. 4.3.1. Track bit 96 requires a signal on the first layer in the SDD, instead of the SPD.

Comparisons of correlation functions and Barlow test results are shown in Figs. 5.11 and 5.12. The results show systematic differences depending on the track bits. In the Barlow tests, the mean and standard deviation were not passed by our cuts. Therefore, the track bit uncertainty was taken into account for one of the final systematic uncertainties. Bit 96 and 16 show apparent upward/downward deviation. Therefore, we took both upward and downward uncertainties and applied them individually to the correlation function.

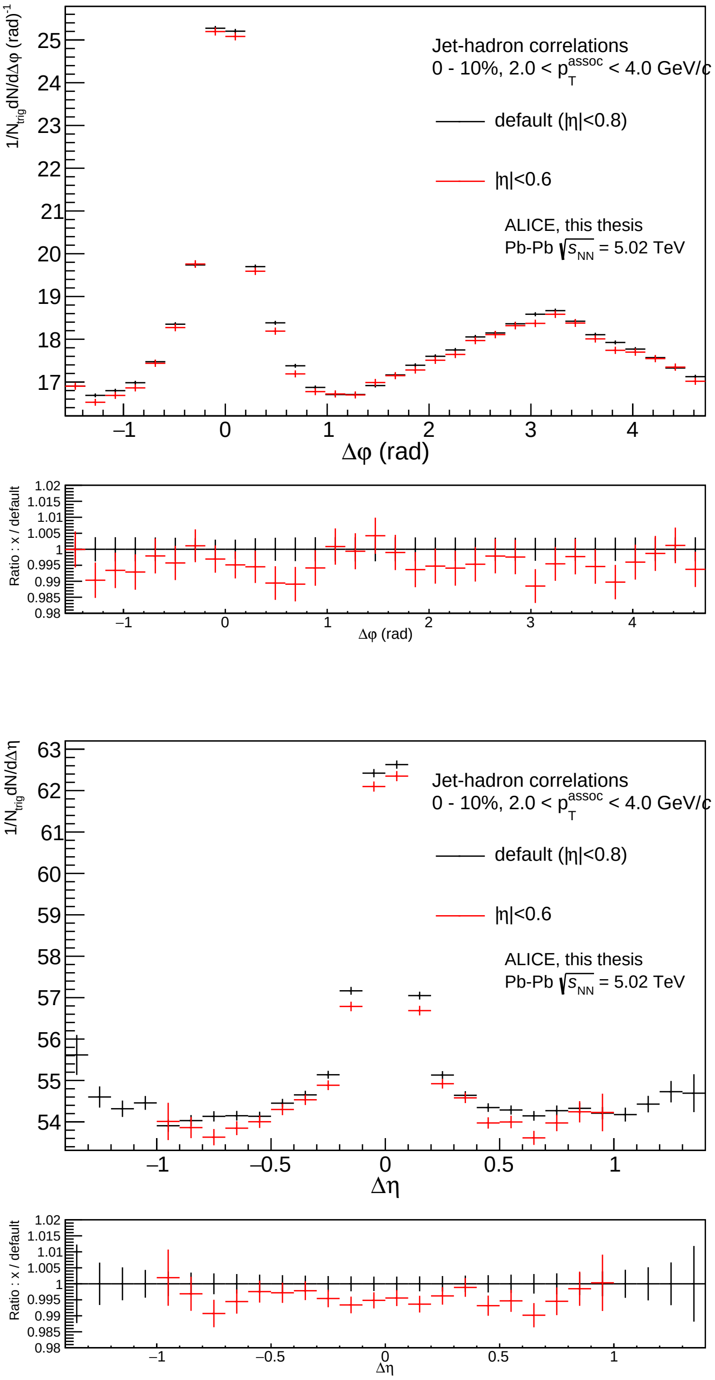

Figure 5.9: Comparison of jet-hadron correlations between different η_{track} ranges. Correlation function in $\Delta\varphi$ (top) and $\Delta\eta$ (bottom) and the ratio (bottom pad of each plot) of different η_{track} cut (±0.6) ($\pm$) to default cut (±0.8) are shown. This result is obtained in the full statistics of LHC15o.

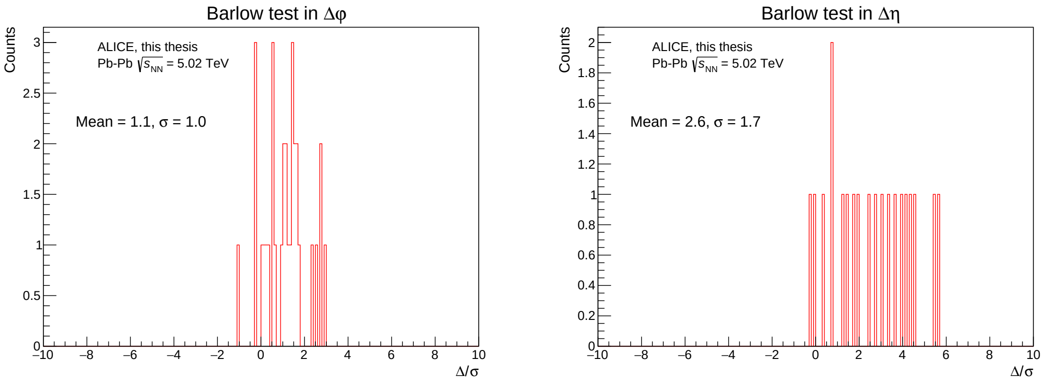

Figure 5.10: Barlow criteria distribution of different η_{track} ranges in the $\Delta\varphi$ (left) and $\Delta\eta$ (right). The mean and sigma of the histogram are shown on the left side of the panels.

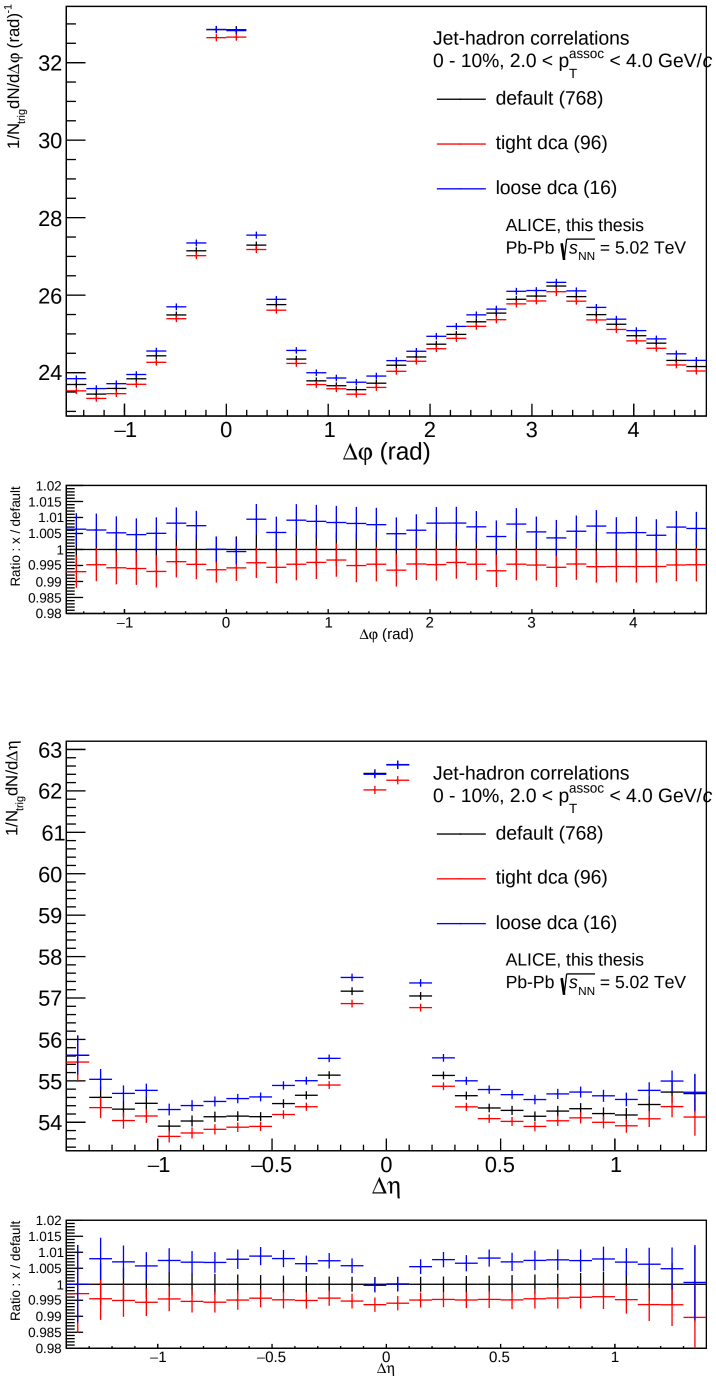

Figure 5.11: Comparison of jet-hadron correlations between different track bits. Correlation function in $\Delta\varphi$ (top) and $\Delta\eta$ (bottom) and the ratio (bottom pad of each plot) of different track bits (bit 16 and bit 96) to the default (bit 786, hybrid track) are shown. This result is obtained in the full statistics of LHC15o.

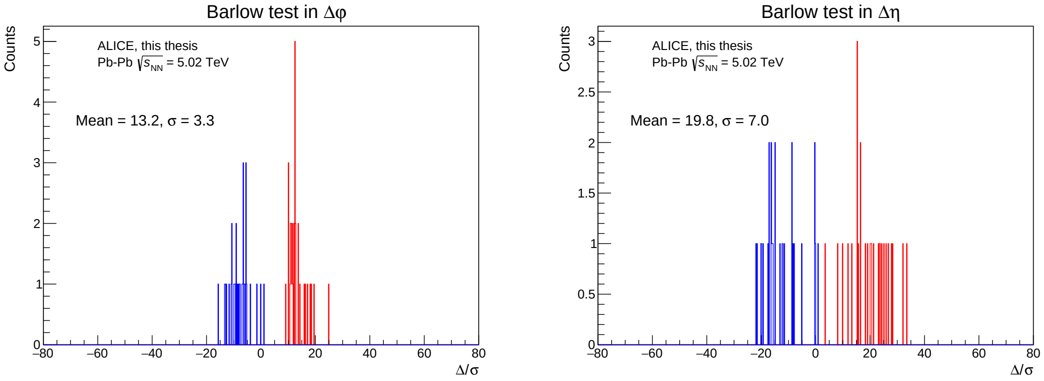

Figure 5.12: Barlow criteria distribution of different track bits in the $\Delta\varphi$ (left) and $\Delta\eta$ (right). The red and blue histogram correspond to the Barlow criteria distribution for track bit 96 and for track bit 16, respectively. The mean and sigma of the inclusive result are shown on the left side of the panels.

Hybrid tracks (bit 768 = 256 + 512)	**Standard tracks with tight DCA cut (bit 96 = 32 + 64)**
SetMinNCrossedRowsTPC(70)	SetMinNCrossedRowsTPC(70)
SetMinRatioCrossedRowsOverFindableClustersTPC(0.8)	SetMinRatioCrossedRowsOverFindableClustersTPC(0.8)
SetMaxChi2PerClusterTPC(4)	SetMaxChi2PerClusterTPC(4)
SetAcceptKinkDaughters(kFALSE)	SetAcceptKinkDaughters(kFALSE)
SetRequireTPCRefit(kTRUE)	SetRequireTPCRefit(kTRUE)
SetRequireITSRefit(kTRUE)	SetRequireITSRefit(kTRUE)
SetClusterRequirementITS(kSPD, kAny)	SetClusterRequirementITS(kSPD, kAny)
SetRequireSigmaToVertex(kFALSE)	SetRequireSigmaToVertex(kFALSE)
SetMaxChi2PerClusterITS(36)	SetMaxChi2PerClusterITS(36)
SetMaxChi2TPCConstrainedGlobal(36)	SetMaxChi2TPCConstrainedGlobal(36)
SetMaxDCAToVertexXY(2.4)	**SetMaxDCAToVertexXYPtDep("0.0105+0.035/pt^1.1")**
SetMaxDCAToVertexZ(3.2)	**SetMaxDCAToVertexZ(2)**
SetDCAToVertex2D(kTRUE)	**SetDCAToVertex2D(kFALSE)**
SetMaxFractionSharedTPCClusters(0.4)	**for 64: SetClusterRequirementITS(kSPD, kNone)**
for 512: SetClusterRequirementITS(kSPD, kOff)	**for 64: SetClusterRequirementITS(kSDD, kFirst)**

Table 5.1: List of applied cuts in different track bits 768 and 96.
Main differences between 768 and 96 are in DCA cuts (loose vs. tight). Bit 16 has the same cuts as Hybrid tracks, but only has different TPC track quality cuts. For Bit 16, only these two cuts are removed: SetMaxChi2TPCConstrainedGlobal(36), SetMaxFractionSharedTPCClusters(0.4).

Tracking efficiency uncertainty is related to the difference between data and MC. We do not know to which extent the MC simulation equals/differs from the real experiment, therefore the efficiency calculation in MC can be a potential source of a systematic uncertainty. To obtain this uncertainty, comprehensive studies are required in data and MC, including investigation of tracking processes. We used an uncertainty value in the published paper [156], which is about 4% at $p_{\mathrm{T}} = 2$ to 5 GeV/c. This uncertainty includes the effect arising from matching efficiency between TPC and ITS.

While analyzing results depending on different IR sets separately (see Table 4.1), we observed a discrepancy from IR sets which is not entirely removed after all correction procedures. In the end, we decided to include such deviation as a systematic uncertainty coming from the IR sets. It was defined based on the differences of the integral of $\Delta\eta$ between the IR sets, as 1% in jet-hadron and 2% in jet-proton correlation.

5.4.1 Summary of systematic uncertainty

The total systematic uncertainty is shown in Figs. 5.14 and 5.15. It is calculated as a quadrature sum of individual uncertainties. The uncertainty of the proton correlation is greater than that of the hadron one in both $\Delta\varphi$ and $\Delta\eta$, because of less statistics for protons.

Figures. 5.16 and 5.17 show the correlation functions including the systematic uncertainty. We divided the uncertainty into the correlated uncertainty (grey) and the un-correlated uncertainty (red) and plotted them separately. In the case of the uncorrelated one, it affects the signal bin-by-bin, and thus it should be considered when we look into the shape of the correlation function. On the other hand, the correlated uncertainty is a constant shift of the correlation function. It involves a change of the magnitude of the correlation function but not a change of shape. For that reason, the correlated uncertainty is indicated as a red box at the edge.

The jet-hadron and jet-proton correlation functions have a prominent jet peak on the near-side in $\Delta\varphi$ and on the center in $\Delta\eta$ distribution. The away-side in $\Delta\varphi$ shows a broader width than the near-side peak because it is an entangled signal consisting of away-side jet fragmentation, the flow effect, and the medium response. The $\Delta\eta$ distribution is flat beyond ± 0.4, less affected by the jet fragmentation.

5.5 Comparison of Jet-hadron and Jet-proton

The comparison between jet-hadron and jet-proton correlations was performed to search for a potential shape difference between them caused by the medium response. A modified Zero Yield At Minimum (ZYAM) method was employed to

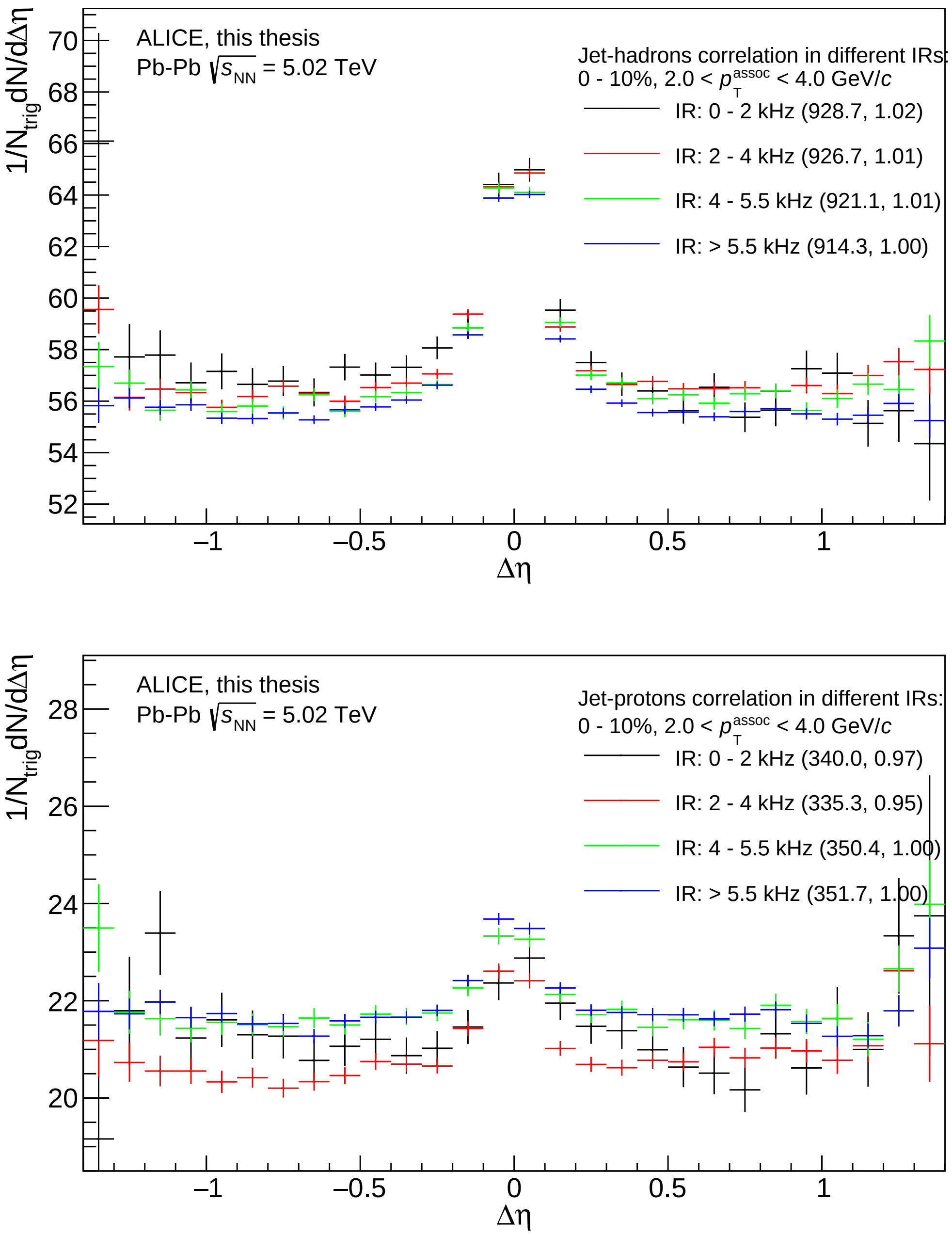

Figure 5.13: Comparison between different IR sets in jet-hadron(top), jet-proton correlation(bottom). In the legend, the two numbers inside parentheses refer the integral between -0.8 to +0.8 and the ratio of the integral of each IR to the highest IR (> 5.5kHz, the highest statistics).

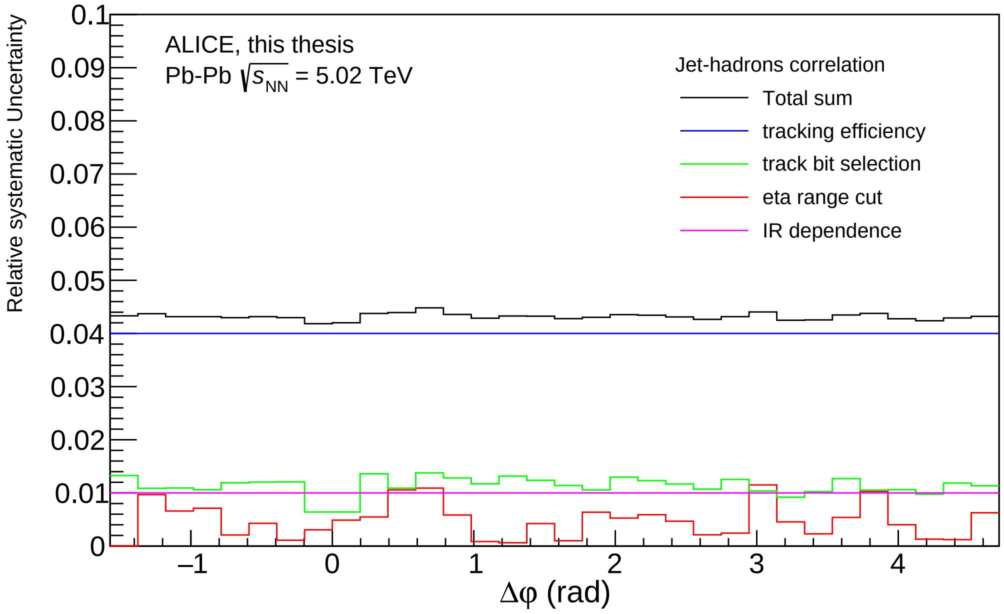

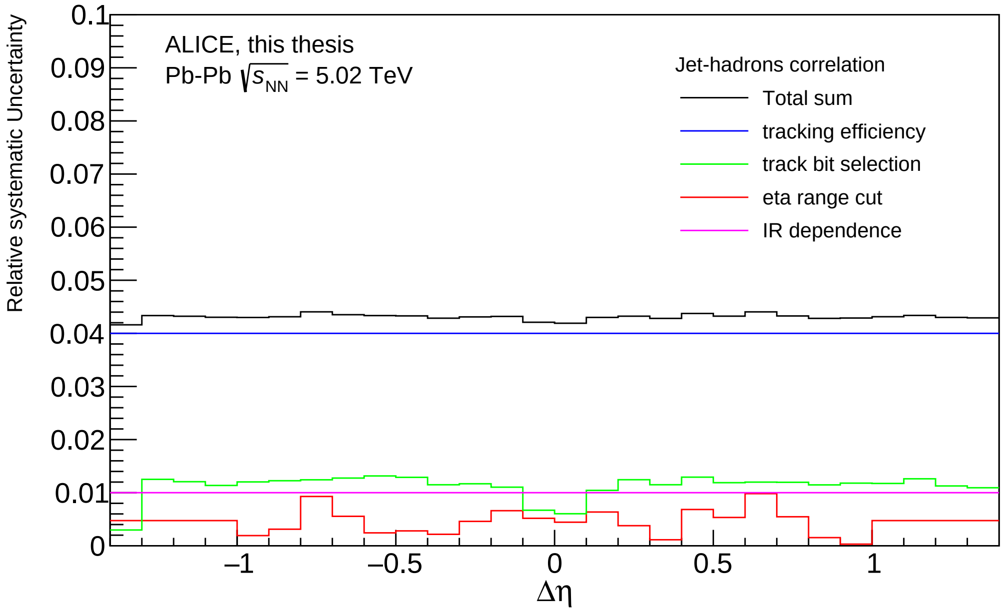

Figure 5.14: Total systematic uncertainty in the jet-hadron correlation.

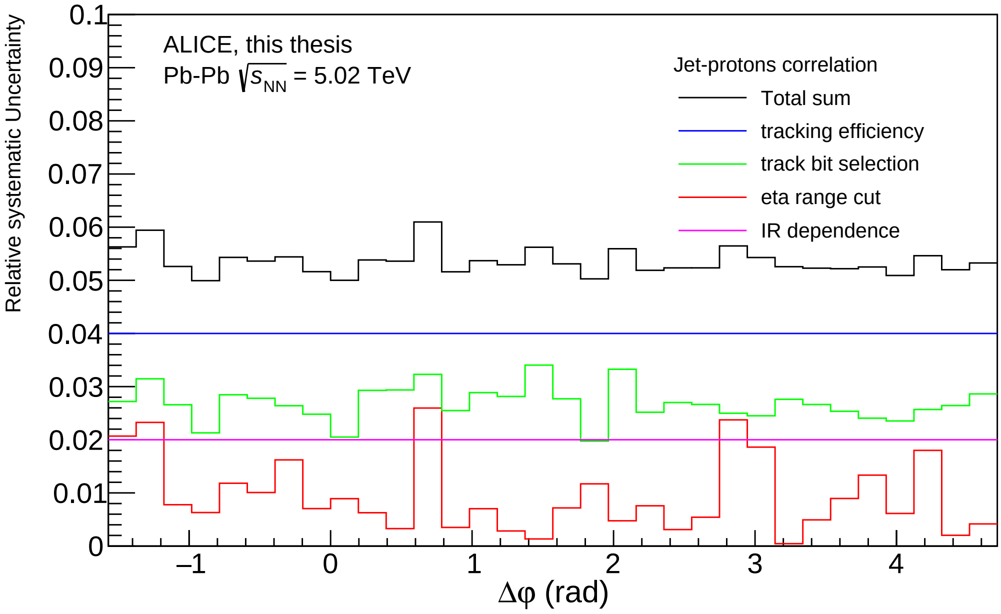

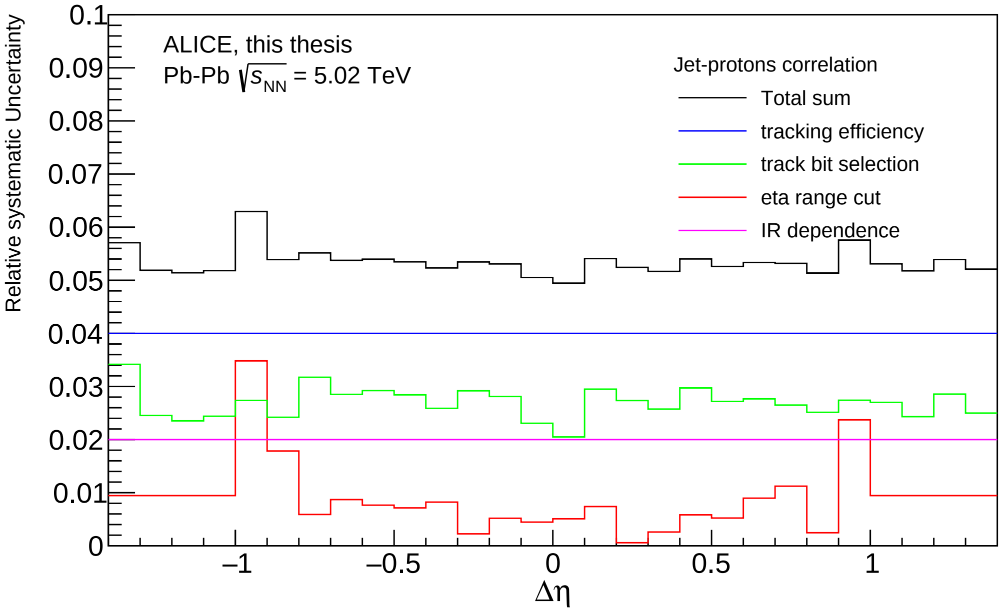

Figure 5.15: Total systematic uncertainty in the jet-proton correlation.

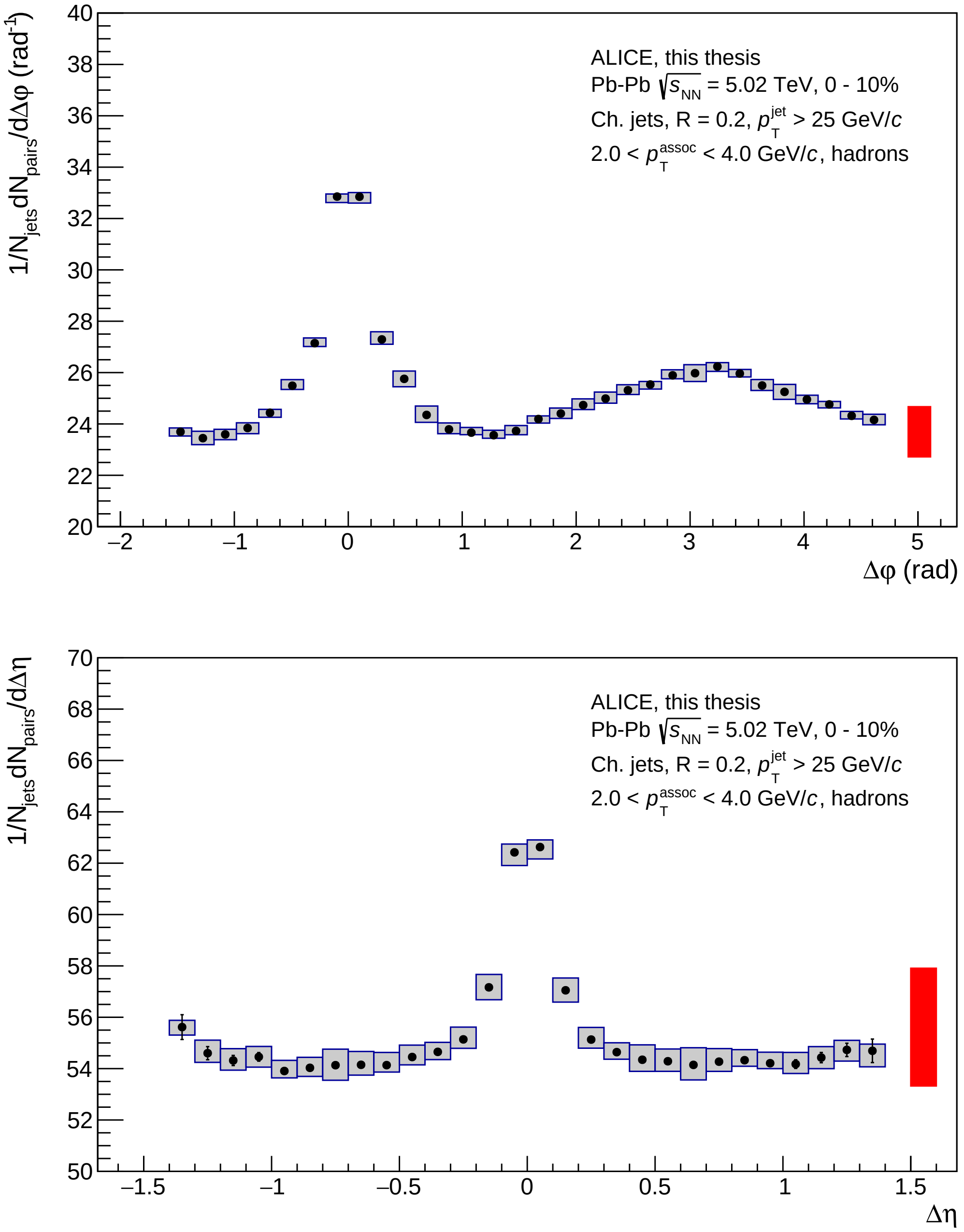

Figure 5.16: The jet-hadron correlations in $\Delta\varphi$ (upper) and $\Delta\eta$ (bottom), normalized by the number of jets. This is the full statistics of LHC15o. The statistical error and the uncorrelated systematic error are shown as a bar and a box in a given bin. The correlated systematic uncertainty is shown as a red box on the right side. Applied cuts for jets and associated hadron tracks are shown in the legend.

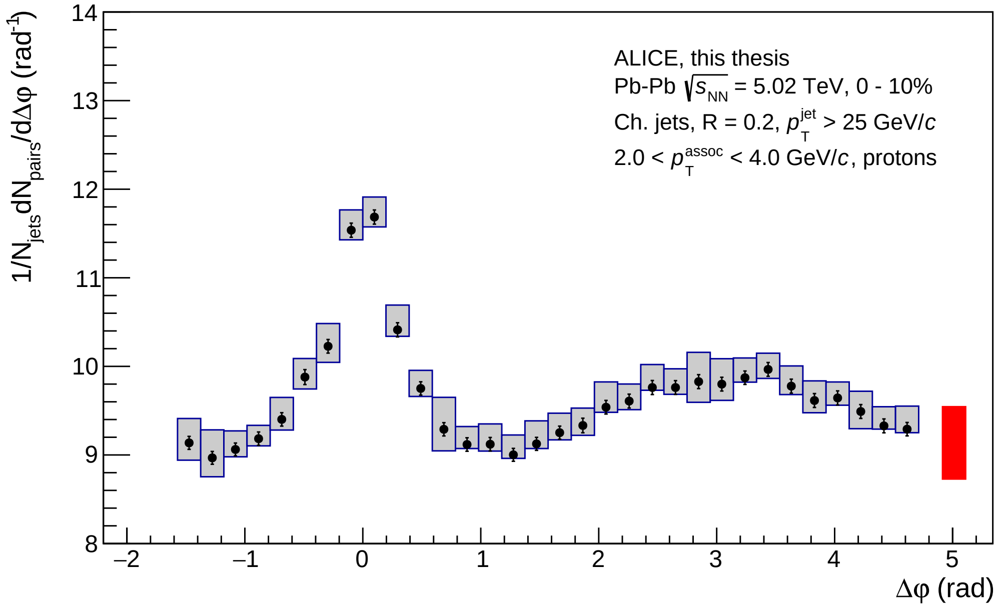

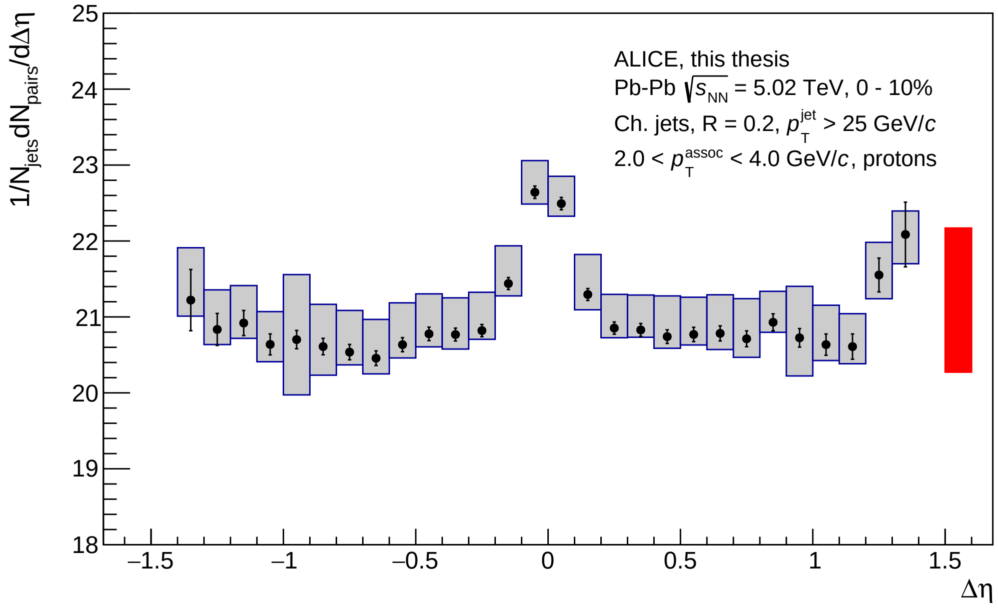

Figure 5.17: The jet-proton correlations in $\Delta\varphi$ (upper) and $\Delta\eta$ (bottom), normalized by the number of jets. This is the full statistics of LHC15o. The statistical error and the uncorrelated systematic error are shown as a bar and a box in a given bin. The correlated systematic uncertainty is shown as a red box on the right side. Applied cuts for jets and associated proton tracks are shown in the legend.

	$\Delta\eta$
Hadron	0.128 ± 0.031 (sys) ± 0.001 (stat)
Proton	0.108 ± 0.054 (sys) ± 0.003 (stat)
	Near side ($\Delta\varphi$)
Hadron	0.275 ± 0.019 (sys) ± 0.002 (stat)
Proton	0.285 ± 0.028 (sys) ± 0.006 (stat)
	Away side ($\Delta\varphi$)
Hadron	0.757 ± 0.034 (sys) ± 0.014 (stat)
Proton	0.730 ± 0.047 (sys) ± 0.039 (stat)

Table 5.2: Widths from Gaussian fits to the jet-hadron and jet-proton correlation functions in $\Delta\eta$ and $\Delta\varphi$.

subtract the different uncorrelated baselines from both correlations. To get the background value for the subtraction, values at $\Delta\varphi = \frac{\pi}{2}$ were used. We estimated a background value by averaging values of $\Delta\varphi = \frac{\pi}{2}$ from -1 to 1 in $\Delta\eta$. Then, the estimated background value was converted to expected values in $\Delta\varphi$ and $\Delta\eta$ projections. With those values, we subtracted the baseline from our $\Delta\varphi$, $\Delta\eta$ correlation functions.

The subtracted correlation functions without any scaling are illustrated in Fig. 5.18. Due to correlation statistics, the total yield is larger in the jet-hadron correlations than in the jet-proton correlations. Table 5.2 shows widths obtained from Gaussian fits to the correlation functions. The Gaussian fits were performed in certain fit ranges to obtain stable fit results: $\Delta\eta$ is in ± 0.32, $\Delta\varphi$ for the near side in ± 1.0 and $\Delta\varphi$ for the away side between $\frac{\pi}{2}$ to $\frac{3\pi}{2}$. Within uncertainty, jet-hadron and jet-proton correlation widths do not show a difference.

The comparison with additional scaling is drawn in Fig. 5.19. The scaling was done by matching the yield of the near-side peak between the jet-hadron and the jet-proton correlations, and only the jet-proton correlation was modified. Such scaling gives an opportunity to see how the correlation functions look like where more medium responses come in.

The overall distributions look very similar to each other in both $\Delta\varphi$ and $\Delta\eta$. If Mach cone-related signals exist, in the given Mach cone emission angle from 55 to 70°, it is expected to appear around $\Delta\varphi = \pm\ 0.9 \sim 1.2$ on the near-side. And, it can be seen in $1.9 \sim 2.2$ and $4.0 \sim 4.3$ on the away-side. Some extent of deviation is observed on the away-side of $\Delta\varphi$ around 2.4 and 3.6, but it is very subtle, so that it is too difficult to draw a concrete conclusion from the results. Besides, we cannot completely ignore the remaining flow contribution in jet-hadron and jet-proton correlations. There is a possibility that the flow effect for hadrons and protons shows such deviation in the comparison. To avoid the distraction of the

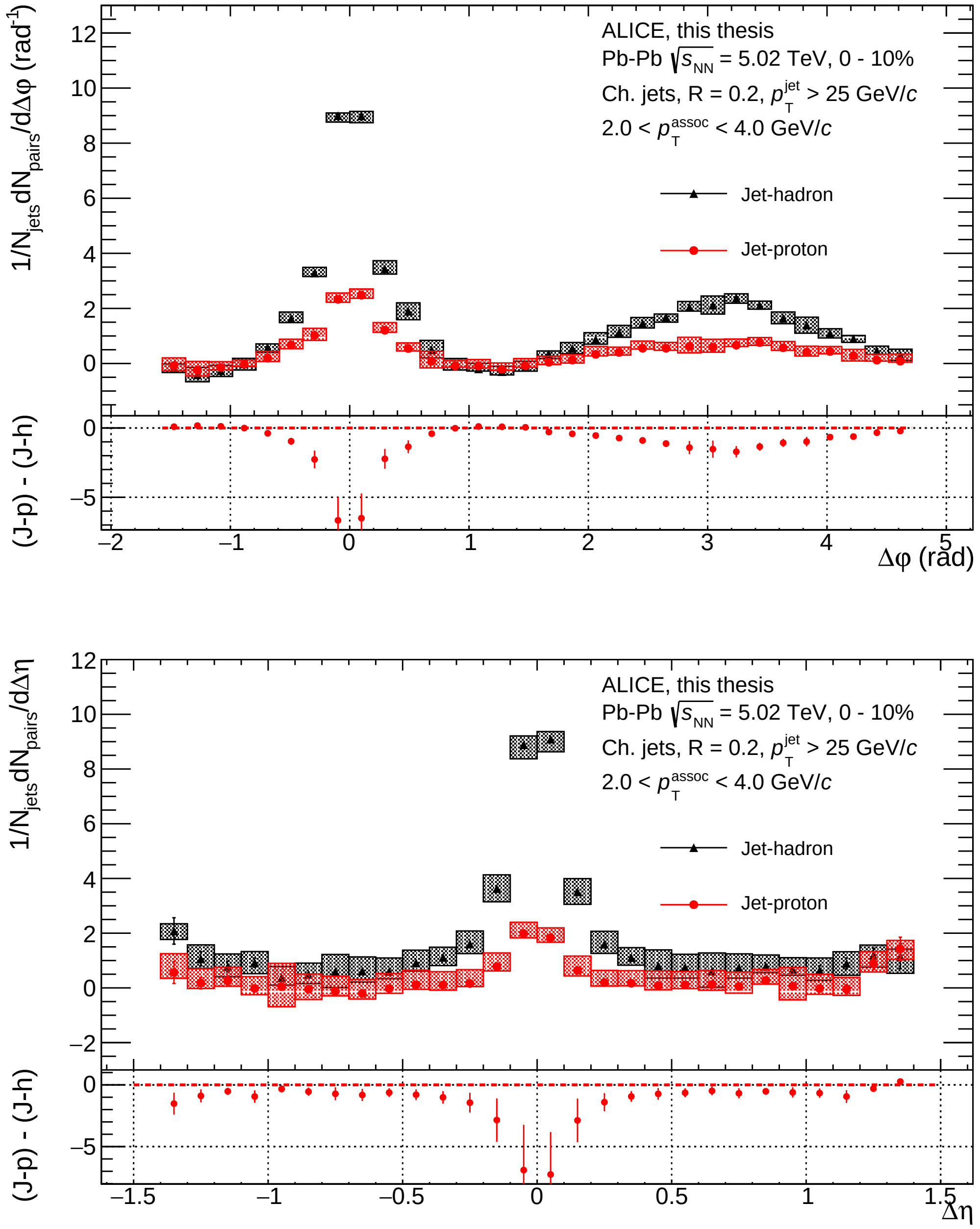

Figure 5.18: Comparison between jet-hadron and jet-proton correlation functions without scaling in the $\Delta\varphi$ (upper) and the $\Delta\eta$ (bottom). The 2D-ZYAM method was used to subtract the baseline in both correlation functions. The bottom panel shows a difference between the jet-proton correlations and the jet-hadron correlations.

flow and look for a distinctive medium signal, another new approach is needed. The following chapter discusses our new analysis method, called hadron-hadron correlations with the away-side tracks, and its results.

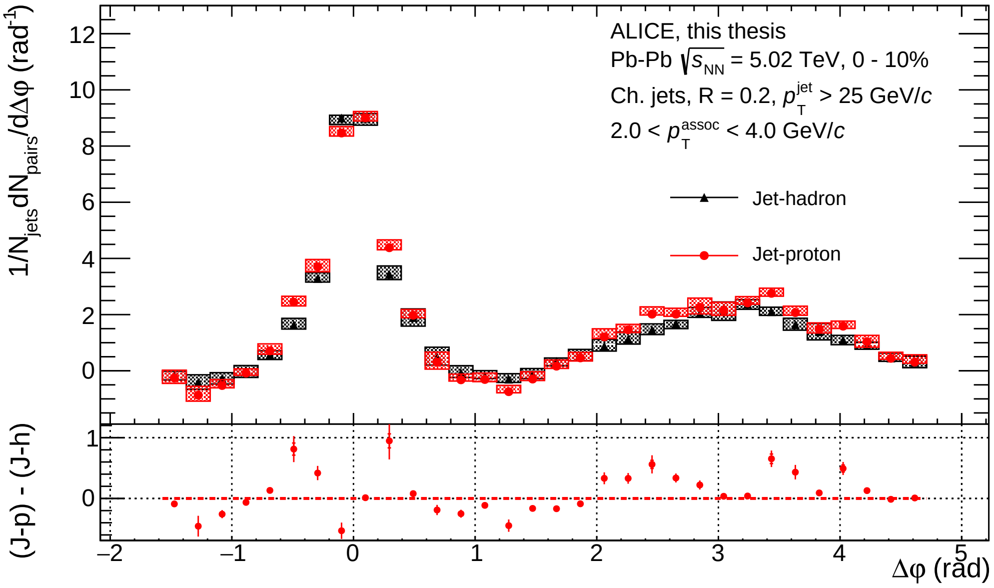

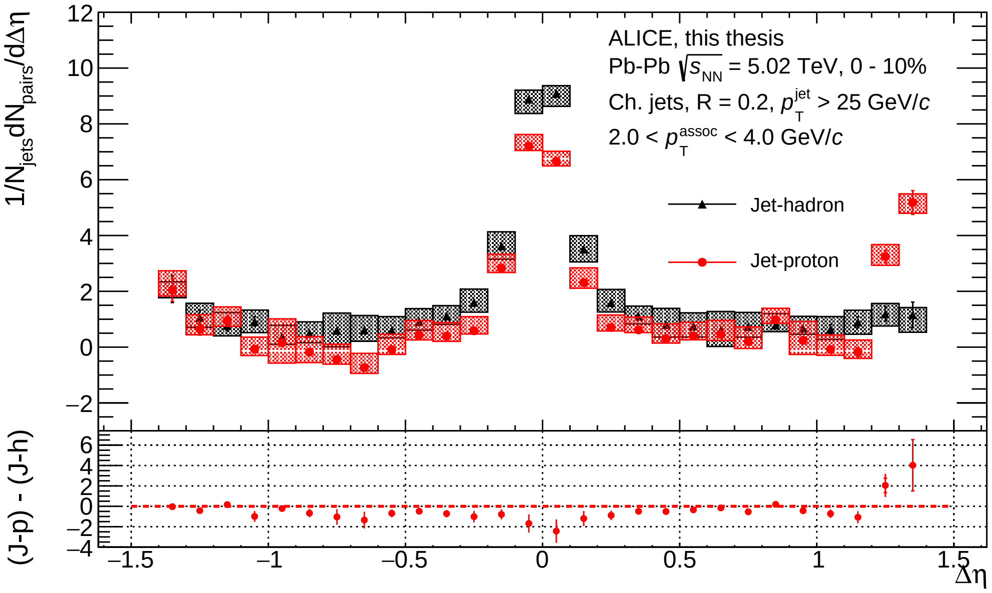

Figure 5.19: Comparison between the jet-hadron and jet-proton correlation functions with the near-side yield scaling in the $\Delta\varphi$ (upper) and the $\Delta\eta$ (bottom). The 2D-ZYAM method was used to subtract the baseline in both correlation functions. The scaling was applied to only the jet-proton correlation functions, matching the yield of the near-side peak between the jet-hadron correlations and the jet-proton correlations. The bottom panel shows a difference between the jet-proton correlations and the jet-hadron correlations.

6 Hadron-hadron correlation with away-side tracks

6.1 Introduction of the concept

As discussed in Ch. 5, Mach cone signals were not observed in the jet-hadron and jet-proton correlations. Therefore, the angular correlations between the away-side tracks were considered, the *hadron-hadron correlations* with the away-side tracks. For the hadron-hadron correlation analysis, the previous jet-hadron correlations provide the geometric information about a trigger jet and associated particles. In the jet-hadron correlations in $\Delta\varphi$, the axis of the trigger jet is placed at $\Delta\varphi = 0$ and the fragmented particles from the trigger jet are present on the near-side. On the away-side, the opposite jet can be found at $\Delta\varphi = \pi$ due to the back-to-back structure on the azimuthal angle. Since the particles related to the recoil jet are found on the away-side, investigating hadron-hadron correlations between the away-side tracks allows us to understand signals induced around the opposite-side jet.

One of the advantages of using tracks around the away-side jets is that these jets are less biased than the trigger jets. Since the trigger jets are clustered via the jet reconstruction algorithm and selected through transverse momentum cuts, they are biased towards the highly energetic jets carrying high transverse momenta that fragment in a narrow cone. Considering that jets lose their energy via interaction with the QGP medium, the trigger jets should have interacted less with the QGP medium since they are highly energetic. Since the Mach cone is a medium response induced by jets, it can be better observed with the away-side jets which should have interacted more with the QGP.

Therefore, one can imagine that ring-shaped Mach cone signals could be found around each away-side jet, distributed along the $\Delta\eta$, as shown in Fig. 6.1a. However, since the away-side jet does not have a fixed $\Delta\eta$ with respect to the trigger jet, in the jet-hadron correlations the possible Mach-cone structures would be smeared together on the away side, as illustrated in Fig. 6.1a. Since the hadron-hadron correlations on the away side is calculated angular difference between only the away side tracks, the hadron-hadron correlations will localize the away-side jets around $(\Delta\varphi,\ \Delta\eta) = (0,\ 0)$, as shown in Fig. 6.1b. Moreover, since flow effects are flat in η, the $\Delta\eta$ distribution of the hadron-hadron correlation with the away-side tracks was investigated to exclude flow effects in the correlation function and to search for the Mach-cone signal around the away-side jets. So, based on this physics motivation, we first studied the hadron-hadron correlations in a toy MC simulation to test our expectations.

6.2 Toy model simulation

For the toy model simulation, three types of particles were simulated, including the background particles (called bulk particles) which exhibit flow, the jet particles, and the Mach-cone particles.

Since the event plane in every event varies according to the collision geometry, the event plane in the simulation is randomly chosen within 0 to 2π. In order to make a realistic bulk distribution, the flow effect should be considered. The bulk particle distribution including the flow effect (v_2, the most dominant term) is defined as:

$$1 + 2v_2^{\text{bulk}} \cos(2x) \qquad 0 \leq x \leq 2\pi \tag{6.1}$$

where v_2 is 0.3 [157]. Now, the φ of the bulk particles is calculated as the sum of a random value x drawn from the bulk particle distribution and the event plane value. The η of the bulk particles is chosen as a random value within the η limit: ± 1.0. Per event, 900 bulk particles were generated. Here, the number of bulk particles was selected to match the yield of the background particles in the jet-hadron correlations.

Similarly, jet φ^{jet1} is also calculated as the sum of the event plane angle and a random number x drawn from the distribution:

$$1 + 2v_2^{\text{jet}} \cos(2x) \qquad 0 \leq x \leq 2\pi \tag{6.2}$$

where v_2^{jet} is 0.2, taken from [158]. Here, the reason why the jet has a flow term, v_2^{jet}, is that jets lose their energy depending on the path length in the QGP. Jets also show a similar anisotropic angular distribution like bulk particles.

Thanks to the back-to-back structure, φ^{jet2} of the opposite jet is simply determined by $\varphi^{\text{jet1}} + \pi$. The value η^{jet} has no constraints, so a random value from a uniform distribution ranging from -0.8 to 0.8 was picked for both jets. Based on the values (φ^{jet}, η^{jet}), 20 particles were sampled from a Gaussian distribution having a mean = φ^{jet} or η^{jet} and a σ = R (jet radius, 0.2). Here, the number of jet particles was selected based on the yield of the background-subtracted jet peak on the near side in the jet-hadron correlations.

Finally, the Mach-cone particles are generated around each jet. Based on the location of the jet (φ^{jet}, η^{jet}), the location of the Mach-cone particles were determined to have the angular difference with respect to the jet axis of the Mach-cone

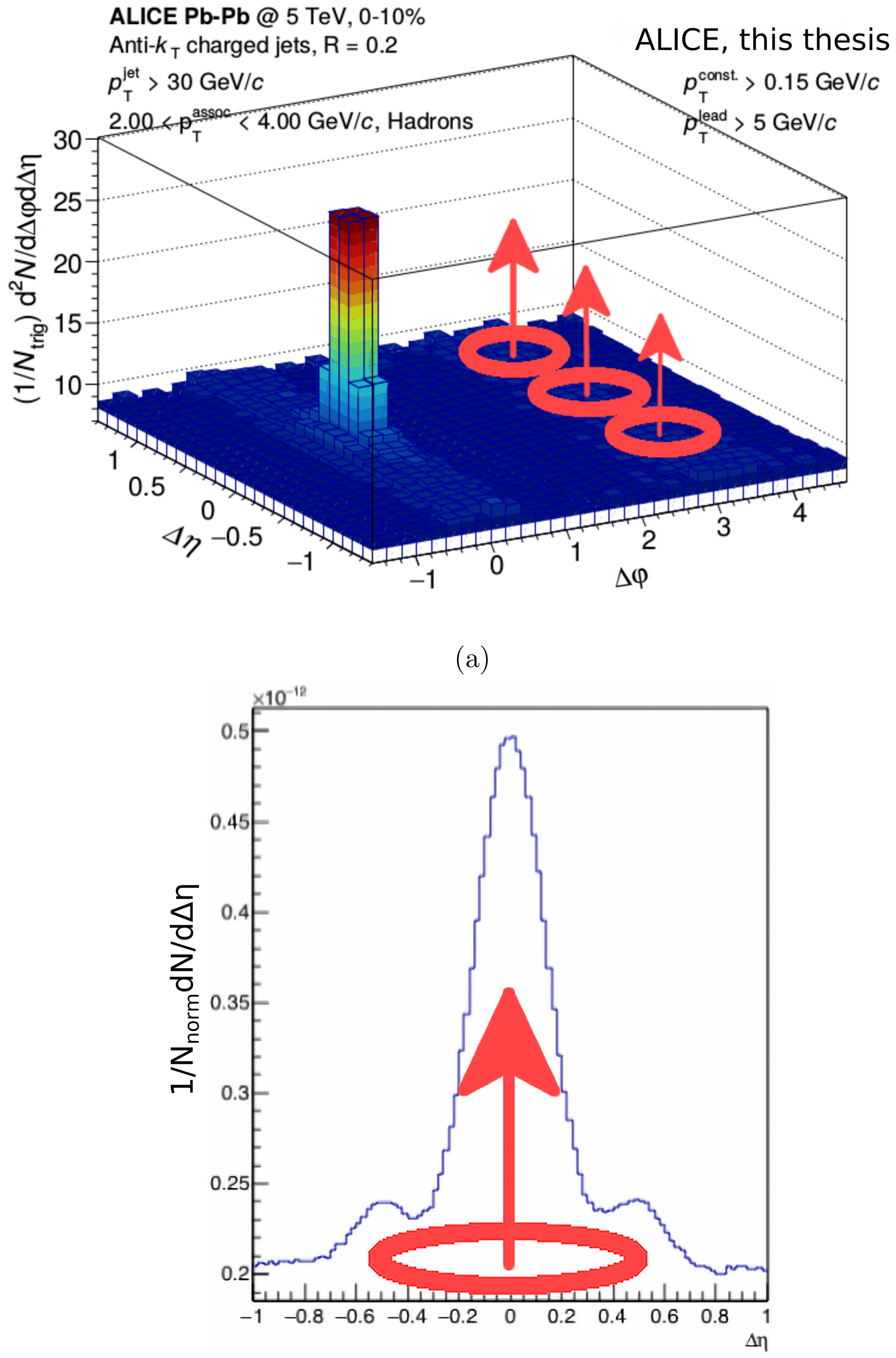

(a)

(b)

Figure 6.1: The expected Mach-cone signal in the (a) jet-hadron correlations and (b) hadron-hadron correlations with the away-side tracks. The pink arrows and rings are jets and Mach-cone signal induced by the jets in the away side ($\pi/2 < \Delta\varphi < 3\pi/2$) in the simulation.

	input parameter	**value**
particle compositions	bulk particles / event	900
	jet particles / event	20
	Mach cone particle / event	10, 2
coefficient	particle v_2	0.3
	jet v_2	0.2
jet	jet radius	0.2
Mach cone	emission angle	55.8°, 66.4°, 70°
	Gaussian smearing mean	0
	Gaussian smearing sigma	0.05

Table 6.1: Input parameters for the toy simulation.

emission angle. The theoretically predicted Mach-cone emission angles shown in Table 2.1 were used for the simulation. The location of the Mach-cone particles were smeared around the expected emission angle by a Gaussian distribution having a mean $= 0$ and a $\sigma = 0.05$. The number of the Mach-cone particles was selected as 10. For this, since there is no theoretical prediction, an arbitrary number was chosen to be half of the number of the jet particles.

The list of input parameters is available in Table 6.1.

6.2.1 Expected shape of Mach-cone signal

The Mach-cone particles show up in a circular shape, having its center at the jet position on the angular plane $((\varphi^{\mathrm{jet}}, \eta^{\mathrm{jet}}))$. The emission angle decides the radius of the circle. Since pseudorapidity (η), instead of the polar angle (θ), is often used for convenience in measurements as explained in Sec. 3.2, the correlation analysis was done in the $\varphi - \eta$ plane, not in the $\varphi - \theta$ plane. Such difference involves the change of the shape of the Mach-cone signal. Therefore, the Mach-cone signal were projected to the $\varphi - \eta$ plane, according to the relation between η and θ:

$$\eta = -\ln(\tan(\frac{\theta}{2})) \tag{6.3}$$

Figure 6.2a shows a simple example of the Mach-cone signal when the initial jet η^{jet} equals to 0 (corresponding to $\theta = 90°$). If the jet is at the origin of the frame, the Mach-cone signal appear in a circular shape with the radius equals to the emission angle ($\theta_{\mathrm{emi}} = 70° \simeq 1.2$ rad) in the φ-θ plane. When the signals are projected to the φ-η plane, the shape changes to an elliptical shape having a larger radius along the η axis, as shown in Fig. 6.2b.

The shape becomes asymmetric when η^{jet} of the initial jet is non-zero. Figure 6.3

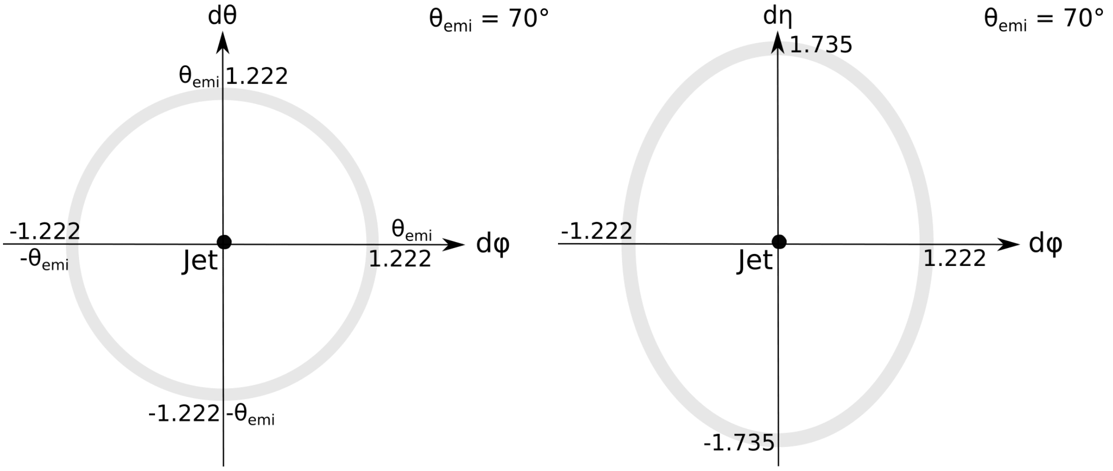

(a) (b)

Figure 6.2: Mach cone signal in (a) φ-θ and (b) φ-η planes, when $\eta_{\text{jet}} = 0$.

shows an example when jet η_{jet} equals to 0.3 (corresponding to $\theta = 73°$). The Mach-cone signal appear from 143° (θ_{emi} + θ) to 3° (θ_{emi} - θ) along the θ axis. When these signals are projected on the $\varphi - \eta$ plane, it shows an asymmetric elliptical shape, as shown in Fig. 6.3.

6.3 Results

Several different Mach-cone signal depending on the η of jets were implemented in the toy simulation. The analysis procedures were almost the same as the analysis of the data described in Ch. 5. From Figs. 6.4 to 6.7 show the basic performance results in the toy simulation step-by-step. (Note that the following toy simulation results show the case where Mach cone emission angle $= 70°$.)

Figure 6.4 shows the (a) jet-hadron correlations for the same events, (b) for the mixed events. The same event distribution in Fig. 6.4a was normalized with the number of jets and the mixed event was normalized to be equal to 1 on the plateau region at the center as shown in Fig. 6.4b. The acceptance-corrected correlation functions were obtained by dividing the mixed event distribution into the same event distribution, as shown in Fig. 6.5. As observed in the jet-hadron correlations in data, the jet-hadron correlations in the toy simulation in Fig. 6.5 show the similar distribution of $\Delta\varphi$ and $\Delta\eta$. The sharp jet peak exists on the near side and the low peak on the away side is extended along the $\Delta\eta$ axis. The result of the toy simulation shows a clear the Mach-cone signal in the jet-hadron correlations, shown as a ring around the near-side jet peak. However, such Mach-cone signal was not observed in the real data. That is because the number of Mach-cone particles

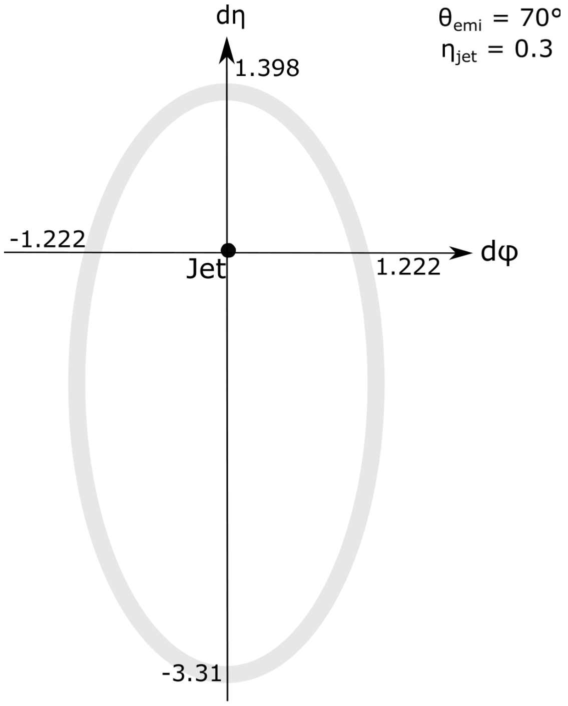

Figure 6.3: Mach cone signal in φ-η plane, when $\eta_{\text{jet}} \neq 0$.

was defined to 10 in the toy simulation, possibly larger than the real number of Mach-cone particles that can be generated in the experiment. Also, since in the real data, the near-side jet, as a trigger jet, is expected to interact less with the QGP medium, the Mach-cone signal on the near side can be hardly seen in the experiment.

Figure 6.6 shows the (a) $\Delta\varphi$ projections and the (b) $\Delta\eta$ projections from the jet-hadron correlations. The blue and red colored points represent different projection ranges along the $\Delta\varphi$ and $\Delta\eta$ axes. For the $\Delta\varphi$ distribution in Fig. 6.6a, the blue and red points show the projection from $|\Delta\eta| < 1$ and $1 < |\Delta\eta| < 1.8$, respectively. Due to the different projection ranges, the blue plot has a clear near-side peak at $\Delta\varphi = 0$, but the red plot has only a wide bump from the flow effect of the bulk particles. The peak on the away side is the same for both distributions, since the away-side jet is uniformly distributed along the $\Delta\eta$ axis. In Fig. 6.6a, a few points pop up near $\Delta\varphi = \pm\ 1.2$ and $\pi \pm 1.2$, which are the Mach-cone signals from the simulation. In Fig. 6.6b, the blue and red points show the $\Delta\eta$ distribution projected from $|\Delta\varphi| < \pi/2$ (near side) and $\pi/2 < |\Delta\varphi|$ (away side), respectively. The blue plot has a clear near-side peak at $\Delta\eta = 0$ and the Mach-cone signal near $\Delta\eta = \pm\ 1.4$, but the red plot has a flat distribution in the whole $\Delta\eta$ range. Based on the result of the jet-hadron correlations, the away-side tracks were chosen

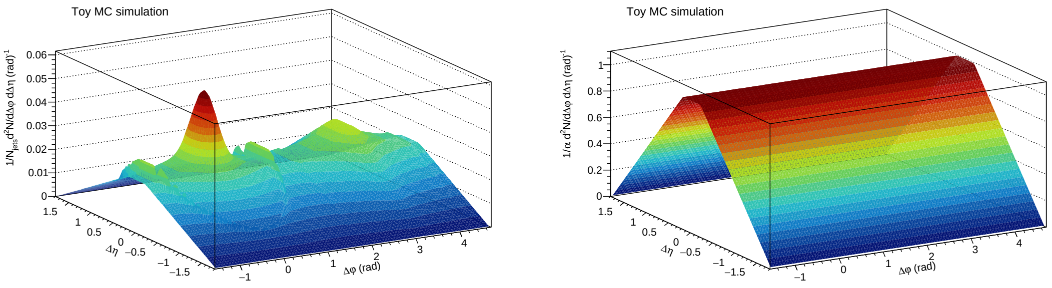

(a) (b)

Figure 6.4: Toy simulation result: the jet-hadron correlations in the (a) same events and (b) mixed events.

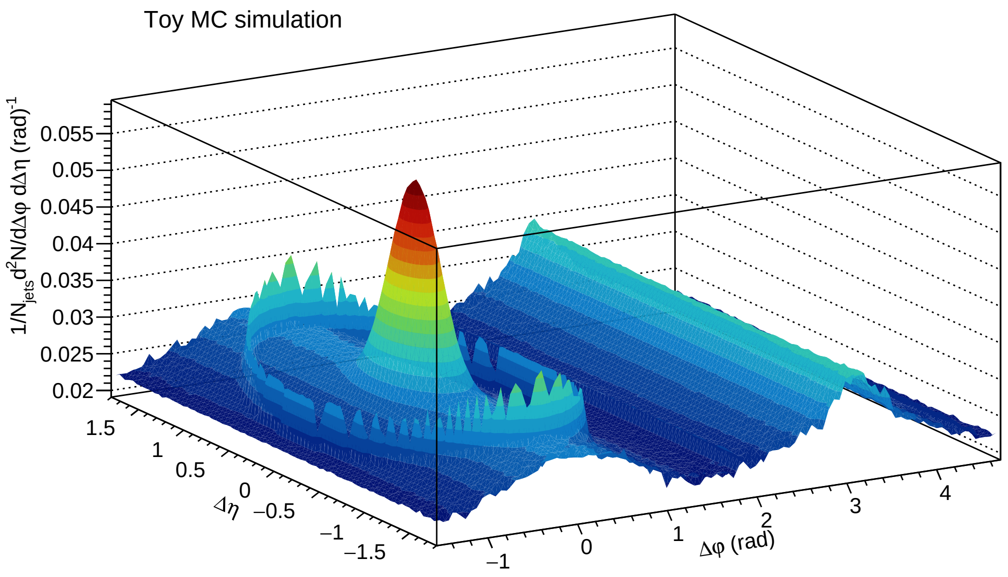

Figure 6.5: Toy simulation result: the acceptance corrected jet-hadron correlations.

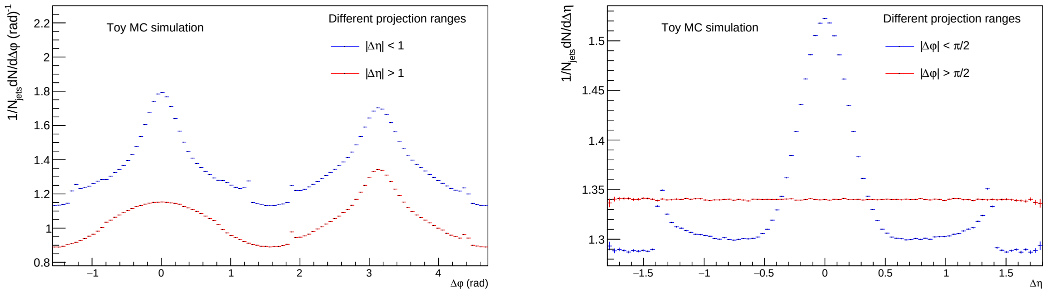

(a) (b)

Figure 6.6: Toy simulation result: the (a) $\Delta\varphi$ projection and the (b) $\Delta\eta$ projection of jet-hadron correlations. Different colored points are different projection ranges, as shown in the legend.

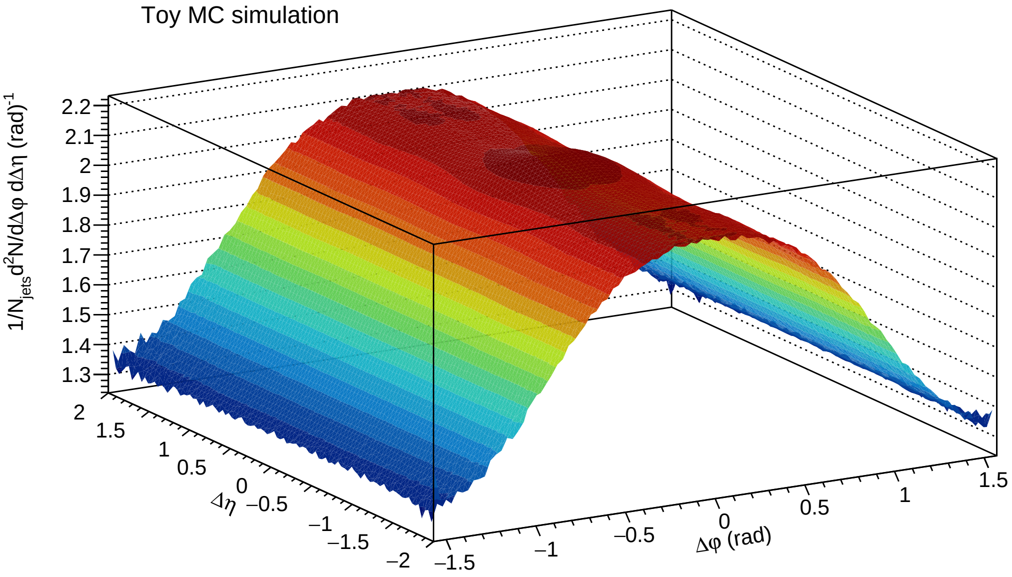

Figure 6.7: Toy simulation result: the hadron-hadron correlation with only away-side tracks, which are chosen in the given range of the jet-hadron correlations, $\pi - \frac{\pi}{4} < \Delta\varphi < \pi + \frac{\pi}{4}$.

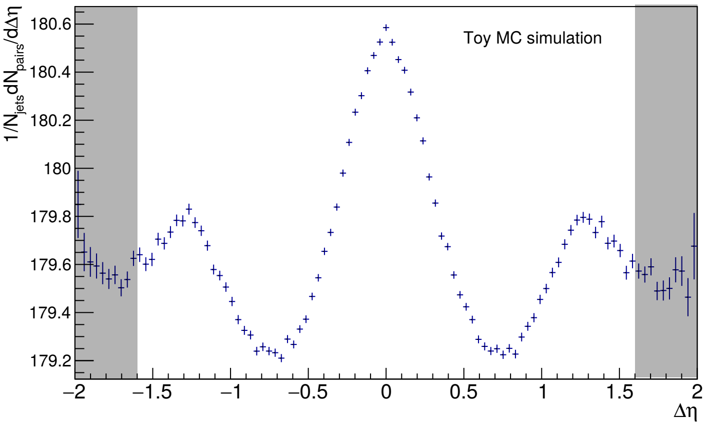

Figure 6.8: Toy simulation result: the hadron-hadron correlation with the away-side tracks in $\Delta\eta$. This result is normalized by the number of near-side jets. Both gray regions were ignored to match the same η range with the result from the data.

for the hadron-hadron correlations, in other words, $\pi - \frac{\pi}{4} < \Delta\varphi < \pi + \frac{\pi}{4}$, which corresponds to $\pm\frac{\pi}{4}$ at the center of the away-side peak.

Next, the hadron-hadron correlation method was validated in the toy simulation. Figure 6.7 shows the hadron-hadron correlations with the selected away-side tracks. Since this hadron-hadron correlation result was plotted on $\varphi - \eta$, the flow effect was observed along the $\Delta\varphi$ axis. However, there is no flow effect along the $\Delta\eta$ axis, as also shown in Fig. 6.8. As explained in the previous section, in the hadron-hadron analysis on the away side, the away-side jets are accumulated around $\Delta\eta = 0$ and the Mach-cone signal by each away-side jet is observed as a clear peak at $\Delta\eta = \pm 1.3$. Compared to the peak of the Mach-cone signal in the jet-hadron correlations, that of the Mach-cone signal has a wider width because it was calculated between hadrons, not between jets and hadrons.

Then, the same analysis approach was adopted in the real data. Figure 6.9 shows the hadron-hadron correlations from the real data corresponding to the simulated data in Fig. 6.8.

Since different normalization factors were used in the simulation and the data, the baseline values are different in Fig. 6.8 and 6.9. The hadron-hadron correlation from the data was normalized with the number of the tracks (only the away-side tracks involved in the hadron-hadron correlation), but the correlation from the simulation was normalized with the number of near-side jets. Despite the baseline difference, the ratio of the jet peak and the baseline is more important for the comparison of the data and the simulation. The relative height (around 1%) is

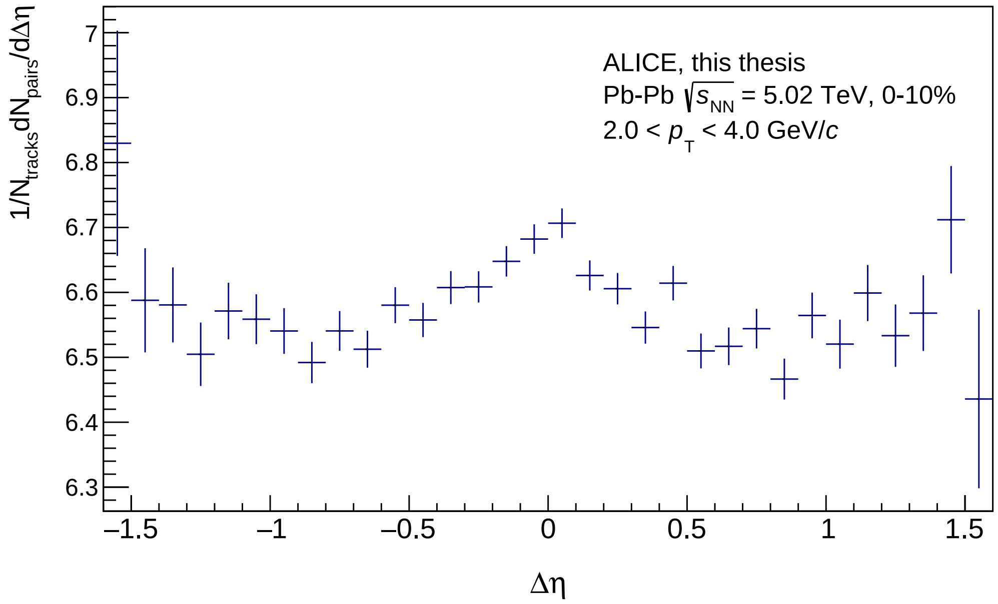

Figure 6.9: Data result: the hadron-hadron correlation with the away-side tracks in $\Delta\eta$. This result is normalized by the number of only away-side tracks which are involved in the hadron-hadron correlations.

comparable in both correlations from the data and the simulation, since the toy simulation was tuned to the data.

The sharpness of the jet peak at $\Delta\eta = 0$ in the simulation shows a difference with respect to the real data. This is because jet broadening effect was not simulated in the toy simulation. In the case of the simulation, all jet particles (20 particles) are sampled from a Gaussian distribution with $\sigma = \mathrm{R}$ (jet radius), as explained in Sec. 6.2. However, in reality, the exact angle of the generation of the jet particles is unclear. For the jet clusterization in the real data, the jet radius, R was defined as 0.2, however, there can be jet particles outside of the radius. Moreover, the toy simulation did not simulate the QGP formation. Therefore, the contributions of jet particles outside of the jet radius and the QGP medium effect make the jet peak broadened in the result of the real data. Under these circumstance, the Mach-cone signal was not observed in the hadron-hadron correlation from the real data.

As a way to confirm whether the two peaks at $\Delta\eta = \pm\ 1.3$ are created by the Mach-cone particles, the differential $\Delta\eta$ distributions projected from different $\Delta\varphi$ ranges was designed. To understand the differential $\Delta\eta$ distribution based on different $\Delta\varphi$ ranges, looking into the Mach-cone signal distribution in the jet-hadron correlations is helpful. Figure 6.10 shows the jet-hadron correlations from the toy model in $\Delta\varphi$ and $\Delta\eta$ on the near side. The center point $(\Delta\varphi, \Delta\eta) = (0, 0)$ is the jet peak on the near side and the light yellow ring shows the Mach-cone particles induced around the jets. Different colored dots indicate the position of the Mach-cone signal depending on different $\Delta\varphi$ ranges. When the $\Delta\eta$ projection is taken at the location of the red dot, it has the largest distance between the jet peak ($\Delta\eta = 0$) and the Mach-cone signal (red dot). On the other hand, when making the $\Delta\eta$ projection from the area nearby the blue dot, the distance between jet and the Mach-cone signal (blue dot) is shorter than the case of the red. The intermediate range, shown as the green dot, is the middle between the red and the blue. The colored vertical lines in Fig. 6.10 indicate 6 different $\Delta\varphi$ ranges, having a same length in $\Delta\varphi$, to make differential $\Delta\eta$ plots. Since, the negative and positive side result in the $\Delta\eta$ projection are symmetric in a given $\Delta\varphi$ range from the center at $\Delta\varphi = 0$, both negative and positive results can be merged after the $\Delta\eta$ projection.

The same differential comparison is also possible with the hadron-hadron correlations.

Figure 6.11 shows the hadron-hadron correlations on $\Delta\eta$ in the simulation, presenting three differently colored distributions from different $\Delta\varphi$ ranges, including the red plot which shows the center range, the green plot shows the intermediate range, and the blue plot shows the edge-side ranges. To place the three distribution on a similar baseline, normalization was done with an arbitrary number. As shown in Fig. 6.11, the Mach-cone peak locations depend on the different $\Delta\varphi$ ranges, for

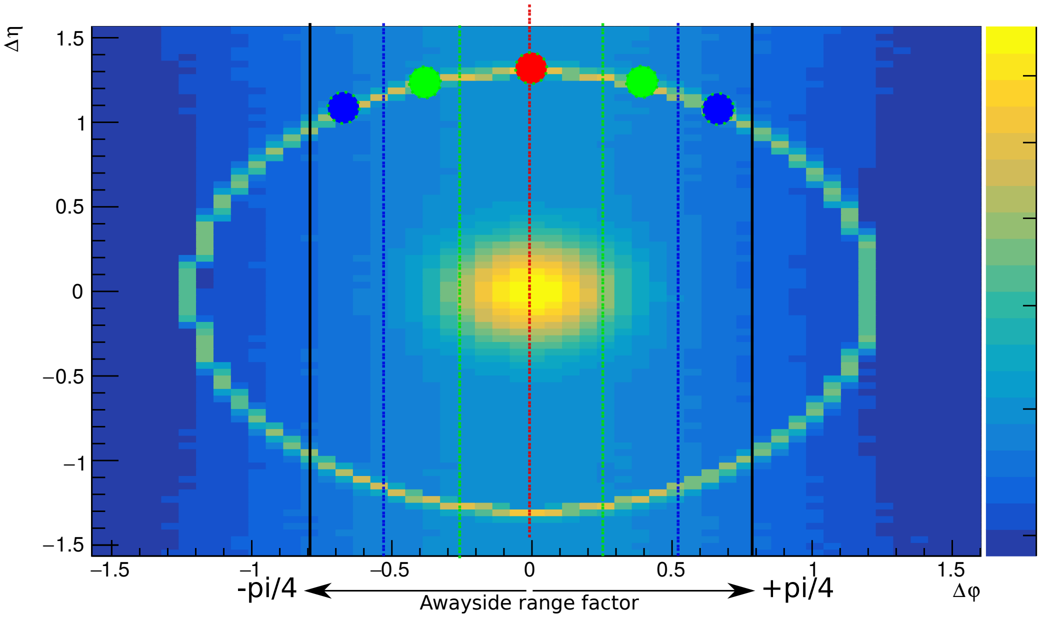

Figure 6.10: Toy simulation result: the jet-hadron correlations in $\Delta\varphi$ and $\Delta\eta$ on the near side. Different colored dots indicate the position of the Mach-cone signal depending on different $\Delta\varphi$ ranges.

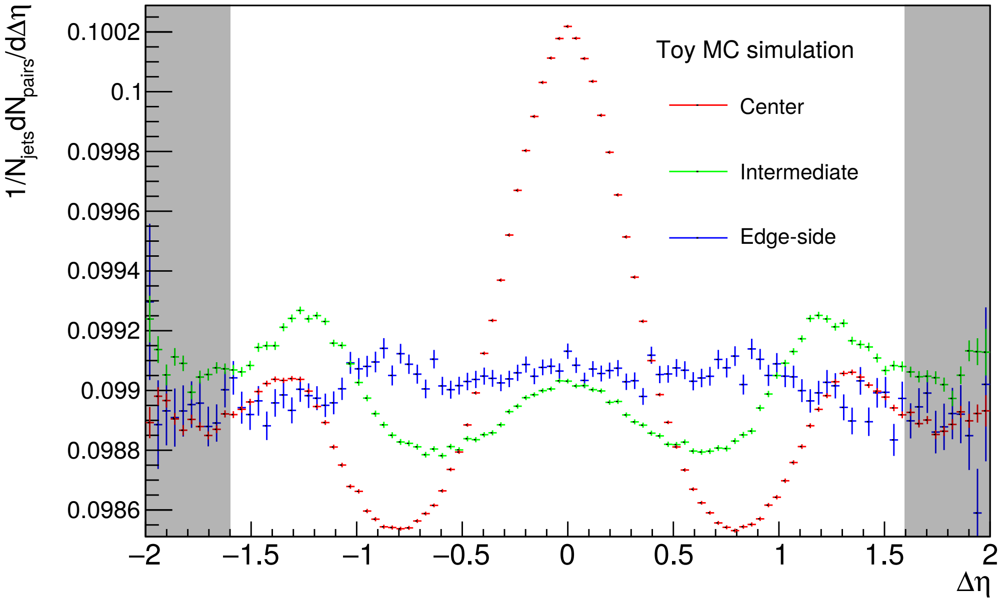

Figure 6.11: Toy simulation result: the differential hadron-hadron correlations according to different $\Delta\varphi$ projection ranges. Both gray regions were ignored to match the same η range with the result from the data.

example, the peak location is the closest to the origin of the plot in case of the edge-side ranges, whereas the farthest from the origin in case of the center range.

Figure 6.13 shows the differential $\Delta\eta$ distributions from the different $\Delta\varphi$ ranges from the data corresponding to the simulated data in Fig. 6.11. In the differential $\Delta\eta$ distribution from the data, no peak is observed within statistical fluctuations.

The Mach-cone signal are expected to be observed as the two peaks near $\Delta\eta = 1.3$. But, such signals could not be observed in the real data within the statistical fluctuations. However, in this study, the total number of jets was only 0.089 M in the real data, compared to 1.6 M in the toy simulation. And also, the actual Mach cone signal of the data might be smaller than that of the simulation, or washed out during the QGP medium evolution. Therefore, more statistics are required for more concrete study with the hadron-hadron correlations. To provide a statistical limit to enable the hadron-hadron correlations in the data, a simple estimation was performed based on the toy simulation. For the estimation, the number of Mach-cone particles per jet is reduced from 10 to 2, to make similar result as the one in the data at the similar statistics, the number of jets $\sim$ 0.08 M. Under the condition, the hadron-hadron correlations were checked in different statistics in the simulation. Figure 6.13 shows the hadron-hadron correlations in the simulation,

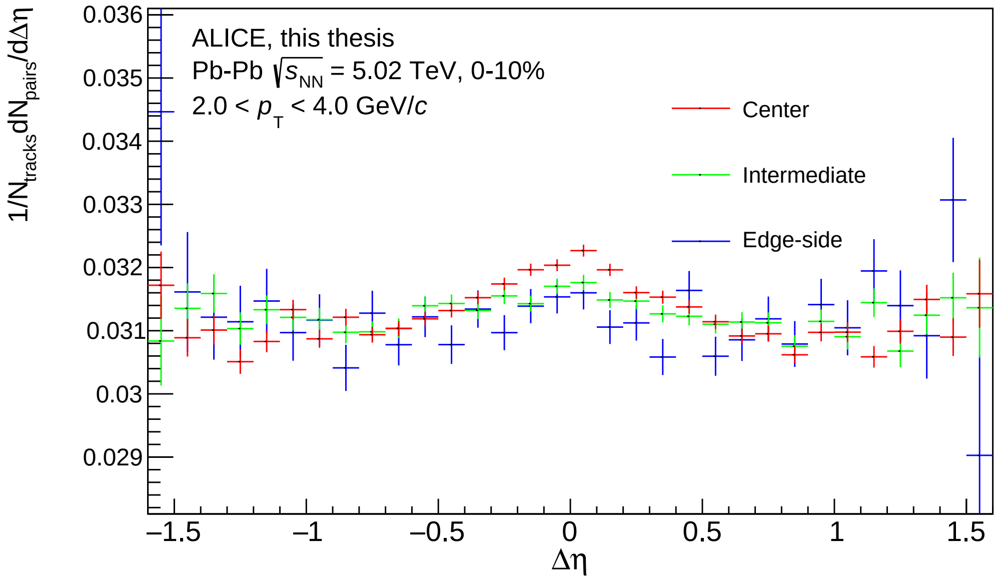

Figure 6.12: Data result: the differential hadron-hadron correlations according to different $\Delta\varphi$ projection ranges.

tuned the number of Mach-cone particles as 2, with jet statistics $= 0.64$ M. It shows a noticeable two peaks around $\Delta\eta = 1.3$. This jet statistics (0.64 M) is 8 times higher than the statistics in the current data.

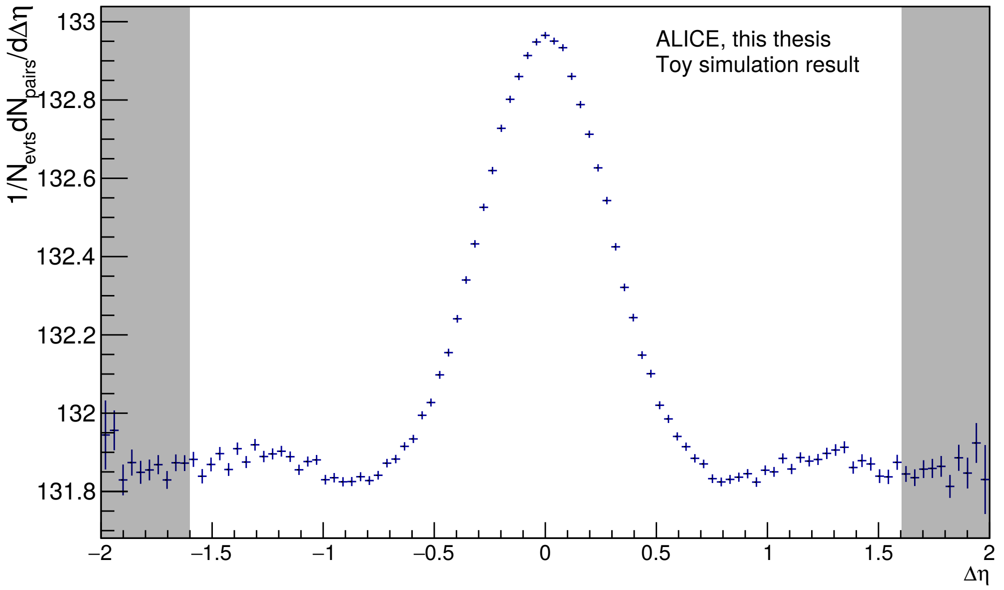

Figure 6.13: Toy simulation result: in the case for Mach particles = 2 per jet. Both gray regions were ignored to match the same η range with the result from the real data.

7 Summary and Outlook

When jets traverse the QGP, they lose all or part of their energy. It was suggested theoretically that Mach shock waves can be induced by jets as one of the possible interaction between jets and the QGP. Since Mach shock waves have a certain angle difference with respect to jet axis, an angular correlation can be helpful to search for evidence of Mach shock waves in the QGP.

This work describes jet-hadron and jet-proton angular correlations with data measured in Pb–Pb collisions at 5.02 TeV with the ALICE detector. The two different correlations were investigated because the proton abundance is different in the QGP medium and for jet fragmentation. By comparing the two correlations, particle production induced by the QGP medium rather than by the fragmentation can be studied. The widths of the correlation functions, obtained by a Gaussian fit method, do not show a difference between the jet-hadron correlations and the jet-proton correlations within uncertainties. A scaling was done to match the yield of the near-side peak between the results for hadrons and for protons. That way, the shapes of both jet-hadron and jet-proton correlations are compared. Minor shape differences were observed in the away-side peak in the $\Delta\varphi$ distribution around 2.4 and 3.6 rad, however, these differences were not sufficient to draw a conclusion due to statistical fluctuations in the jet-proton correlations.

Another analysis approach, hadron-hadron correlations of the away-side tracks, was investigated to search, in particular, for a Mach-cone signal around the away-side jets. While in jet-hadron correlations the away-side jet is smeared along the $\Delta\eta$ axis, the hadron-hadron correlations with the away-side tracks allow us to localize the away-side jet peak. $\Delta\eta$ (pseudorapidity) projections of the hadron-hadron correlations also enable us to neglect the flow effect. In addition, since the tracks used for the hadron-hadron correlations are chosen based on the geometrical information from the jet-hadron correlations, more relevant tracks to the away-side jets are involved in the hadron-hadron correlations. This is helpful to reduce tracks from background and to focus on the results related to the away-side jets. This analysis method was first examined with a toy Monte Carlo simulation. The input parameters for the simulation were tuned based on the jet-hadron correlations measured in the data. The implemented Mach-cone signals were observed in this approach. The Mach-cone signals show wider and more evident peaks in the hadron-hadron correlations, compared to the jet-hadron correlation, in the toy simulation. Based on the toy simulation, the same analysis approach was applied to the data. No

Mach-cone signal was observed in the data within statistical fluctuations. This result in the data can imply that the actual Mach-cone signal might be much smaller than the value in the simulation or washed out due to the QGP medium evolution. Therefore, for a precise study with the hadron-hadron correlation method, more statistics is needed. The current statistics of the data is 20 times less than that of the toy simulation. According to the rough assumption in the simulation, at least 8 times more statistics are required in the data for precise measurements.

For future measurements, higher statistics is one important factor. During the Long Shutdown (LS2, 2019-2021) after Run 2 (2015-2018), ALICE upgraded its central detectors, particularly the ITS with 7 silicon pixel layers and an upgrade of the TPC with Gas Electron Multipliers (GEMs) for continuous readout. Based on these upgrades, ALICE is currently preparing for a new data-taking period, LHC Run 3, with much-improved detector resolution and higher statistics. Therefore, investigating the jet-hadron and jet-proton correlations with increased statistics will be interesting and allow more quantitative and differential comparisons between both correlation results.

Another aspect that should be considered for future measurements is the initial location of jets in the QGP medium. According to [108], the Mach-cone signals are largely affected by the initial location of jets, as explained in Ch. 2. The paper insists that the signals cannot be propagated properly when the jet location is close to the center, since the signal is washed out due to the effect of the medium expansion. Since this aspect is not considered in this work, it will be interesting to study it in future measurements. The initial location of jets is not directly accessible in the experiments, but a correlation analysis depending on the angle to the event plane will provide relevant information about the relative location of jets in the QGP medium. Besides, although the associated p_{T} range ($2 < p_{\mathrm{T}} < 4$ GeV/c) was used in this work because of incomplete acceptance correction in a low p_{T} region, p_{T} differential analysis will be interesting. The p_{T} differential analysis is more challenging and statistics-hungry, since the dominant particle production mechanism changes for different p_{T} regions and the detector performance is also affected by the p_{T} of the tracks. Nevertheless, since the preferred p_{T} for the Mach-cone signals is unclear theoretically and experimentally, the p_{T} differential analysis will expand the measurement scope and also improve the understanding of background particle production included in the jet-hadron correlation analysis.

A Bibliography

[1] E. Rutherford, *LXXIX. the scattering of α and β particles by matter and the structure of the atom*, *The London, Edinburgh, and Dublin Philosophical Magazine and Journal of Science* **21** (1911) 669.

[2] E. Rutherford, *LIV. collision of α particles with light atoms. IV. an anomalous effect in nitrogen*, *The London, Edinburgh, and Dublin Philosophical Magazine and Journal of Science* **37** (1919) 581.

[3] J. Chadwick, *Possible existence of a neutron*, *Nature* **129** (1932) 312.

[4] H. Yukawa, *On the interaction of elementary particles. I.*, *Proc. Phys. Math. Soc. Jpn.* **17** (1935) 48.

[5] C. M. G. Lattes, G. P. S. Occhialini and C. F. Powell, *Observations on the tracks of slow mesons in photographic emulsions*, *Nature* **160** (1947) 453.

[6] M. Gell-Mann, *THE EIGHTFOLD WAY: A THEORY OF STRONG INTERACTION SYMMETRY*, Tech. Rep. TID-12608; CTSL-20, California Inst. of Tech., Pasadena. Synchrotron Lab., California Inst. of Tech., Pasadena. Synchrotron Lab. (Mar., 1961).

[7] M. Gell-Mann, *A schematic model of baryons and mesons*, *Physics Letters* **8** (1964) 214.

[8] G. Zweig, *An SU(3) model for strong interaction symmetry and its breaking. Version 2*, in *DEVELOPMENTS IN THE QUARK THEORY OF HADRONS. VOL. 1. 1964 - 1978*, D. B. Lichtenberg and S. P. Rosen, eds., pp. 22–101 (1964).

[9] M. Breidenbach et al., *Observed behavior of highly inelastic Electron-Proton scattering*, *Phys. Rev. Lett.* **23** (1969) 935.

[10] E. D. Bloom et al., *High-Energy inelastic $e-p$ scattering at 6° and 10°*, *Phys. Rev. Lett.* **23** (1969) 930.

[11] G. Miller et al., *Inelastic Electron-Proton scattering at large momentum transfers and the inelastic structure functions of the proton*, *Phys. Rev. D* **5** (1972) 528.

[12] J.-E. Augustin et al., *Discovery of a narrow resonance in* e^+e^- *annihilation*, *Phys. Rev. Lett.* **33** (1974) 1406.

[13] J. J. Aubert et al., *Experimental observation of a heavy particle* J, *Phys. Rev. Lett.* **33** (1974) 1404.

[14] S. W. Herb et al., *Observation of a dimuon resonance at 9.5 GeV in 400-GeV Proton-Nucleus collisions*, *Phys. Rev. Lett.* **39** (1977) 252.

[15] F. Abe et al., *Observation of top quark production in* p-$\bar{p}$ *collisions with the collider detector at fermilab*, *Phys. Rev. Lett.* **74** (1995) 2626.

[16] S. Abachi et al., *Observation of the top quark*, *Phys. Rev. Lett.* **74** (1995) 2632.

[17] Wikipedia contributors, "Standard model." `https://en.wikipedia.org/w/index.php?title=Standard_Model&oldid=1052862017`, Oct., 2021. Accessed: 11-Nov-2021.

[18] P. Langacker, *The Standard Model and Beyond*, Series in High Energy Physics, Cosmology and Gravitation,, Taylor & Francis (2017).

[19] S. L. Glashow, *Partial-symmetries of weak interactions*, *Phys. Rev. C Nucl. Phys.* **22** (1961) 579.

[20] S. Weinberg, *A model of leptons*, *Phys. Rev. Lett.* **19** (1967) 1264.

[21] A. Salam, *Proceedings of the 8th nobel symposium*, *Almquist & Wiskell, Stockholm* (1968) .

[22] G. 't Hooft and M. Veltman, *Regularization and renormalization of gauge fields*, *Nucl. Phys. B* **44** (1972) 189.

[23] P. W. Higgs, *Broken symmetries, massless particles and gauge fields*, *Physics Letters* **12** (1964) 132.

[24] G. S. Guralnik, C. R. Hagen and T. W. B. Kibble, *Global conservation laws and massless particles*, *Phys. Rev. Lett.* **13** (1964) 585.

[25] F. Englert and R. Brout, *Broken symmetry and the mass of gauge vector mesons*, *Phys. Rev. Lett.* **13** (1964) 321.

[26] E. W. Kolb and M. S. Turner, *Grand unified theories and the origin of the baryon asymmetry*, *Annu. Rev. Nucl. Part. Sci.* **33** (1983) 645.

[27] W. de Boer, *Grand unified theories and supersymmetry in particle physics and cosmology*, *Prog. Part. Nucl. Phys.* **33** (1994) 201.

[28] J. Ellis, *Outstanding questions: physics beyond the standard model*, *Philos. Trans. A Math. Phys. Eng. Sci.* **370** (2012) 818.

[29] H. L. Anderson, E. Fermi, E. A. Long and D. E. Nagle, *Total cross sections of positive pions in hydrogen*, *Phys. Rev.* **85** (1952) 936.

[30] T. M. Hahn et al., *Neutrons and Gamma-Rays from the proton bombardment of beryllium*, *Phys. Rev.* **85** (1952) 934.

[31] J. Ashkin, J. P. Blaser, F. Feiner and M. O. Stern, *Pion-Proton scattering at 150 and 170 MeV*, *Phys. Rev.* **101** (1956) 1149.

[32] V. E. Barnes et al., *Observation of a hyperon with strangeness minus three*, *Phys. Rev. Lett.* **12** (1964) 204.

[33] H. Fritzsch and M. Gell-Mann, *Current algebra: quarks and what else*, Tech. Rep. CONF-720923–P2, Max–Planck–Institute for Physics and Astrophysics. Munich, Germany, Lauritsen Laboratory of High Energy Physics, California, Institut of Technology, Pasadena, California (1972).

[34] H. Fritzsch, M. Gell-Mann and H. Leutwyler, *Advantages of the color octet gluon picture*, *Phys. Lett. B* **47** (1973) 365.

[35] M. Thomson, *Modern Particle Physics*, Cambridge University Press (Oct, 2013), 10.1017/CBO9781139525367.

[36] J. C. Collins and D. E. Soper, *The theorems of perturbative QCD*, *Annu. Rev. Nucl. Part. Sci.* **37** (1987) 383.

[37] G. Sterman et al., *Handbook of perturbative QCD*, *Rev. Mod. Phys.* **67** (1995) 157.

[38] **Particle Data Group** Collaboration, *Review of Particle Physics*, *PTEP* **2020** (2020) 083C01.

[39] J. C. Collins and M. J. Perry, *Superdense matter: Neutrons or asymptotically free quarks?*, *Phys. Rev. Lett.* **34** (1975) 1353.

[40] N. Cabibbo and G. Parisi, *Exponential hadronic spectrum and quark liberation*, *Phys. Lett. B* **59** (1975) 67.

[41] H.-T. Ding, F. Karsch and S. Mukherjee, *Thermodynamics of strong-interaction matter from Lattice QCD*, *Int. J. Mod. Phys. E* **24** (2015) 1530007.

[42] Y. Aoki et al., *The QCD transition temperature: results with physical masses in the continuum limit II*, *J. High Energy Phys.* **2009** (2009) 088.

[43] HotQCD Collaboration et al., *Chiral and deconfinement aspects of the QCD transition*, *Phys. Rev. D* **85** (2012) 054503.

[44] C. Ratti, *Lattice QCD and heavy ion collisions: a review of recent progress*, *Rep. Prog. Phys.* **81** (2018) 084301.

[45] K. G. Wilson, *Confinement of quarks*, *Phys. Rev. D* **10** (1974) 2445.

[46] K. G. Wilson, *The Origins of lattice gauge theory*, *Nucl. Phys. B Proc. Suppl.* **140** (2005) 3.

[47] "MADAI collaboration - heavy-ion collisions." `https://madai.phy.duke.edu/indexaae2.html?page_id=503`. Accessed: 2021-11-12.

[48] E. V. Shuryak, *Quark-gluon plasma and hadronic production of leptons, photons and psions*, *Phys. Lett. B* **78** (1978) 150.

[49] J. D. Bjorken, *Highly relativistic nucleus-nucleus collisions: The central rapidity region*, *Phys. Rev. D* **27** (1983) 140.

[50] R. Stock, *Relativistic Nucleus-Nucleus Collisions and the QCD Matter Phase Diagram*, *Theory and Experiments, Landolt-Börnstein - Group I Elementary Particles, Nuclei and Atoms* **21A** (2008) 225.

[51] P. Braun-Munzinger, K. Redlich and J. Stachel, *Particle production in heavy ion collisions*, in *Quark–Gluon Plasma 3*, pp. 491–599, World Scientific (2004).

[52] P. Braun-Munzinger, V. Koch, T. Schäfer and J. Stachel, *Properties of hot and dense matter from relativistic heavy ion collisions*, *Phys. Rep.* **621** (2016) 76.

[53] U. W. Heinz and M. R. M. Jacob, *Evidence for a New State of Matter: An Assessment of the Results from the CERN Lead Beam Programme*, Tech. Rep. nucl-th/0002042, CERN (2000).

[54] **STAR** Collaboration, *Experimental and theoretical challenges in the search for the quark gluon plasma: The STAR Collaboration's critical assessment of the evidence from RHIC collisions*, Nucl. Phys. A **757** (2005) 102.

[55] **PHOBOS** Collaboration, *The PHOBOS perspective on discoveries at RHIC*, Nucl. Phys. A **757** (2005) 28.

[56] **PHENIX** Collaboration, *Formation of dense partonic matter in relativistic nucleus-nucleus collisions at RHIC: Experimental evaluation by the PHENIX collaboration*, Nucl. Phys. A **757** (2005) 184.

[57] **BRAHMS** Collaboration, *Quark gluon plasma and color glass condensate at RHIC? The Perspective from the BRAHMS experiment*, Nucl. Phys. A **757** (2005) 1.

[58] J. D. Bjorken, "Energy loss of energetic partons in quark-gluon plasma: Possible extinction of high pt jets in hadron-hadron collisions." FERMILAB-PUB-82-059-THY, Aug., 1982.

[59] G.-Y. Qin et al., *Radiative and collisional jet energy loss in the quark-gluon plasma at the BNL relativistic heavy ion collider*, Phys. Rev. Lett. **100** (2008) 072301.

[60] **PHENIX** Collaboration, *Common suppression pattern of η and π^0 mesons at high transverse momentum in Au+Au collisions at $\sqrt{s_{\rm NN}} = 200$ GeV*, Phys. Rev. Lett. **96** (2006) 202301.

[61] J.-Y. Ollitrault, *Relativistic hydrodynamics for heavy-ion collisions*, Eur. J. Phys. **29** (2008) 275.

[62] A. Jaiswal and V. Roy, *Relativistic hydrodynamics in heavy-ion collisions: general aspects and recent developments*, Adv. High Energy Phys. **2016** (2016) 9623034.

[63] N. Herrmann, J. P. Wessels and T. Wienold, *Collective flow in heavy-ion collisions*, Annu. Rev. Nucl. Part. Sci. **49** (1999) 581.

[64] E. Schnedermann, J. Sollfrank and U. Heinz, *Thermal phenomenology of hadrons from 200A GeV S+S collisions*, Phys. Rev. C Nucl. Phys. **48** (1993) 2462.

[65] **ALICE** Collaboration, *Centrality dependence of π, K, p production in Pb-Pb collisions at $\sqrt{s_{NN}} = 2.76$ TeV*, Phys. Rev. C **88** (2013) 044910.

[66] N. Schmal, *Effect of feeddown contributions on blast-wave descriptions of elliptic flow and particle spectra data in heavy ion collisions*, Master's thesis, Heidelberg University, 2020.

[67] S. Voloshin and Y. Zhang, *Flow study in relativistic nuclear collisions by fourier expansion of azimuthal particle distributions*, *Zeitschrift für Physik C Particles and Fields* **70** (1996) 665.

[68] S. A. Voloshin, A. M. Poskanzer and R. Snellings, *Collective phenomena in non-central nuclear collisions*, *Theory and Experiments, Landolt-Börnstein - Group I Elementary Particles, Nuclei and Atoms* **23** (2010) 293.

[69] H. Satz, *Extreme States of Matter in Strong Interaction Physics: An Introduction*, Springer Science & Business Media (Mar., 2012).

[70] B. R. Martin, *Nuclear and particle physics*, John Wiley, Hoboken, NJ (2006).

[71] **H1, ZEUS** Collaboration, *Combination of measurements of inclusive deep inelastic $e^{\pm}p$ scattering cross sections and QCD analysis of HERA data*, *Eur. Phys. J. C* **75** (2015) 580.

[72] C. Diaconu, T. Haas, M. Medinnis, K. Rith and A. Wagner, *Physics accomplishments of HERA*, *Annu. Rev. Nucl. Part. Sci.* **60** (2010) 101.

[73] J. C. Collins, D. E. Soper and G. Sterman, *Factorization for short distance hadron-hadron scattering*, *Nucl. Phys. B* **261** (1985) 104.

[74] E. L. Berger, J. C. Collins, D. E. Soper and G. Sterman, *Diffractive hard scattering*, *Nucl. Phys. B* **286** (1987) 704.

[75] W. Hollik, *Quantum field theory and the standard model*, *Phys. Today* **67** (2014) 57.

[76] S. Catani and M. H. Seymour, *A general algorithm for calculating jet cross sections in NLO QCD*, *Nucl. Phys. B* **485** (1997) 291.

[77] S. Catani and M. H. Seymour, *Erratum to "a general algorithm for calculating jet cross sections in NLO QCD" [nucl. phys. B 485 (1997) 291–419]*, *Nucl. Phys. B* **510** (1998) 503.

[78] T. Kaufmann, A. Mukherjee and W. Vogelsang, *Hadron fragmentation inside jets in hadronic collisions*, *Phys. Rev. D* **92** (2015) 054015.

[79] D. d'Enterria and B. Betz, *High-pT hadron suppression and jet quenching*, in *The Physics of the Quark-Gluon Plasma*, in lecture notes in phys. 785, pp. 285–339, Springer Verlag (2009).

[80] J. J. Sakurai, *Advanced Quantum Mechanics*, Addison-Wesley Publishing Company (1967).

[81] B. G. Zakharov, *Parton energy loss in an expanding quark-gluon plasma: Radiative vs. collisional*, *JETP Lett.* **86** (2007) 444.

[82] R. Baier, Y. L. Dokshitzer, A. H. Mueller, S. Peigné and D. Schiff, *Radiative energy loss of high energy quarks and gluons in a finite-volume quark-gluon plasma*, *Nucl. Phys. B* **483** (1997) 291.

[83] R. Baier, D. Schiff and B. G. Zakharov, *Energy loss in perturbative QCD*, *Annu. Rev. Nucl. Part. Sci.* **50** (2000) 37.

[84] **CMS** Collaboration, *Correlations between jets and charged particles in PbPb and pp collisions at $\sqrt{s_{\mathrm{NN}}} = 2.76$ TeV*, *J. High Energy Phys.* **2016** (2016) 156.

[85] **ALICE** Collaboration, *First measurement of jet mass in Pb–Pb and p–Pb collisions at the LHC*, *Phys. Lett. B* **776** (2018) 249.

[86] **CMS** Collaboration, *Measurement of the groomed jet mass in PbPb and pp collisions at $\sqrt{s_{\mathrm{NN}}} = 5.02$ TeV*, *J. High Energy Phys.* **2018** (2018) 161.

[87] **STAR** Collaboration, *Evidence from d + Au measurements for final state suppression of high p(T) hadrons in Au+Au collisions at RHIC*, *Phys. Rev. Lett.* **91** (2003) 072304.

[88] **STAR** Collaboration, *Jet-hadron correlations in $\sqrt{s_{NN}} = 200 GeV$ p+p and central Au+Au collisions*, *Phys. Rev. Lett.* **112** (2014) 122301.

[89] **STAR** Collaboration, *Disappearance of Back-To-Back High-p_T hadron correlations in central AuAu collisions at $\sqrt{s_{NN}} = 200 GeV$*, *Phys. Rev. Lett.* **90** (2003) 082302.

[90] K. J. Eskola, H. Honkanen, C. A. Salgado and U. A. Wiedemann, *The fragility of high-pt hadron spectra as a hard probe*, *Nucl. Phys. A* **747** (2005) 511.

[91] **PHENIX** Collaboration, *Dihadron azimuthal correlations in Au+Au collisions at $\sqrt{s_{NN}} = 200$ GeV*, *Phys. Rev. C* **78** (2008) 014901.

[92] **STAR** Collaboration, *Azimuthal di-hadron correlations in d+Au and Au+Au collisions at* $\sqrt{s_{NN}} = 200$ *GeV from STAR*, *Phys. Rev. C* **82** (2010) 024912.

[93] J. A. Slavin, R. E. Holzer, J. R. Spreiter and S. S. Stahara, *Planetary mach cones: Theory and observation*, *J. Geophys. Res.* **89** (1984) 2708.

[94] H. Hornung, *Regular and mach reflection of shock waves*, *Annu. Rev. Fluid Mech.* **18** (1986) 33.

[95] H. Reichenbach, *In the footsteps of ernst mach — a historical review of shock wave research at the Ernst-Mach-Institut*, *Shock Waves* **2** (1992) 65.

[96] Wikipedia contributors, "Mach wave." `https://en.wikipedia.org/w/index.php?title=Mach_wave&oldid=1029511552`, June, 2021. Accessed: 11-Nov-2021.

[97] C. Neipp, A. Hernández, J. J. Rodes, A. Márquez and A. Beléndez, *An analysis of the classical doppler effect*, *Eur. J. Phys.* **24** (2003) 497.

[98] K. Plotkin, *Review of sonic boom theory*, in *12th Aeroacoustic Conference* (1989), DOI [`https://arc.aiaa.org/doi/pdf/10.2514/6.1989-1105`].

[99] Wikipedia contributors, "Cherenkov radiation." `https://en.wikipedia.org/w/index.php?title=Cherenkov_radiation&oldid=1051268856`, Oct., 2021. Accessed: 11-Nov-2021.

[100] W. R. Leo, *Techniques for Nuclear and Particle Physics Experiments: A How-to Approach*, Springer, Berlin, Heidelberg (1994).

[101] **ALICE** Collaboration, *The ALICE experiment at the CERN LHC*, *J. Instrum.* **3** (2008) S08002.

[102] D. Samsonov, J. Goree, H. M. Thomas and G. E. Morfill, *Mach cone shocks in a two-dimensional yukawa solid using a complex plasma*, *Phys. Rev. E Stat. Phys. Plasmas Fluids Relat. Interdiscip. Topics* **61** (2000) 5557.

[103] P. Bandyopadhyay, K. Jiang, R. Dey and G. E. Morfill, *Effect of polarization force on the mach cones in a complex plasma*, *Phys. Plasmas* **19** (2012) 123707.

[104] L. Couëdel et al., *Three-dimensional structure of mach cones in monolayer complex plasma crystals*, *Phys. Rev. Lett.* **109** (2012) 175001.

[105] J. Liang et al., *Single-shot real-time video recording of a photonic mach cone induced by a scattered light pulse*, *Sci Adv* **3** (2017) e1601814.

[106] Y. Ito et al., *Interferometric and fluorescence analysis of shock wave effects on cell membrane*, *Communications Physics* **3** (2020) 1.

[107] B. Baeuchle, L. Csernai and H. Stoecker, *MACE – mach cones in heavy ion collisions*, `0710.1476`.

[108] E. Shuryak and P. Staig, *Sound edge of the quenching jets*, *Phys. Rev. C Nucl. Phys.* **88** (2013) 054903.

[109] J. Casalderrey-Solana, E. V. Shuryak and D. Teaney, *Conical flow induced by quenched QCD jets*, *J. Phys. Conf. Ser.* **27** (2005) 003.

[110] H. Stöcker, *Collective flow signals the quark–gluon plasma*, *Nucl. Phys. A* **750** (2005) 121.

[111] L. M. Satarov, H. Stöcker and I. N. Mishustin, *Mach shocks induced by partonic jets in expanding quark–gluon plasma*, *Phys. Lett. B* **627** (2005) 64.

[112] J. Ruppert and B. Müller, *Waking the colored plasma*, *Phys. Lett. B* **618** (2005) 123.

[113] I. M. Dremin, *Ring-like events: Cherenkov gluons or mach waves?*, *Nucl. Phys. A* **767** (2006) 233.

[114] A. Majumder and X.-N. Wang, *Landau-Pomeranchuck-Migdal interference and cherenkov-like gluon bremsstrahlung in dense matter*, *Phys. Rev. C Nucl. Phys.* **73** (2006) 051901.

[115] **ALICE** Collaboration, *Higher harmonic anisotropic flow measurements of charged particles in Pb-Pb collisions at* $\sqrt{s_{\rm NN}}$ *=2.76 TeV*, *Phys. Rev. Lett.* **107** (2011) 032301.

[116] P. Staig and E. Shuryak, *Fate of the initial state perturbations in heavy ion collisions. II. glauber fluctuations and sounds*, *Phys. Rev. C Nucl. Phys.* **84** (2011) 034908.

[117] P. Staig and E. Shuryak, *Fate of the initial state perturbations in heavy ion collisions. III. the second act of hydrodynamics*, *Phys. Rev. C Nucl. Phys.* **84** (2011) 044912.

[118] E. Shuryak, *Shocks and sounds in Quark–Gluon plasma*, *Nucl. Phys. A* **904-905** (2013) 349c.

[119] E. Shuryak and P. Staig, *Sounds of the QCD phase transition*, *Phys. Rev. C Nucl. Phys.* **88** (2013) 064905.

[120] **STAR** Collaboration, *Di-hadron correlations with identified leading hadrons in 200 GeV Au+Au and d+Au collisions at STAR*, *Phys. Lett. B* **751** (2015) 233.

[121] J. Klein, *Jet Physics with A Large Ion Collider Experiment at the Large Hadron Collider*, Ph.D. thesis, Heidelberg University, Nov., 2014.

[122] **ALICE** Collaboration, *Harmonic decomposition of two particle angular correlations in Pb–Pb collisions at* $\sqrt{s_{\rm NN}}$*=2.76 TeV*, *Phys. Lett. B* **708** (2012) 249.

[123] F. Krizek and for the ALICE Collaboration, *Correlations and flavors in jets in ALICE*, *J. Phys. Conf. Ser.* **668** (2016) 012018.

[124] **ATLAS** Collaboration, *The ATLAS experiment at the CERN large hadron collider*, *J. Instrum.* **3** (2008) S08003.

[125] **CMS** Collaboration, *The CMS experiment at the CERN LHC*, *J. Instrum.* **3** (2008) S08004.

[126] **LHCb** Collaboration, *The LHCb detector at the LHC*, *J. Instrum.* **3** (2008) S08005.

[127] L. Evans and P. Bryant, *LHC machine*, *J. Instrum.* **3** (2008) S08001.

[128] **ALICE** Collaboration, *Performance of the ALICE experiment at the CERN LHC*, *Int. J. Mod. Phys. A* **29** (2014) 1430044.

[129] P. C. L. Betev, "Definition of the ALICE coordinate system and basic rules for sub-detector components numbering." internal report (ALICE-INT-2003-038).

[130] A. Tauro, *A schematics of the ALICE detector*, May, 2017. https://cds.cern.ch/record/2263642, ALICE-PHO-SKE-2017-001.

[131] **ALICE** Collaboration, *ALICE forward detectors: FMD, TO and VO: Technical Design Report*, 2004. https://cds.cern.ch/record/781854, CERN-LHCC-2004-025.

[132] **ALICE** Collaboration, *Performance of the ALICE VZERO system*, *J. Instrum.* **8** (2013) P10016.

[133] **ALICE** Collaboration, *Alignment of the ALICE inner tracking system with cosmic-ray tracks*, *J. Instrum.* **5** (2010) P03003.

[134] J. Alme et al., *The ALICE TPC, a large 3-dimensional tracking device with fast readout for ultra-high multiplicity events*, *Nucl. Instrum. Methods Phys. Res. A* **622** (2010) 316.

[135] M. Arslandok, *Event-by-Event Identified Particle Ratio Fluctuations in Pb–Pb Collisions with ALICE*, Ph.D. thesis, Frankfurt University, 2017.

[136] **ALICE** Collaboration, P. Cortese, *ALICE Time-Of Flight system (TOF): addendum to the Technical Design Report*, Technical design report. ALICE, CERN, Geneva (2002).

[137] R. Brun and F. Rademakers, *ROOT — an object oriented data analysis framework*, *Nucl. Instrum. Methods Phys. Res. A* **389** (1997) 81.

[138] I. Antcheva et al., *ROOT — a C++ framework for petabyte data storage, statistical analysis and visualization*, *Comput. Phys. Commun.* **180** (2009) 2499.

[139] “ALICE software.” `https://github.com/alisw/`. Accessed: 2021-12-2.

[140] M. Cacciari, G. P. Salam and G. Soyez, *FastJet user manual*, *The European Physical Journal C* **72** (2012) 1896.

[141] K. Bos et al., *LHC computing Grid: Technical Design Report. Version 1.06* , 2005. https://cds.cern.ch/record/840543, CERN-LHCC-2005-024.

[142] M. L. Miller, K. Reygers, S. J. Sanders and P. Steinberg, *Glauber modeling in High-Energy nuclear collisions*, *Annu. Rev. Nucl. Part. Sci.* **57** (2007) 205.

[143] M. O. Schmidt, *Space Point Calibration of the ALICE TPC with Track Residuals*, Ph.D. thesis, Heidelberg University, July, 2020.

[144] R. E. Kalman, *A new approach to linear filtering and prediction problems*, *Transactions of the ASME–Journal of Basic Engineering* **82** (1960) 35.

[145] M. Ivanov, *Identified charged hadron production measured with ALICE at the LHC*, *Nucl. Phys. A* **904-905** (2013) 162c.

[146] B. A. Hess, *Particle Identification in Jets and High-Multiplicity pp Events with the ALICE TPC*, Ph.D. thesis, Tubingen University, Oct., 2015.

[147] M. Cacciari, G. P. Salam and G. Soyez, *The anti-kt jet clustering algorithm*, *J. High Energy Phys.* **2008** (2008) 063.

[148] M. Gyulassy and X.-N. Wang, *HIJING 1.0: A monte carlo program for parton and particle production in high energy hadronic and nuclear collisions*, *Comput. Phys. Commun.* **83** (1994) 307.

[149] B. Andersson, G. Gustafson and B. Söderberg, *A general model for jet fragmentation*, *Zeitschrift für Physik C Particles and Fields* **20** (1983) 317.

[150] R. Brun et al., *GEANT: Detector description and simulation tool*, Tech. Rep. W5013 ; W-5013 ; CERN-W5013 ; CERN-W-5013, CERN (1993).

[151] "GSL - GNU scientific library - GNU project - free software foundation." `https://www.gnu.org/software/gsl/`. Accessed: 2021-12-14.

[152] D. Teaney, *Effect of shear viscosity on spectra, elliptic flow, and Hanbury Brown–Twiss radii*, *Phys. Rev. C Nucl. Phys.* **68** (2003) 034913.

[153] **ALICE** Collaboration, *Production of charged pions, kaons, and (anti-)protons in Pb-Pb and inelastic pp collisions at $\sqrt{s_{\mathrm{NN}}}$=5.02 TeV*, *Phys. Rev. C Nucl. Phys.* **101** (2020) 044907.

[154] Y. L. Dokshitzer and D. E. Kharzeev, *Heavy quark colorimetry of QCD matter*, *Phys. Lett. B* **519** (2001) 199 [`hep-ph/0106202`].

[155] R. Barlow, *Systematic errors: facts and fictions*, `hep-ex/0207026`.

[156] **ALICE** Collaboration, *Transverse momentum spectra and nuclear modification factors of charged particles in pp, p-pb and Pb-Pb collisions at the LHC*, *J. High Energy Phys.* **2018** (2018) 13.

[157] **ALICE** Collaboration, *Anisotropic flow of charged particles in Pb-Pb collisions at $\sqrt{s_{\mathrm{NN}}}$=5.02 TeV*, *Phys. Rev. Lett.* **116** (2016) 132302.

[158] **ALICE** Collaboration, *Azimuthal anisotropy of charged jet production in $\sqrt{s_{\mathrm{NN}}} = 2.76$ TeV Pb–Pb collisions*, *Phys. Lett. B* **753** (2016) 511.

Acknowledgements

First of all, I would like to express my deepest gratitude to my supervisors, Prof. Dr. Johanna Stachel and Dr. Alice Ohlson, for their continued support and assistance during my doctoral studies. During the supervision I've learned a lot of physics, especially from Frau Stachel, also the passionate attitude to life. I was so happy studying at this beautiful research group ALICE@PI. I would like to thank Alice for the kind and in-depth guidance and warm encouragements. I wouldn't be where I am today without the helps.

Big thanks to Dr. Alexander Schmah who always guided me with good questions and discussions, and enthusiastically reviewed my thesis. And I would like to thank Prof. Norbert Herrmann for being a referee for my final exam. And many thanks to Dr. Ole Schmidt, Dr. Mesut Arslandok, Dr. Martin Voelk, and Prof. Dr. Klaus Reygers, who helped me by answering my silly questions and reviewing my thesis.

Thanks to my colleagues, Minjung Kim, Meike Danish, PD. Dr. Yvonne Pachmayer, and Luisa Bergmann, who has supported and encouraged me during the hard times, and also, especially Minjung and Meike for the lots of physics discussion during the writing. I also would like to give many thanks to all other members of the ALICE@PI (past and present), full of such lovely people, because of you, I was never lonely in Germany.

I would like to thank my collaborators in ALICE, Dr. Jens Wiechula and Martin Schmidt, who helped me a lot for my service task, and also other ones worked together in PWG JE and CF. Many thanks to BongHwi Lim, who always advised me whenever encountering technical problems of the analysis software and listened to me in the hard times. And I would like to thank my beloved parents, brother, and Jeongbin for all the consistent supports and trust. I would like to thank all my friends in Korea as well for supports and encouragements.

Last but not least, I would like to mention the supports by Dr. Oliver Busch, which helped me a lot to begin the journey as a doctoral student. I would like to dedicate my thesis to Oliver, who would be so happy in a good place with the completion of my thesis.

Erklärung:

Ich versichere, dass ich diese Arbeit selbstständig verfasst habe und keine anderen als die angegebenen Quellen und Hilfsmittel benutzt habe.

Heidelberg, den (Datum) ....